SLAC-R-548
UC-410

Structural Studies of Alkali Metal Adsorption on Silicon Surfaces

Erik Jonathan Nelson

Stanford Linear Accelerator Center
Stanford University
Stanford, CA 94309

SLAC-Report-548
December 1999

Prepared for the Department of Energy
under contract number DE-AC03-76SF00515

Printed in the United States of America. Available from the National Technical Information Service, U.S. Department of Commerce, 5285 Port Royal Road, Springfield, VA 22161.

STRUCTURAL STUDIES
OF ALKALI METAL ADSORPTION
ON SILICON SURFACES

A DISSERTATION

SUBMITTED TO THE DEPARTMENT OF PHYSICS

AND THE COMMITTEE ON GRADUATE STUDIES

OF STANFORD UNIVERSITY

IN PARTIAL FULFILLMENT OF THE REQUIREMENTS

FOR THE DEGREE OF

DOCTOR OF PHILOSOPHY

Erik Jonathan Nelson

October 1999

To Mom, Dad, and Beth

ABSTRACT

Structural Studies of Alkali Metal Adsorption on Silicon Surfaces

The knowledge of the location of the atoms at a metal/semiconductor interface is a prerequisite to the understanding of its electronic structure. Unlike some metals, alkali metals (AM's) form abrupt, ordered monolayer interfaces with semiconductors, since they neither react nor cluster. This ordered adsorption, as well as the simple AM electronic structure of one valence *s*–electron, allows simplifications in theoretical models and in interpretations of experimental data of the AM/Silicon interface which are not available for metal/semiconductor interfaces in general. This thesis will document the use of a combination of synchrotron experimental techniques to determine the geometrical structure of a number of AM/Si interfaces. Knowledge of adsorption sites and substrate geometry from experiment will give a better starting point for theoretical calculations to explain the electronic structure and properties of these interfaces. In addition, studying the changes in surface reconstruction geometries of these interfaces with different AM coverages and under annealing will provide information on the adsorption process.

The substrate surface which was chosen to use in the AM/semiconductor interface studies is the Si(111)2x1 surface. The 2x1 surface reconstruction is formed by cleaving along the (111) plane of crystalline Si in vacuum. This surface has a well-characterized surface reconstruction, which is important for determining adsorption geometries. The 2x1 reconstruction is a pi-bonded chain, and the direction of the chain can be exploited in determining the adsorption geometry. The Si(111)2x1 surface is semiconducting with important surface states in the energy gap that can be altered by AM adsorption. In addition, while the Si(111)2x1 reconstruction is energetically stable for the clean surface, the total energy difference between this reconstruction and the ideal bulk-terminated Si(111)1x1 surface is small enough that room-temperature AM adsorption can revert the Si(111) surface structure to bulk-terminated. As with the Si(111) wafer surface, annealing the cleaved AM/Si(111) interface produces a 3x1 Si surface reconstruction for Na and K adsorption.

The AM adsorbates used for this thesis will be K, Na, and Cs. We have found a number of previously unobserved reconstructions for room-temperature adsorption of each of the three alkali metals on the Si(111)2x1 surface. The results observed for K and Cs adsorption have several similarities, and are different from those for Na. The

three AM adsorbates span a range of atomic sizes, electronic structures, electronegativities, and interaction strengths, and from their adsorption behavior the importance of these factors can be determined. The different sizes of adsorbate atoms affect the choice of adsorption site as well as the adsorbate-adsorbate spacing and therefore the periodicity and electronic structure of the interface.

In terms of the experimental approach, a two-step regimen of several synchrotron experimental techniques is applied to the above AM/Si systems. In the first step, we utilize core-level and valence-band photoelectron spectroscopy (PES) in conjunction with LEED and secondary electron cutoff (work function difference) measurements for a series of increasing AM coverages upon the cleaved Si(111) surface. This provides a detailed picture of the electronic structure changes of the interfaces with adsorbate coverage through a structural transition. The ability to select photon energy using synchrotron radiation enhances core-level and valence band PES, as a variety of peaks can be examined at tunable surface sensitivity.

The second step of our regimen is our structural study via back-reflection X-ray standing waves (XSW). XSW is a synchrotron technique which determines the distance of adatoms from a chosen diffracting plane. The distances are determined from fitting absorption spectra of the AM atoms taken as the incident X-ray photon energy is varied about the Bragg reflection energy. XSW is performed on both the 111 and $(11\bar{1})$ diffracting planes of Si, which are normal to and mostly lateral to the Si(111) surface, respectively. The resulting distances from the two planes can be triangulated to determine the adsorption site of the adatoms. Determination of substrate atom positions and of the effect of overlayers upon the surface reconstruction can be achieved by making the XSW measurements sensitive to electrons emitted by the surface Si atoms as compared to the bulk Si atoms. Surface-sensitive data for Si are taken by detecting Si 1s photoelectrons, which have a kinetic energy of ~135 eV at the Si Bragg energy of 1977 eV, and therefore short (5-10 Å) escape depths. XSW is used to determine the AM and surface Si atomic geometry of the Na/Si(111)1x1, Na/Si(111)3x1, K/Si(111)3x1, and Cs/Si(111)$\sqrt{3}$x$\sqrt{3}$–R30° interfaces.

ACKNOWLEDGEMENTS

There are many people to whom I am very grateful for the help they have given me in carrying out and completing my graduate work.

Piero Pianetta has been an excellent adviser, and the guidance, support, and knowledge he has given in numerous discussions were invaluable. His eagerness to assist with experiments and problems at the beam lines as well as his ability to find needed equipment and resources have made my experience in synchrotron experiments productive, educational, and enjoyable.

I would not have attained my current level of understanding or technical ability in the X-ray standing wave technique without the training and support of Tom Kendelewicz. Tom taught me the technique when I started my dissertation work, and our numerous technical discussions have helped me best interpret our standing wave data in conjunction with the results of other techniques, and have given me valuable information about the field of surface science. Tom also provided guidance in planning and performing experiments, and helped take some of the data presented in this dissertation.

I thank Joe Woicik for sharing with me the idea of extending X-ray standing waves to study valence electron emission, and for encouraging me to pursue a NIST/NRC Postdoctoral Research Associateship with him at Brookhaven National Laboratory. I look forward to collaborating with him in the next two years.

I am grateful to Ping Liu, who helped me take some of the data presented in this dissertation and provided guidance as the senior graduate student on the beam line. I always will remember the long days (and nights) of experiments on the beam lines at SSRL spent with Tom and Ping.

I also extend my gratitude to Professors Gordon Brown, Z. X. Shen, and Sandy Fetter, who participated in my oral defense along with Piero and Tom. Prof. Brown gave insight into geological applications for X-ray standing waves, and Prof. Shen has suggested possible applications of the new Valence-Band X-ray Standing Wave

technique to colossal magnetoresistive and superconducting materials. I also greatly appreciate the help and supportive environment provided by the Brown and Shen research groups.

My experimental work at SSRL would not have been completed with out the support of the staff at SSRL and Stanford, and in particular I thank Jeff Moore, Curtis Troxel, Al Armes, Gloria Barnes, and Marilyn Gordon for all their help. I also thank my fellow students Renée Mo, Steven Sun, Colin Doyle, Zahid Hasan, Paul White, Changyoung Kim for their assistance, support, and friendship.

Finally, I would like to thank my family and friends for always being supportive of me and my work, and for keeping me going during the difficult times.

TABLE OF CONTENTS

LIST OF TABLES

LIST OF ILLUSTRATIONS

CHAPTER ONE

INTRODUCTION

The knowledge of the location of the atoms at a metal/semiconductor interface is a prerequisite to the understanding of its electronic structure. Unlike some metals, alkali metals (AM's) form abrupt, ordered single atomic layer interfaces with semiconductors, since they neither react nor cluster[1]. This ordered adsorption, as well as the simple AM electronic structure of one valence *s*–electron, allows simplifications in theoretical models and in interpretations of experimental data of the AM/Silicon interface which are not available for metal/semiconductor interfaces in general. This dissertation will document the use of a combination of synchrotron experimental techniques to determine the geometrical structure of a number of AM/Si interfaces. Knowledge of adsorption sites and substrate geometry from experiment will give a better starting point for theoretical calculations to explain the electronic structure and properties of these interfaces. In addition, studying the changes in surface reconstruction geometries of these interfaces with different AM coverages and under annealing will provide information on the adsorption process.

The substrate surface which was chosen to use in the AM/semiconductor interface studies is the Si(111)2x1 surface. The 2x1 surface reconstruction is formed

by cleaving along the (111) plane of crystalline Si in vacuum. This surface has a well-characterized surface reconstruction, which is important for determining adsorption geometries. The Si(111)2x1 reconstruction is the π-bonded chain structure first proposed by Pandey[2], and the direction of the chain can be exploited in determining the adsorption geometry. The Si(111)2x1 surface is semiconducting with important surface states in the energy gap that can be altered by AM adsorption. In addition, while the Si(111)2x1 reconstruction is energetically stable for the clean surface, the total energy difference between this reconstruction and the ideal bulk-terminated Si(111)1x1 surface is 0.36 eV per surface Si atom[3], which is small enough that room-temperature AM adsorption can revert the Si(111) surface structure to the bulk-terminated case, where the surface atoms are located in the extended bulk positions. As with the Si(111)7x7 wafer surface, annealing the cleaved AM/Si(111) interface produces a 3x1 Si surface reconstruction upon Na and K adsorption.

The AM adsorbates used for this thesis will be K, Na, and Cs. We have found a number of previously unobserved reconstructions for room-temperature adsorption of each of the three alkali metals on the Si(111)2x1 surface. The results observed for K and Cs adsorption have several similarities, and are different from those for Na. The three AM adsorbates span a range of atomic sizes, electronic structures, electronegativities, and interaction strengths, and from their adsorption behavior the importance of these factors can be determined. The different sizes of adsorbate atoms affect the choice of adsorption site as well as the adsorbate-adsorbate spacing and therefore the periodicity and electronic structure of the interface.

The AM/semiconductor interfaces have the property of a work function (i.e. the minimum energy required for a photoelectron to escape the surface) which is reduced significantly from the work function of the clean semiconductor surface[1]. For Na, K, and Cs on Si(111), this work function decrease ranges from 2.7 to 3.6 eV at coverages near saturation coverage. As a function of AM coverage, the work function decreases sharply until it reaches a minimum close to a full atomic layer of AM and then saturates or increases slightly at saturation coverage (an example is given in Figure 4.14 of Chapter 4 for Cs/Si(111)). This behavior indicates two different coverage regimes for the AM/semiconductor interface. At low AM coverages, the linear decrease in work function with coverage corresponds to the formation of independent dipoles upon the surface when the AM donates its valence electron to the semiconductor surface dangling bonds. As the coverage increases, the lateral distance between dipoles on the surface shortens, and AM-AM interactions become more important. These interactions tend to reduce the amount of alkali charge donated to the semiconductor surface in favor

of forming a more metallic AM overlayer. This causes a depolarization of the surface dipoles, which results in a decrease of the slope of the work function change until a minimum is reached. The relative importance of AM-Si and AM-AM interactions will determine whether the underlying Si surface reconstruction will change upon AM adsorption, and will be addressed in our coverage-dependent studies of the AM/Si(111) surfaces through photoemission spectroscopy and work function difference measurements.

In terms of the experimental approach, a two-step regimen of four synchrotron experimental techniques is applied to the above AM/Si systems. In the first step, we utilize core-level and valence-band photoelectron spectroscopy (PES) in conjunction with LEED and secondary electron cutoff (work function difference) measurements for a series of increasing AM coverages upon the cleaved Si(111) surface. This provides a detailed picture of the electronic structure changes of the interfaces with adsorbate coverage through a structural transition. LEED provides information on the surface periodicity of the interface structure. The ability to select photon energy using synchrotron radiation enhances core-level and valence band PES, as a variety of peaks can be examined at tunable surface sensitivity. In addition, alkali core-level photoemission spectra and work function difference measurements provide a reliable determination of AM coverage.

The second step of our regimen is our structural study via back-reflection X-ray standing waves (XSW). XSW is a synchrotron technique which combines the elemental specificity of X-ray absorption yields with the spatial resolution of X-ray diffraction techniques[4-8]. The technique is named after the standing wavefield formed from the superposition of the incident X-rays and the X-rays reflected off of the bulk crystal lattice. The position of the X-ray standing wavefield intensity profile is shifted with respect to the diffracting planes as the photon energy is varied through the finite width of the Bragg reflectivity. XSW determines the distance of adatoms from a chosen diffracting plane. The distances are determined from fitting absorption spectra of the AM atoms taken as the incident X-ray photon energy is varied about the Bragg reflection energy. XSW is performed on both the (111) and $(11\bar{1})$ diffracting planes of Si, which are normal to and mostly lateral to the Si(111) surface, respectively. The resulting distances from the two planes can be triangulated to determine the adsorption site of the adatoms. Determination of substrate atom positions and of the effect of overlayers upon the surface reconstruction can be achieved by making the XSW measurements sensitive to electrons emitted by the surface Si atoms as compared to the bulk Si atoms. Surface-sensitive data for Si are taken by detecting Si 1s

photoelectrons, which have a kinetic energy of ~135 eV at the Si Bragg energy of 1977 eV, and therefore short (5-10 Å) escape depths. The surface-sensitive Si 1s XSW data are compared to simulated XSW data expected for proposed structural models of the Si(111) reconstruction to determine the most correct surface structure. Photoemission spectra provide information on the chemical environment of AM adatoms and Si surface atoms, which also can be as used to help determine the structural environment of these atoms. XSW is used to determine the AM and surface Si atomic geometry of the Na/Si(111)1x1, Na/Si(111)3x1, K/Si(111)3x1, and Cs/Si(111)$\sqrt{3}$x$\sqrt{3}$-R30° interfaces.

Outline of the Dissertation

The dissertation is divided into nine chapters, organized primarily by experimental technique and secondarily by the interface investigated.

Chapter 2 is a discussion of the experimental setup and techniques, including the details of the AM/Si(111) sample preparation, the vacuum chamber, the experimental techniques, and the two beam lines used in the experiments, namely Beam Lines 3-3 (JUMBO) and 8-1 at the Stanford Synchrotron Radiation Laboratory (SSRL).

Chapter 3 describes the X-ray Standing Wave technique in detail, including the theoretical basis of the basic standing wave equation and an introduction and interpretation of the two fitting parameters known as the coherent distance and coherent fraction.

Chapter 4 presents and evaluates the LEED, photoemission, and work function difference data collected as the alkali metal coverage is increased from 0% to 100% saturation coverage in stepwise room-temperature doses upon the cleaved Si(111) surface. Results are presented and compared for Na, K, and Cs adsorption. Each alkali produces previously unreported LEED patterns upon adsorbing to Si(111). Both K and Cs go through a complex progression of LEED patterns with little change in the corresponding photoemission spectra, while Na has a simpler LEED progression and substantial changes in the photoemission spectra. In addition, we investigate the photoemission spectra for the annealed Na/Si(111)3x1 and K/Si(111)3x1 interfaces.

Chapters 5 through 7 examine the adsorbate and substrate atomic structure of various AM/Si(111)1x1 interfaces upon the cleaved Si(111) surface using alkali core-level and Auger yield and surface-sensitive Si 1s yield X-ray standing waves as well as photoemission, LEED, and work function difference measurements. In each case,

LEED provides preliminary information on the overall surface periodicity, while alkali core-level photoemission and work function data determine the coverage. Next the Si 1s XSW data are compared to simulated XSW data corresponding to different Si(111) surface structural models to determine the substrate reconstruction, if any. The alkali adatom positions are determined both through the (111) coherent distance for the alkali absorption yield XSW data, which gives the adatom height above the Si surface, and through the combination of (111) and $(11\bar{1})$ reflection XSW data, which triangulates the lateral position of the adatom. Photoemission spectra also provide supporting structural information about the local bonding environment of the alkali and surface Si atoms.

Chapter 5 examines the adsorbate and substrate atomic structure of the saturation coverage Na/Si(111)1x1 interface. The underlying Si surface atoms are determined to be in positions corresponding to the bulk, and Na is found to adsorb in two high-symmetry sites upon the bulk-terminated surface.

Chapter 6 presents the atomic structure of the room-temperature dosed Cs/Si(111)$\sqrt{3}$x$\sqrt{3}$–R30^{o} interface at 1/3 monolayer (ML) Cs coverage. Our proposed structural model retains the underlying Si π-bonded chain of the clean Si(111)2x1 surface. Cs is adsorbed in two nearly equivalent sites on either side of this chain. The LEED pattern of this model is simulated in the kinematic approximation and is found to match the $\sqrt{3}$x$\sqrt{3}$–R30^{o} pattern over the observed energy range.

Chapter 7 examines the atomic structure of the annealed Na/Si(111)3x1 and K/Si(111)3x1 interfaces at 1/3 ML alkali coverage through the comparison of three proposed structural models. The model which best matches the alkali and silicon XSW data is a missing-top layer model with Si chains of 3x1 periodicity. Na and K are adsorbed in sites to the sides of these chains. In addition, the structure of the room-temperature dosed K/Si(111)3x1 interface is determined, at a coverage near 2/3 ML K. This Si substrate reconstruction is an extended version of the Pandey π-bonded chain model with 3x1 periodicity, and again K adsorbs to the sides of the chains to satisfy the dangling bonds.

Chapter 8 describes preliminary experiments to test the feasibility of extending the X-ray standing wave technique to monitor valence or bonding electron photoemission. The Valence Band X-Ray Standing Wave (VBXSW) technique is used successfully to measure the polarity of bonds in bulk GaAs. In addition, the valence emission of bulk Ge produces a different result than Ge core-level emission, and the connection between this result and the delocalization of the initial bonding state is discussed, as well as complications in the interpretation of the data due in part to the

high photoelectron and photon energies involved. It is our hope that this technique will develop into a new and effective method of spatially resolving valence and bonding electronic states.

Chapter 9 summarizes the results of the experiments and makes overall conclusions about the alkali adsorption process and AM/Si(111) electronic structure. In addition, ideas for future work with VBXSW are presented.

References

[1] See reviews in H. P. Bonzel, A. M. Bradshaw, and G. Ertl, eds., Physics and Chemistry of Alkali Metal Adsorption, Amsterdam: Elsevier, 1989.

[2] K. C. Pandey, Phys. Rev. Lett. 47 (1981) 1913.

[3] J. E. Northrup and M. L. Cohen, Phys. Rev. Lett. 49 (1982) 1349.

[4] B. W. Batterman and H. Cole, Rev. Mod. Phys. 36 (1964) 681.

[5] P. L. Cowan, J. A. Golovchenko, and M. F. Robbins, Phys. Rev. Lett. 44 (1980) 1680.

[6] J. A. Golovchenko, J. R. Patel, D. R. Kaplan, P. L. Cowan, and M. J. Bedzyk, Phys. Rev. Lett. 49 (1982) 560 .

[7] J. Zegenhagen, Surf. Sci. Rep. 18 (1993) 199.

[8] D. P. Woodruff, Prog. Surf. Sci. 57 (1998) 1.

CHAPTER TWO

EXPERIMENTAL SETUP AND SAMPLE PREPARATION

Sample preparation

All experiments were performed inside a UHV chamber, with ~$3x10^{-11}$ torr base pressure. Ultra-high vacuum (UHV) was required during the experiment as room-temperature dosed alkali/semiconductor interfaces are very susceptible to contamination. The pressure during alkali dosing did not rise above ~$1x10^{-10}$ torr, and during annealing the pressure also remained below ~$1x10^{-10}$ torr. As our experience with sample preparation techniques increased, the maximum pressures in later experiments correspondingly improved to $7x10^{-11}$ torr for dosing and $9x10^{-11}$ torr for annealing. The cleaver, getter, cylindrical mirror analyzer (CMA), and LEED optics all are in the same analysis chamber, in order to avoid outgassing from moving the AM-dosed sample between chambers and opening valves. The analysis chamber is attached to the incoming synchrotron beam port. For annealed cleavable surfaces, the Si samples were pre-cleaned at 700 K for at least 12 hours in a UHV preparation chamber connected to the analysis chamber by a valve.

All Si(111) surface samples were cleaved *in situ* from 5x5x12mm^3 crystalline Si bars of using a knife-and-anvil technique. A cleaver apparatus on a port aligner is moved around the bar and the bar is moved against a metal stop or "anvil". The "knife" is a diamond blade which is translated on a feedthrough to press up against the other side of the bar, and then a ~1 mm thick piece of the bar is cleaved off along the (111) cleavage planes of Si (parallel to the surface). The surface on the remaining part of the bar is our sample surface, and is visually checked to be flat and mirror-like before inspecting via low-energy electron diffraction (LEED). Using cleaved surfaces removed the necessity to prepare the clean sample by flashing at high temperature, as required for 7x7, since the clean 2x1 reconstruction is readily formed by room temperature cleaving. All samples were cut and oriented in the chamber so that the top face is normal to the $(1\bar{1}0)$ direction and the side faces are normal to the $(11\bar{2})$ direction. Three batches of Si bars were used: *p*-type Si of resistivity 0.048 Ω-cm, *p*-type Si of resistivity 26 Ω-cm, and *n*-type Si of resistivity 1-10 Ω-cm.

Before dosing, the quality of the cleaved surface was checked using LEED, and only surfaces with good single-domain 2x1 LEED patterns were dosed with alkali metal. Alkali metal (Na, K, or Cs) was evaporated upon the samples by resistively heating a well-outgassed SAES chromate getter. Heating drives a reduction reaction which releases alkali atoms from the chromate, and reproducible adatom coverages can be achieved by monitoring the time that the getter is heated. The distance from the getter to the Si(111) surface was kept at ~3.5 cm for most samples to avoid heating of the sample surface from the evaporator while limiting the required dosing time and pressure; earlier experiments used a closer distance near 1 cm and correspondingly shorter dosing times, but gave similar experimental results.

Table 2.1 lists the dosing and annealing conditions for each of the AM/Si(111) interfaces whose atomic geometry is determined using X-ray Standing Waves (XSW). The proposed adsorbate and substrate geometries are analyzed and discussed in Chapters 5-8. These interfaces were prepared either by annealing a saturation-coverage dosed surface or by room-temperature dosing to saturation coverage or less. Si bars for the annealed Na/Si(111)3x1 and K/Si(111)3x1 interfaces were pre-annealed before cleaving to avoid significant outgassing during the post-dosing anneal. The cleaved surfaces were dosed to saturation coverage at room temperature, with a typical dosing time of 8 minutes broken into two 4-minute sessions to keep the pressure low. Saturation coverage surfaces exhibit a 1x1 LEED pattern; however, this was not checked for most samples as the saturation coverage surface is very susceptible to oxygen contamination. The saturation-dosed sample then was resistively heated right

after dosing, and the temperature was monitored using a typical chromel-alumel thermocouple. The temperature was kept above 580°C for 5-10 min, and the peak temperature ranged from 600°C to 660°C. Upon cooling, the LEED pattern becomes 3-domain 3x1 for both the Na/Si(111) and K/Si(111) surfaces. Then all of the data were collected with the sample at room temperature. The 3x1 pattern also can be formed by dosing the sample while it is hot; however, the dosing time is increased as well as the pressure, which increases the risk of contamination.

The room-temperature (RT) dosed interfaces Na/Si(111)1x1, K/Si(111)3x1, and Cs/Si(111)$\sqrt{3}$x$\sqrt{3}$–R30° were formed by dosing the alkali metal on the cleaved Si(111)2x1 surface for a predetermined time. Of these three interfaces, only Na/Si(111)1x1 occurs at saturation coverage. The correct dosing times to produce these interfaces first were determined from separate alkali dosing progression experiments, which were performed on the Si(111) surface for all three alkali metals. Typical dosing times were 1.5 to 2 min per dose, and between 6 and 8 doses were required to saturate the surface, with variations depending on the alkali species being evaporated. After each dose, the LEED pattern was observed, and photoemission spectroscopy (PES) and work function (WF) difference spectra were collected. These dosing progressions were repeated on at least three samples for each alkali metal to ensure reproducibility and to increase the confidence in the dosing limits for each observed "surface phase", which is characterized by a LEED pattern. The variations in LEED, PES, and WF difference results with coverage for the three alkali metals on the AM/Si(111) interface provide information on the adsorption process, including the effect of varying alkali adatom size. The results of these experiments are given in Chapter 4.

Photoemission Spectroscopy and Work Function Difference Measurements

The photoemission spectroscopy (PES) and work function (WF) difference measurements for the alkali (Na, K, and Cs) dosing progressions were taken on Beam Line 8-1 at the Stanford Synchrotron Radiation Laboratory (SSRL). The incident beam was monochromatized using a 822.6 line/mm toroidal grating monochromator (TGM), and exit slits downstream of the TGM were set to 100μm in both vertical and horizontal directions. A Phi double-pass cylindrical mirror analyzer (CMA) analyzed the photoelectron yield, and the sample surface was oriented at an angle of 45° from both the incident beam and the CMA axis. The detection solid angle of the detector is a cone of angles 42.3° ± 6° about the CMA axis, which is somewhere between angle-resolved

and angle-integrated detection. Photoemission counts were normalized to the incident photon flux, which was measured by the drain current of a thin Ni grid placed in the incident beam's path.

The change in the secondary electron cutoff with AM coverage provided WF difference data. Electrons at the secondary electron cutoff have suffered energy loss in traveling to the surface and barely escape the surface, with a total energy at the vacuum level of the sample. The kinetic energy at the cutoff is $\Phi_{sample} - \Phi_{analyzer}$, i.e. the difference between sample and analyzer work functions. Since the analyzer work function does not change, the change in the energy of the secondary electron cutoff with AM coverage is equal to the change in the work function of the sample due to the AM. Two standard "6 V" lantern batteries in series biased the sample -12.31 V relative to the CMA ground for the cutoff measurements, since $\Phi_{analyzer} > \Phi_{sample}$. The batteries' voltage was checked periodically and did not change throughout the experimental run.

Table 2.2 lists the photoemission peaks studied for the three AM/Si(111) interfaces and the photon energies at which the spectra were collected. The photon energy of 145 eV for the Si 2p spectra was chosen to provide high surface sensitivity, as the inelastic escape depth of photoelectrons at 40 eV kinetic energy is near the minimum on the "universal curve". The published escape depth at this energy is 4.7 ± 1.5 Å [1], corresponding to 1.5 ± 0.5 Si layers. Core-level photoemission is sensitive to the chemical environment of the emitting atoms, and atoms in different sites or chemical environments are shifted in energy with respect to each other. By examining changes in the magnitudes and energy shifts of the components making up the alkali and silicon core-level spectra lineshapes as alkali coverage increases, we can deduce changes in the alkali adsorption sites and the Si surface reconstruction. In addition, the overall intensity of the normalized alkali core-level peaks (Na 2p, K 3p, Cs 4d and Cs 5d) is used to determine the alkali coverage. Since AM/semiconductor interfaces have a saturation alkali coverage, the coverage of a particular interface in the dosing progression can be determined by normalizing the alkali core-level peak intensity by the peak intensity for saturation coverage. This is the method used to define the coverages in Chapter 4. Figure 2.1 shows the linear increase in K 3p peak intensity with potassium dosing time up until saturation for the K/Si(111) interface, as well as the WF difference curve. Both curves are characteristic of all the AM/Si(111) interfaces studied. An idle time of 35 sec was subtracted from the overall time the evaporator was on for each dose, and the apparent nonlinearity near 200 sec dosing time can be explained by error in this idle time for shorter dosing times. Valence band (VB) spectra

were used to look at changes in the Si surface state at the top of the valence band, and to check for oxygen contamination after each dose, whose signature is a significant oxide peak at ~5 eV kinetic energy below the valence band maximum. As will be discussed in Chapter 4, contamination was observed in the VB spectra at the highest doses for the discussed potassium dosing progression, but the sodium and cesium dosings showed no signs of contamination. Each of the observed LEED patterns also was achieved by "one shot" dosing on the clean surface and showed no oxide peak in the VB, indicating that the appearance of the observed LEED patterns was not related to the amount of oxygen contamination.

LEED Measurements

After seeing some of the new surface LEED patterns during our PES and WF difference study of increasing K doses on the cleaved Si(111) surface, we did some additional dosing progressions off-line of Beam Line 8-1 using LEED to characterize the surface after each dose. By removing the PES and WF measurements after each dose we reduced the overall duration of the experiment and thus the amount of oxygen contamination. The incident electron beam is normal to the surface and has a tunable energy from 20 to 200 eV, which is near the minimum of the "universal curve" to ensure that diffracted beams originate almost entirely from diffraction off the surface lattice. The LEED pattern is formed by diffracted electron beams hitting the fluorescent screen, and it is a direct representation of the reciprocal lattice of the sample surface. LEED patterns were imaged using the analysis chamber's Princeton Research reverse-view LEED optics. The reverse-view LEED allowed a clear field of view for photographs, which were taken with 30 sec exposure time with a camera mounted on the window to the LEED. For each pattern, photographs typically were taken at three incident electron beam energies, near 45 eV, 65 eV, and 100 eV. The filament current was ~1 mA, and we tried to take pictures quickly to avoid damage to the surface due to the electron beam. Again, the clean Si(111) surfaces were checked for a good single-domain 2x1 pattern before dosing was performed, and the clean surface was photographed as well. Most LEED patterns observed appeared over a beam energy range of ~25 eV to $\geq$ 120 eV and over the entire sample. When the LEED pattern did not appear over the entire sample, visible steps or roughness on part of the surface explained the lack of a spatially continuous pattern.

X-ray Standing Wave Measurements

X-ray Standing Wave (XSW) data were collected in the backreflection mode[2-10] using the same chamber and instrumentation as for the LEED and photoemission spectroscopy (PES) measurements. Figure 2.2 depicts the experimental setup for the XSW experiment as well as samples of the various spectra that are collected as a function of photon energy. The sample is aligned so that incident photons are normal to the (111) or ($11\bar{1}$) Bragg planes of Si and monochromatized using a pair of InSb(111) crystals on the soft X-ray beam line 3-3 (JUMBO) at SSRL. JUMBO has three primary optical components - an entrance slit, a focusing mirror, and the double-crystal monochrometer[11-13]. All components are in ultra-high vacuum. The size of the entrance slit can be adjusted to improve angular resolution at the expense of cutting beam intensity. The mirror, which is a platinum coating on a quartz crystal, is curved in directions lateral and transverse to the beam in order to focus the beam at the sample position in both vertical and horizontal directions. The position of the mirror is such that the beam spot at the sample (1.5 mm vertical x 2.5 mm horizontal) is a unity-magnification image of the beam at the source. In between the mirror and sample positions is the double-crystal monochrometer system, which selects the photon energy of the beam. Precision goniometers are connected to each of the crystals, and their motion is controlled by computer. First the crystal is translated along the beam direction and rotated to select the correct Bragg geometry for the desired photon energy. Then the upper is rotated until maximum intensity is achieved. A feedback circuit connected to I_0 channeltrons ensures maximum intensity at each photon energy. The desired photon energy of 1977 eV corresponds to a Bragg angle of 57° from the InSb(111) crystal surface. The angular resolution of the beam at this energy is between 50 and 100 arc seconds[11-12], and our fits to the measured reflectivity determine an energy width of 0.7 eV (Gaussian full-width at half-maximum).

Before collecting XSW data, a photoemission scan is taken with photon energy near the Bragg energy of 1977 eV to locate the photoemission or Auger peak of interest (Figure 2.2(a)). The peaks used were the Na 1s, Cs $3d_{3/2}$, and Si 1s photopeaks at binding energies –1070.8 eV, –740.5 eV, and –1839.3 eV, respectively, and the K LMM Auger peak at 245 eV kinetic energy. Near 1977 eV, the Si 1s photoelectrons are highly surface sensitive, with a kinetic energy near the minimum of the universal curve, so the corresponding XSW data give information about the surface Si atomic geometry. After the energy of the peak is determined, a number of spectra are taken simultaneously as the photon energy is scanned through the Si(111) Bragg condition. The sum of the incident and Bragg-reflected X-ray flux is monitored by amplifying the

emission current of an Ni grid collected with a channeltron (Figure 2.2(b)). Then the XSW absorption yield of alkali metal or Si atoms as a function of photon energy is monitored via the total counts at the peak with the CMA (Figure 2.2(c)). For photoemission peaks kinetic energy is tracked as the photon energy changes (constant initial state mode), while for Auger peaks the kinetic energy is kept constant with changing photon energy (constant final state mode). Background standing wave scans are recorded slightly above the peak (higher kinetic energy) and the background XSW data are collected in a separate run immediately after the on-peak XSW data (Figure 2.2(d)). This background XSW yield reflects inelastically scattered bulk electrons and also varies with photon energy, and is subtracted from the on-peak XSW yield to give the specific signal of interest (Figure 2.2(e)). This subtracted spectra is then fitted to the XSW equation, as described in Chapter 3. Total electron yield data are recorded concurrently by monitoring the amplified drain current from the sample (Figure 2.2(f)). The total electron yield signal has an XSW signal characteristic of bulk Si since it consists primarily of inelastically scattered electrons from the bulk. Its expected lineshape therefore is well-determined, and the total yield data can be used as a check on the overall quality of the XSW data collected.

Both (111) and (11$\bar{1}$) diffraction planes were used for backreflection XSW, and in most cases the XSW data set for one reflection were taken on the same surface immediately after taking the full data set for the other reflection. The Bragg energy for the two reflections is identical. The geometry of the two reflections is shown in Figure 2.2. The (111) reflection is taken with the surface normal to the incident beam, while the (11$\bar{1}$) reflection has the sample turned towards the analyzer so the incident photons are at an angle of 70.53° with respect to the surface normal. In the horizontal plane, the CMA axis is 90° from the incident photon and parallel to the bulk reflecting planes. The radiation has an inherent polarization in the horizontal plane of the synchrotron ring. This geometry corresponds to the case of σ polarization, where the incident and reflected electric fields are collinear and perpendicular to the plane formed by the incident and reflected photon momenta. Oxygen contamination was checked periodically via O 1s photoemission, as reasonable valence band spectra were not available at this high photon energy. We tried to take the XSW data in as short an amount of time as possible to get reasonable fit results, in order to avoid contamination of the surface, which is still susceptible to contamination over the time frame of an 8-hour XSW run. This and the small peak height produced by an alkali coverage of 1/3 monolayer (ML) to 1 ML accounts for the roughness of the alkali metal XSW data presented.

References

[1] C. M. Garner, I. Lindau, C. Y. Su, P. Pianetta, and W. E. Spicer, Phys. Rev. B 19 (1979) 3944.

[2] D. P. Woodruff, Prog. Surf. Sci. 57 (1998) 1.

[3] B. W. Batterman and H. Cole, Rev. Mod. Phys. 36 (1964) 681.

[4] J. C. Woicik, T. Kendelewicz, K. E. Miyano, P. L. Cowan, C. E. Bouldin, B. A. Karlin, P. Pianetta and W. E. Spicer, Phys. Rev. Lett. 68 (1992) 341.

[5] T. Kendelewicz, J. E. Klepeis, J. C. Woicik, S. H. Southworth, C. Mailhiot, M. van Schilfgaarde, M. Methfessel, A. Herrera-Gómez, and K. E. Miyano, Phys. Rev. B 51 (1995) 10774.

[6] T. Kendelewicz, P. Liu, G. E. Brown, Jr. and E. J. Nelson, Surf. Sci. 395 (1998) 229.

[7] J. C. Woicik, T. Kendelewicz, S. A. Yoshikawa, K. E. Miyano, G. S. Herman, P. L. Cowan, P. Pianetta and W. E. Spicer, Phys. Rev. B 53 (1996) 15425.

[8] J. C. Woicik, T. Kendelewicz, A. Herrera-Gómez, K. E. Miyano, P. L. Cowan, C. E. Bouldin, P. Pianetta, and W. E. Spicer, Phys. Rev. Lett. 71 (1993) 1204.

[9] J. C. Woicik, T. Kendelewicz, A. Herrera-Gómez, A. B. Andrews, B. S. Kim, P. L. Cowan, K. E. Miyano, C. E. Bouldin, B. A. Karlin, G. S. Herman, J. L. Erskine, P. Pianetta, and W. E. Spicer, J. Vac. Sci. Tech. A 11 (1993) 2359.

[10] J. C. Woicik, T. Kendelewicz, K. E. Miyano, P. L. Cowan, C. E. Bouldin, B. A. Karlin, P. Pianetta, and W. E. Spicer, Phys. Rev. B 44 (1991) 3475.

[11] Z. Hussain, E. Umbach, D. A. Shirley, J. Stöhr, and J. Feldhaus, Nucl. Inst. Meth. 195 (1982) 115.

[12] J. Cerino, J. Stöhr, N. Hower, and R. Z. Bachrach, Nucl. Inst. Meth. 195 (1980) 227.

[13] F. D. Dikmen, "Documentation on the Operation and Performance of the Double Crystal Monochrometer - JUMBO", Stanford Synchrotron Radiation Laboratory beamline 3-3 manual, 1981.

Table 2.1(a). Dosing and annealing conditions for the Na/Si(111) interfaces whose atomic geometry is determined using X-ray Standing Waves (XSW).

Sample	Coverage % of photopeak intensity at saturation and ML (monolayers)	Dosing Conditions: Getter Current, Time, and Distance to Sample	Maximum Dosing Pressure	Annealing Conditions: Filament Current, Time, and Temperature	Maximum Annealing Pressure
Na/Si(111) 1x1	100% 1.00 ML Na	*Si 1s XSW data:* 5.7 A 2 doses, 5 min each 3.8 cm *Na 1s XSW data:* 5.5 A 2 min 0.8 cm	*Si 1s XSW data:* $3x10^{-10}$ torr *Na 1s XSW data:* $1x10^{-10}$ torr	Not annealed	Not annealed
Na/Si(111) 3x1	25% to 31% 0.25 ML to 0.31 ML Na	5.7 A 2 doses, 4 min each 3.8 cm	$9x10^{-11}$ torr	4.2 A 5-10 min above 580°C maximum 600-660°C	$9x10^{-11}$ torr

Table 2.1(b). Dosing and annealing conditions for the K/Si(111) and Cs/Si(111) interfaces whose atomic geometry is determined using X-ray Standing Waves (XSW).

Sample	Coverage % of photopeak intensity at saturation and ML (monolayers)	Dosing Conditions: Getter Current, Time, and Distance to Sample	Maximum Dosing Pressure	Annealing Conditions: Filament Current, Time, and Temperature	Maximum Annealing Pressure
Annealed K/Si(111) 3x1	30% to 42% 0.27 ML to 0.38 ML K	5.8 A 2 doses, 4 min each 3.8 cm	$9x10^{-11}$ torr	4.2 A 5-10 min above 580°C maximum 600-660°C	$9x10^{-11}$ torr
Room-temp. K/Si(111) 3x1	51% to 74% 0.46 ML to 0.67 ML K	5.7 A 3 min 3.8 cm	$8x10^{-11}$ torr	Not annealed	Not annealed
Cs/Si(111) $\sqrt{3}x\sqrt{3}$-R30°	56% to 88% 0.30 ML to 0.48 ML Cs	5.8 A 2 min 40 sec 3.8 cm	$1x10^{-10}$ torr	Not annealed	Not annealed

Table 2.2. Photoemission peaks studied for the three AM/Si(111) interfaces and the photon and photoelectron kinetic energies at which the spectra were collected. Analyzer energy resolution is 1.6% of the analyzer pass energy, e.g. 10 eV pass energy corresponds to 0.16 eV resolution.

Photopeak	Photon Energy (eV)	Nominal Binding Energy (eV)	Photoelectron Kinetic Energy (eV)	Pass Energy (eV)
Na $2p_{1/2}$	77	30.4	41.0	10
Na $2p_{3/2}$	77	30.5	41.1	10
K $3p_{1/2}$	65	18.3	41.8	15
K $3p_{3/2}$	65	18.3	41.8	15
Cs $4d_{3/2}$	120	79.8	36.2	10
Cs $4d_{5/2}$	120	77.5	38.6	10
Cs $5p_{1/2}$	65	14.2	46.8	15
Cs $5d_{3/2}$	65	12.1	48.9	15
Si $2p_{1/2}$	145	99.8	40.8	10
Si $2p_{3/2}$	145	99.2	41.4	10
Valence Band (Na experiment)	65 and 20.8	0-12 and 0-7	49-61 and 10-17	15
Valence Band (K experiment)	65	0-12	49-61	15
Valence Band (Cs experiment)	65 and 20.8	0-12 and 0-7	49-61 and 10-17	15

Figure 2.1. K 3p peak intensity and work function difference plotted versus potassium dosing time. The plotted dosing time is the actual time the evaporator was on minus an idle time of 35 sec. Note the linear increase in the peak intensity and then saturation corresponding to a full layer of K. Both curves are characteristic of all the AM/Si(111) interfaces studied.

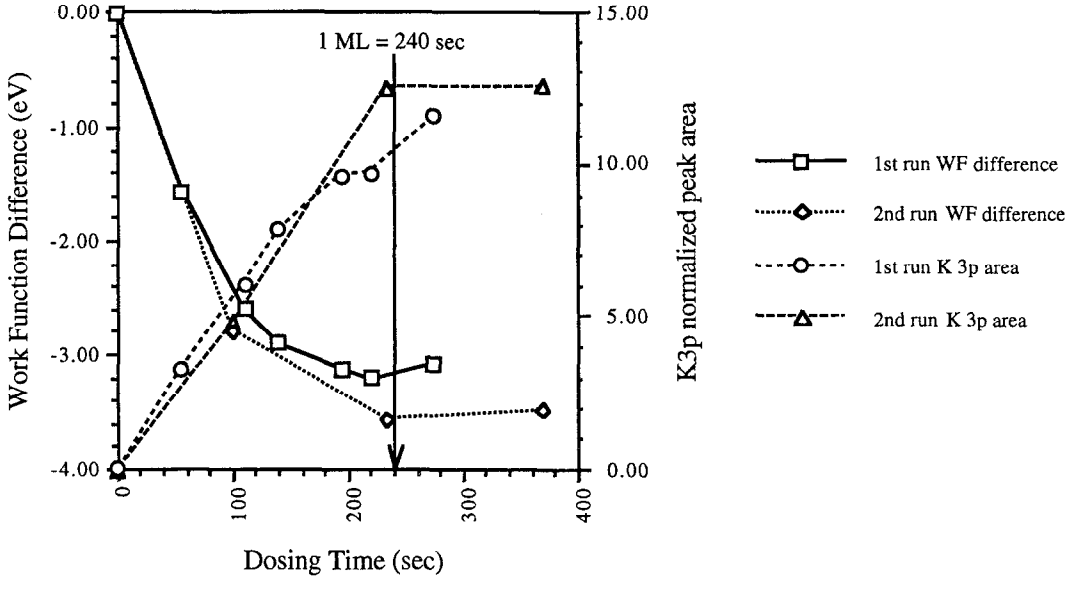

Figure 2.2. Experimental setup for the X-ray Standing Wave (XSW) experiment, as well as samples of the various spectra. The backreflection energy for the (111) planes of Si is 1977.16 eV. (a) Na 1s photoemission data collected at hν = 1985 eV, above the Bragg condition. (b) Sum of incident and reflected X-ray intensities. (c) On-peak photoelectron yield versus photon energy. Detected binding energy = 1074.3 eV. (d) Above-peak background yield versus photon energy. Detected binding energy = 1070 eV. (e) Subtracted data, on-peak minus background. (f) Total yield versus photon energy.

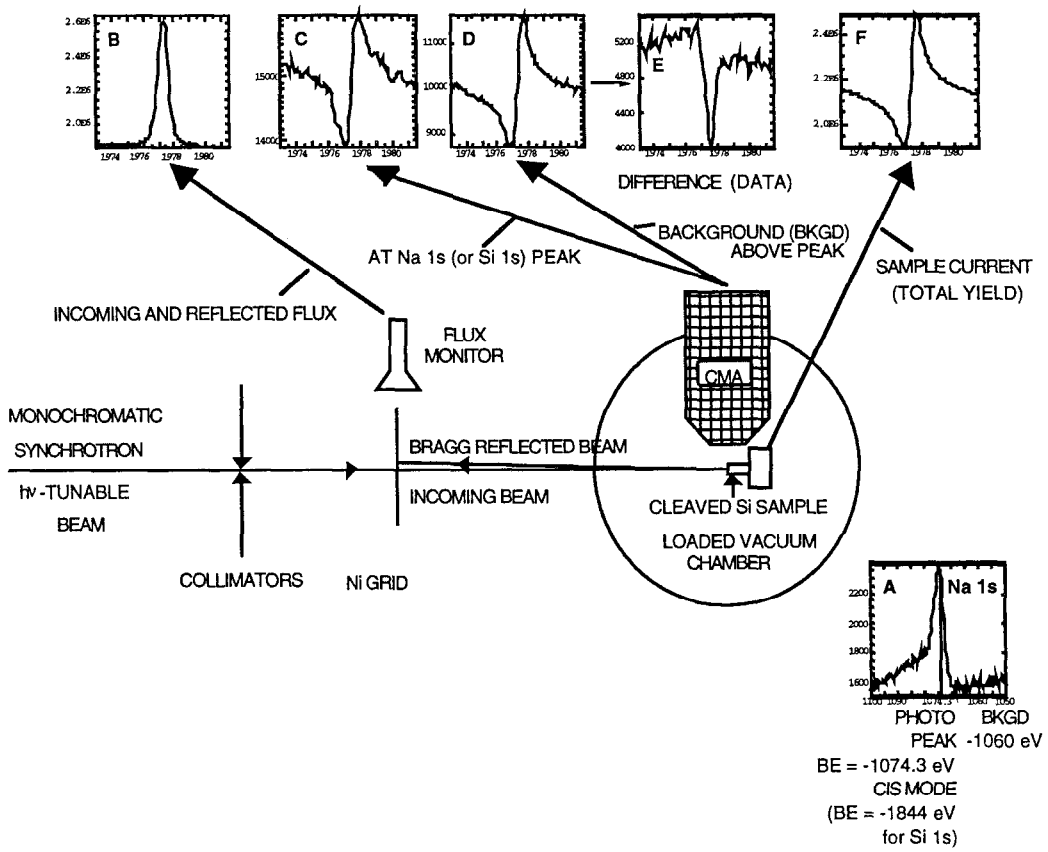

Figure 2.3. The sample and detector geometry for the (111) and (11$\bar{1}$) reflections. In both cases the incident X-ray is back-reflected off of the diffracting plane.

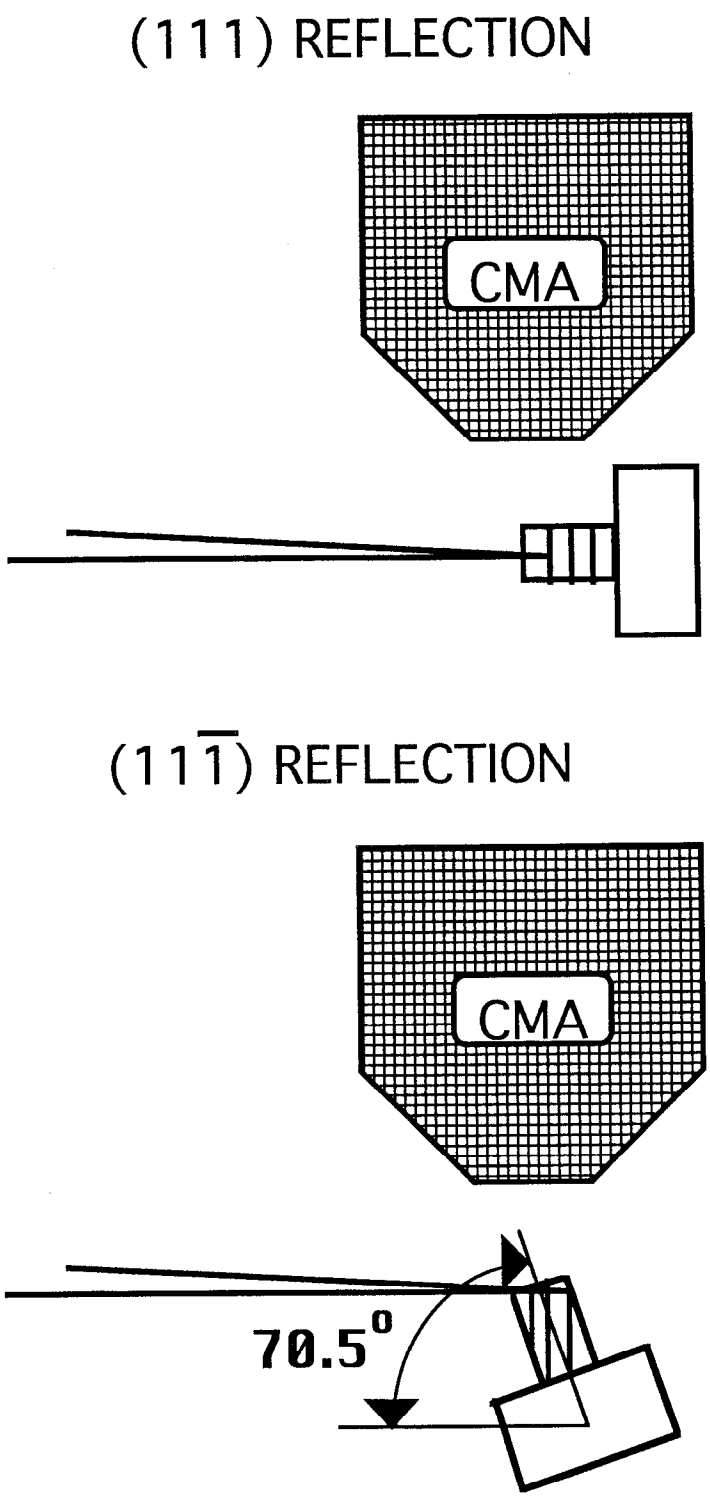

CHAPTER THREE

AN EXPLANATION OF THE BACKREFLECTION X-RAY STANDING WAVE TECHNIQUE

Formation of the X-ray Standing Wave

This chapter presents the formalism behind the X-ray standing wave (XSW) technique, as well as describing some of the specific applications of the technique used in the experiments of Chapters 5-9. The name of the technique refers to the standing wave set up as an interference between incoming and reflected X-rays. However, the XSW technique combines this X-ray diffraction with X-ray absorption and is therefore an energy-resolved and element-specific technique, unlike X-ray diffraction alone. The diffraction aspect allows the determination of the positions of the energy-selected atoms to a high degree of precision, usually on the order of 0.1 Å or less. Thus X-ray standing waves is an excellent way to determine the atomic geometry of adsorbate atoms upon a substrate of different atomic number Z, and this will be one of the primary uses of the XSW technique in our study of the AM/Si(111) surfaces. As described below, the back-reflection energy of the (111) reflection of Si is fortunately low enough to make Si 1s photoemission yields surface sensitive, and our other

primary use of XSW will be to determine Si surface atom geometries by exploiting this surface sensitivity.

In order to create the standing wave, the reflected X-ray is produced via Bragg reflection off of the bulk crystal lattice. The requirement upon the X-ray wavelength to create the reflected X-ray is the Bragg condition:

$$\lambda = 2d\cos\theta \tag{1}$$

where λ is the X-ray wavelength, d is the spacing between atomic lattice planes, and θ is the angle between the incident X-ray and the normal to the lattice plane. This condition requires the difference in path length between X-rays scattering off of neighboring planes to be equal to a wavelength so that the two X-rays interfere coherently. The diffracting plane spacing $d = 1/|\mathbf{H}|$, where $\mathbf{H}$ is the reciprocal lattice vector for the reflection, and points normal to the diffracting plane. In all of the experiments to follow, we are in the backreflection geometry (θ=0), and therefore

$$\lambda = 2d\,(\text{backreflection}) \tag{2}$$

The incident and reflected wave have the same wavelength and therefore the same wavevector magnitude, although the directions are different. In equation form,

$$|\mathbf{k}_H| = |\mathbf{k}_0 + \mathbf{H}| = |\mathbf{k}_0| \tag{3}$$
$$\mathbf{k}_H = -\mathbf{k}_0\,,\ \mathbf{H} = \mathbf{k}_H - \mathbf{k}_0 = -2\mathbf{k}_0\,(\text{backreflection})$$

where the second equation only applies to the backreflection configuration.

Equation (3) is true for the kinematic theory of X-ray diffraction, where the scattering of waves in a selected region of the sample is independent of wave scattering in the neighboring regions. This is not true for a bulk crystal, where the periodicity of the crystal necessitates the consideration of waves strongly scattering multiple times forwards and backwards off of the lattice and interfering with other scattered waves. In this case, the total wave field inside the crystal must be considered, and dynamical diffraction theory is used to describe the resulting standing wave within the crystal. The derivation of the ratio of incident and reflected electric field amplitudes E_H/E_0 inside a periodic crystal has been performed several times in the literature[1-3]. It involves expressing the total vector field $\mathbf{A}$ as a periodic Bloch wave and the periodic charge density of the crystal as a Fourier series, and then solving Maxwell's equations for the

electric field within the crystal. Both series are indexed by the reciprocal lattice vectors **H**. As a result, the magnitudes of the incident and reflected wavevectors are no longer required to be exactly equal, but equal to a factor of $\Gamma F_H \approx 10^{-5}$ to one. F_H is the X-ray structure factor (Fourier component of crystal charge density) for the bulk crystal for the reflection **H**, and $\Gamma = e^2\lambda^2/4\pi^2\varepsilon_0 mc^2 V = r_{electron}\lambda^2/\pi V$ is a constant relating the structure factor to the dielectric function. This slight relaxation of equation (3) results in a finite width in angle and energy for the reflectivity $R=|E_H/E_0|^2$. More importantly, across this width the phase ν between the incident and reflected waves is well-defined and changes by π. In general, the phase and reflectivity are functions of incident photon angle and energy; however, the angular dependence is removed near backreflection. The expression for the complex ratio of the incident and reflected electric field amplitudes is [2]

$$\frac{E_H}{E_0} = \sqrt{R(E)}e^{i2\pi\nu(E)} = \sqrt{\frac{F_H}{F_{\bar{H}}}}(\eta \pm \sqrt{\eta^2 - 1}) \qquad (4)$$

The reflectivity R is squared magnitude of this complex ratio, while argument of the phase factor of this ratio is $2\pi\nu$. Both reflectivity and phase are functions of the photon energy E. The complex variable η is given by the expression [2]

$$\eta = \eta(E) = \frac{2\dfrac{(E - E_B)}{E} - \Gamma F_0}{\Gamma\sqrt{F_H F_{\bar{H}}}} \qquad (5)$$

Here F_0, F_H, and $F_{\bar{H}}$ are the complex structure factors for the (000) reflection and the reflections along **H** and **–H**, and $\Gamma = r_{electron}\lambda^2/\pi V$ as above. E is the photon energy, and $E_B = hc/(2d \cos\theta) = |\mathbf{H}|hc/(2\cos\theta)$ is the kinematic Bragg energy for the reflection. Far from the Bragg condition, η is large in magnitude, and the two terms in parentheses in equation (4) cancel to give zero reflectivity.

Figure 3.1(a)-(b) plot the theoretical reflectivity and phase as a function of photon energy for the (111) reflection of Si in the backreflection geometry, which is identical to the result for the $(11\bar{1})$ reflection due to the tetrahedral symmetry of the Si crystal structure. The (111) and $(11\bar{1})$ are the two reflections used in our X-ray standing wave measurements of the AM/Si(111) surfaces. The plane spacing is d = 3.135 Å, and the corresponding Bragg energy is 1977.16 eV. As seen from Figure 3.1(a), the peak of the reflectivity is shifted to 1977.31 eV. In addition, the peak has a finite width, with a height of 0.43 and a full width at half maximum (FWHM) of 0.21

eV. The shift and finite width are a result of dynamical diffraction theory and not experimental resolution, which is not included in Figure 3.1(a). The value of the phase $2\pi\nu$ between the incident and reflected waves is 1.14 π for photon energies below the reflection, and 0.14 π above the reflection. A change in phase by π occurs as the photon energy is swept across the width of the reflectivity (Figure 3.1(b)).

The backreflection standing wave intensity I at a position **r** in the crystal is found by squaring the superposition of the incident and standing waves:

$$I = |\mathbf{E}_H + \mathbf{E}_0|^2 = |E_0|^2 \left|1 + \frac{E_H}{E_0} e^{-2\pi i \mathbf{H}\cdot\mathbf{r}}\right|^2 = |E_0|^2 \left|1 + \sqrt{R(E)} e^{2\pi i(\nu(E) - \mathbf{H}\cdot\mathbf{r})}\right|^2 \quad (6)$$

For backreflection, the directions of the incident and reflected electric field are identical, and the $\exp(-2\pi i \mathbf{H}\cdot\mathbf{r})$ term is the phase difference due to the difference in wavevector $\mathbf{k}_H - \mathbf{k}_0 = \mathbf{H}$ between the incident and reflected waves. Expanding the square and dividing by the incident wave intensity gives

$$I / I_0 = 1 + R(E) + 2\sqrt{R(E)} \cos(2\pi(\nu(E) - \mathbf{H}\cdot\mathbf{r})) \quad (7)$$

So the standing wave intensity varies in space with wavelength $1/|\mathbf{H}|$, and the magnitude and position of the intensity extrema with respect to the crystal diffracting planes are determined by the dynamical diffraction theory results for R(E) and ν(E), respectively. As the photon energy is swept through the reflectivity and the phase $2\pi\nu$ decreases by π, the intensity extrema shift inward (opposite to **H**) by half a wavelength. Since the phase starts near π and ends near 0 as photon energy is increased, the standing wave maxima start close to halfway between the diffracting planes and end almost coincident with the diffracting planes.

As mentioned above, using the back-reflection configuration ($\mathbf{k}_H = -\mathbf{k}_0$) removes the angular dependence of the reflectivity. The more general expression for the reflectivity includes angular coefficients in front of equation (4) and in front of each term in the numerator of equation (5). However, these coefficients all depend on the cosines of the angles between $\mathbf{k}_0$, **H**, and the surface normal **n**. These cosines all equal 1 for the back-reflection case where $\mathbf{k}_0 \parallel -\mathbf{n}$, and the ratio of cosines equals 1 for back-reflection even when the diffracting plane and surface plane are not parallel. More importantly, the derivative of these terms with respect to angle are close to zero, so the reflectivity becomes insensitive to angle. The angular width of the reflectivity curve in the back-reflection configuration is on the order of a degree of arc, while the

corresponding width away from the back-reflection condition is on the order of tens of arc seconds. The relaxation of angular restrictions to produce a strong reflection makes the back-reflection version of the X-ray standing wave technique much more insensitive to imperfections in the sample crystal (although not a problem for our crystalline Si samples), as well as allowing the technique to be used on synchrotron beamlines with less ideal angular collimation properties, such as beamlines normally used for X-ray absorption fine structure (EXAFS) experiments. In addition, the experiment can be performed using a fixed sample geometry and without precision goniometers. Synchrotron beamlines have the ability to vary the photon energy with an energy resolution comparable to the theoretical reflectivity energy width, and are used for our backreflection XSW experiments.

Absorption in a X-ray Standing Wavefield: Derivation of the Standing Wave Equation

Since X-ray standing wave intensity pattern is well-defined relative to the bulk crystal diffracting planes, the X-ray standing wavefield can be used to determine the distances of absorbing atoms from these planes. As the standing wavefield extends both into the bulk crystal and outside the crystal surface, both bulk and surface atoms can be studied. The yield of an absorption channel as the photon energy is swept through the Bragg condition will have a characteristic lineshape dependent on the absorbing atoms' positions. The intensity needs to be proportional to the absorption cross section. Therefore, photoemission, Auger emission, total electron yield, secondary electron yield, and fluorescence are among the possible absorption channels which can be monitored. Photoemission, Auger, and fluorescence yields are energy-analyzed and therefore element-specific. By using these yields, the signal from adsorbate or impurity atoms can be separated from the bulk signal and their positions determined. Thus X-ray standing waves is well-suited to our study of alkali metal adsorption upon the Si(111) surface.

The differential absorption cross section is proportional to

$$\frac{d\sigma}{d\Omega} \propto \left| E_0 < f | e^{i\mathbf{k}_0 \cdot \mathbf{r}} \varepsilon_0 \cdot \nabla | i > + E_H < f | e^{i\mathbf{k}_H \cdot \mathbf{r}} \varepsilon_H \cdot \nabla | i > \right|^2 \qquad (8)$$

$$\frac{d\sigma}{d\Omega} \propto \left| \begin{array}{l} < f | \exp(i\mathbf{k}_0 \cdot \mathbf{r}) \varepsilon_0 \cdot \nabla | i > \\ + \sqrt{R(E)} \exp(i(\nu(E) - 2\pi(\mathbf{H} \cdot \mathbf{R}))) \times < f | \exp(i\mathbf{k}_H \cdot \mathbf{r}) \varepsilon_H \cdot \nabla | i > \end{array} \right|^2$$

The absorption cross-section is related to the square of the sum of two matrix elements between the initial and final electronic states. The two elements involves the interaction

of the electron momentum with the incident and reflected electric fields. The pre-factor of the second term describes the relationship between the incident and reflected electric field amplitudes. The position **R** in this pre-factor is the center of the initial state charge distribution, which corresponds to the center of the atomic core for core-level initial states. **r** within the matrix element is the electron position relative to this central position **R**. No approximation has been made to get the pre-factor of equation (8); it comes about from a change of position variables from the coordinate space of the lattice to the coordinate space centered on the absorbing atom, i.e. in symbolic form

$$\mathbf{r}' \text{ (lattice)} \rightarrow \mathbf{r}' - \mathbf{R} = \mathbf{r} \text{ (atom)} \tag{9}$$

The equation for the energy dependence of the absorption yield profile is very similar to the standing wave intensity profile of equation (7). For initial core-level states, the dipole approximation is assumed, that is, the electric field does not vary rapidly over the extent of the initial state. In symbolic form,

$$\exp(i\mathbf{k}\cdot\mathbf{r}) \approx 1 \tag{10}$$

Using $\varepsilon_0 = \varepsilon_H$ for σ polarization, one can see that the two matrix elements in equation (8) are equal in the dipole approximation. Thus the matrix element can be factored out of the expression. The final result is the "standing wave equation", i.e. the absorption cross section is proportional to

$$\frac{d\sigma}{d\Omega} \propto 1 + R(E) + 2f_c\sqrt{R(E)}\cos(\nu(E) - 2\pi D_c) \tag{11}$$

The absorption intensity depends on the sum of the incident and reflected electric field intensities 1+R(E), plus an interference term (the third term of equation (11)) proportional to $\sqrt{R(E)}$. Since the reflectivity R(E) is less than one, the third term is of comparable size to the other terms in equation (11). Away from the reflection, R–>0 and the absorption yield is proportional to the incident intensity only (the first term of equation (11)). If the absorption yield Y(E) in the standing wave field is divided by the constant yield Y_0 away from the Bragg condition, the normalized yield is equal to

$$Y(E)/Y_0 = 1 + R(E) + 2f_c\sqrt{R(E)}\cos(\nu(E) - 2\pi D_c) \tag{12}$$

The reflectivity R(E) and phase ν(E) are known functions of photon energy, and the measured absorption yield is fit to equation (12) to find the parameters D_c and f_c.

Coherent Distance D_c and Fraction f_c : Meaning and Lineshape Dependence

In the case of single-site adsorption, the coherent distance D_c corresponds to the distance of the absorbing atom from the diffracting plane divided by the diffraction plane spacing (3.135 Å for the (111) planes of Si). The coherent fraction f_c is equal to the fraction of adsorbing atoms situated in the site; the remaining fraction $(1 - f_c)$ of atoms are disordered and their contribution to the interference term (last term of the above equation) averages to zero. Thermal disorder in the absorbing atoms also reduces the coherent fraction by a Debye-Waller factor $e^{-2\pi^2\sigma_H^2}$, where σ_H^2 is the mean squared atomic vibration amplitude in the direction of the reflection **H**.

From the form of the interference term in equation (12), it can be seen that the lineshape of the modulation in the adsorption yield depends upon the coherent distance D_c, which appears as the argument of the cosine. The magnitude of the interference term is proportional to the coherent fraction f_c as well as the square root of the reflectivity $\sqrt{R(E)}$. Figure 3.2(a) shows the dramatic change in lineshape as D_c is changed from 0 to 1. Note that D_c is only known modulo 1 plane spacing due to the periodicity of the cosine term; however, with reasonable assumptions of bond lengths the absolute value of D_c can be determined. Visible changes in the lineshape can be observed for a change in coherent distance of 0.1 plane spacings. This corresponds to a change in absorbing atom position of 0.3 Å for the (111) reflection of Si. This rapid change in lineshape with position is the reason for the high position sensitivity of the X-ray standing wave (XSW) technique. Typical XSW experiments can give a distance resolution of ± 0.10 Å.

Figure 3.2(b) shows the progression of the XSW lineshape for D_c=1 as the coherent fraction f_c is increased over the range of possible values from 0 to 1. A Gaussian with full width at half-maximum of 0.70 eV has been convoluted with the theoretical lineshape in order to simulate what the data would look like in our experiments (this is also done for Figure 3.2(a)). At f_c=0, which is the case of total disorder or incoherence, the lineshape is equal to 1+R(E) and the shape is peaked at the reflectivity maximum. In this extreme case the lineshape is independent of D_c. As f_c is increased, the lineshape develops the characteristic lineshape corresponding to D_c=1, with a minimum followed by a maximum as photon energy increases. This lineshape is distinct visually from the reflectivity in the range f_c = 0.3-0.4. At f_c=1,

which is the case of complete ordering of the atoms, the feature is largest in magnitude, with a minimum-to-maximum height larger than the reflectivity by a factor of 2.9. Figure 3.2(b) shows how improving the ordering of the absorbing atoms can improve the signal and therefore the signal-to-noise ratio of the data. However, even with a substantial degree of disorder ($f_c = 0.3$-0.4), the lineshape and therefore the coherent distance can be determined. With increased disorder of the absorbing atoms, the lineshape is similar to the reflectivity regardless of the actual value of D_c. In addition, since the third term of equation (12) also is proportional to $\sqrt{R(E)}$, strong reflections from a well-ordered bulk crystal samples (such as crystalline Si) produce a larger signal and signal-to-noise ratio than weaker reflections from samples with crystal imperfections or mosaicity. It is interesting to note that the magnitude of the standing wave feature depends both on an X-ray absorption effect (through f_c) and an X-ray diffraction effect (through $\sqrt{R(E)}$).

In the case of multiple sites of the absorbing atoms, the definitions of the coherent distance D_c and coherent fraction f_c are different from the single-site case. Each absorbing atom site *i* contributes an interference term, with the weight of each term determined by the relative populations $f_{c,i}$ and the phase of each term given by the distance $D_{c,i}$ of the site from the diffracting plane; the fraction $1 - \Sigma f_{c,i}$ corresponds to the fraction of atoms in disordered positions. The more general definition of the coherent distance and fraction is the phase and amplitude, of the absorbing atom structure factor. The structure factor F_H for the reciprocal lattice vector **H** is the Fourier component of the absorbing atomic distribution along **H**, and is defined by the equation

$$F_H \equiv f_{c,H} e^{2\pi i D_{c,H}} = e^{-2\pi^2 \sigma_H^2} \sum_j f_{j,H} e^{2\pi i D_{j,H}} \qquad (13)$$

$D_{j,H}$ is the distance of absorbing atom *j* from the diffracting plane divided by the diffracting plane spacing $1/|\mathbf{H}|$, $f_{j,H}$ is the fractional population of atoms *j*, and the sum is over all absorbing atoms, where the index *j* separates atoms with different relative positions $D_{j,H}$. The Debye-Waller factor $e^{-2\pi^2\sigma_H^2}$ is given explicitly and reflects the component of thermal motion of absorbing atoms normal to the diffracting plane; this term is real and contributes only to the coherent fraction $f_{c,H}$. This expression for F_H is similar to the crystal structure factor for X-ray diffraction. However, the usual atomic scattering factor seen for X-ray diffraction is not present, because the XSW technique uses energy discrimination to select a specific photoemission or Auger peak. This insures that all of the absorbing atoms are of the same element, so the atomic scattering

factor is factored out of the sum. If the real part of the above equation (13) is taken, we find the relationship between the sum of the contributions of the individual sites' cosine-like interference terms and the overall coherent fraction and distance of the third term of equation (12).

From the above equation, the coherent distance can be interpreted as a phase-averaged distance of all the absorbing atoms from the diffracting plane, and the coherent fraction represents the extent of constructive or destructive interference among the signals for the different atom populations. In the case of the alkali adatoms, the different distances $D_{j,H}$ of the absorbing atoms can arise from multiple sites and from the mapping of the adatom position into three equivalent domains. The three-domain mapping will not affect the (111) coherent distance or fraction as the adatom height above the surface is the same for the three domains. However, the simulated $(11\bar{1})$ data can be quite different for single-domain versus three-domain adsorption models, with the same adatom position relative to the Si chains in each domain. This multi-domain effect is described in more detail in Chapter 7, which determines the structure of the Na/Si(111)3x1 and K/Si(111)3x1 interfaces, which exhibit multi-domain LEED patterns.

For the specific case of equal populations of atoms in two different absorbing atom positions, the coherent distance D_c is equal to the average atom position

$$D_c = (D_{c,1}+D_{c,2})/2 \qquad (14)$$

and the coherent fraction is related to the spread in the two atom positions $D_{c,1}-D_{c,2}$ by the equation

$$f_c = \cos(\pi(D_{c,1}-D_{c,2})) \qquad (15)$$

Thus, if the two atoms are separated by half a diffraction plane spacing, their contributions to the standing wave absorption yield are exactly out of phase and cause the coherent fraction to vanish, and the absorption yield matches the sum of incident and reflected intensities, 1+R(E).

The bulk structure of Si has two inequivalent atom positions for the (111) and $(11\bar{1})$ reflections due to the bilayer structure along these directions. Bulk Si atoms are located in two layers of equal population, located 1/8 of a plane spacing above and below the (111) or $(11\bar{1})$ plane. Figure 3.3 depicts the $(1\bar{1}0)$ plane projection (side view) of the bulk Si structure as well as the position of the (111) and $(11\bar{1})$ diffraction

planes. Si atoms in different bilayers are located the same distance from the nearest bulk diffraction plane and thus have the same contribution to the overall absorption profile. Using equations (14) and (15), we find that the absorption profile of bulk Si atoms along the (111) and (11$\bar{1}$) reflections can be fit to a single standing wave with D_c = 1 (average position on the planes) and $f_c = \cos(\pi/4) = 1/\sqrt{2} = 0.707$. This bulk profile can be measured via total yield or the electron yield of the off-peak background, which is dominated by inelastically scattered electrons. As an internal check of the quality of the collected XSW data, it was verified that the total yield and background XSW data for all the data sets presented in Chapters 5-9 agreed within error bars with the expected values for the bulk atomic structure (D_c = 1, f_c = 0.69), which is an internal check of the XSW data. The ideal bulk Si of f_c = 0.707 fraction is further reduced to f_c = 0.69 by the thermal Debye-Waller factor for bulk Si at room temperature.

Fitting Procedure

The XSW photoemission yield data are fit to the standing wave equation in order to determine the coherent distance D_C and fraction f_C as fit parameters. First, the reflectivity is fit to the theoretical lineshape convoluted with a Gaussian in order to determine the Gaussian energy width due to the monochrometer and the peak offset from the calculated Bragg energy. The background XSW data are subtracted from the on-peak data to give the variation of the photopeak height versus photon energy. The background data are multiplied by a constant before subtraction to adjust the background yield to its value underneath the photopeak. A straight line is fit to the tails of the subtracted XSW data (outside the Bragg condition) and the standing wave equation is multiplied by the equation for this line to produce a possible fit to the data. The fit is offset in energy and convoluted with the Gaussian energy distribution determined from the reflectivity data. The best fit is chosen through a least-squares technique, and the error bars listed reflect where the χ^2 value is doubled from its minimum value.

Bragg reflections for Alkali Adatom XSW Data

XSW data from two Bragg reflections are collected for the alkali adatoms. The (111) reflection measures the normal component of adatom surface positions (i.e. height above the substrate), while the coherent distance from the (11$\bar{1}$) reflection is predominantly the surface lateral component of adatom positions along the (11$\bar{2}$)

direction. On the cleaved Si(111) surface, the $(11\bar{2})$ direction corresponds to the direction perpendicular to the π-bonded chains of our single-domain clean Si(111)2x1 surfaces. By considering the data from both reflections, the alkali metal adsorption site positions can be triangulated. The experimental geometry for both reflections is discussed in Chapter 2.

Si 1s XSW data for the (111) Bragg reflection

XSW using surface-sensitive photoabsorption yield previously has been used to determine the substrate reconstruction of a number of surfaces, as well as the position of the substrate surface atoms beneath the adatoms[4-8]. At the photon energy for Si(111) backreflection (1977 eV), the kinetic energy of Si 1s photoelectrons is ~130 eV. The escape depth of electrons at this kinetic energy is quite low at 7.2 ± 1.6 Å, as determined from the kinetic energy of photoemitted Si 1s electrons and the "universal curve" for Si [9]. This corresponds to 2.3 atomic layers of Si, and the majority of electrons which contribute to the Si 1s photoemission peak will originate from these top two layers. By assuming this escape depth and performing an angular integral over the CMA acceptance cone, we find the contribution from the topmost bilayer was $63 \pm 8\%$ across most of our models, with the second bilayer contributing $20 \pm 2\%$ and the bulk Si contributing the remaining $17 \pm 6\%$. Thus the contribution of bulk Si atoms to the total signal must be considered. As mentioned above, atoms in multiple positions along the Bragg reflection will decrease the overall coherent fraction of the data. If the Si(111) surface atoms are in different positions than the Si bulk atoms relative to the bulk (111) diffracting plane position, the Si 1s XSW data will have a coherent fraction which is reduced to bulk coherent fraction of $f_c = 0.707$, due to the interference of bulk and surface contributions with different phases (distances). In addition, as seen from equation (15), an expansion or contraction of the Si atom spacing within the surface bilayer results in a reduction or increase in f_c, respectively. A bulk-terminated surface nominally will have surface atoms in the same positions as bulk Si and should have a coherent fraction near the bulk value. An observed increase in f_c for the Si 1s XSW data as the sample changes from the clean Si(111)2x1 to an alkali-dosed AM/Si(111) interface can point towards a bulk-termination of the Si(111) surface upon alkali adsorption. This is one of main points in the structural analysis of the Na/Si(111)1x1 interface in Chapter 5. In addition, simulated XSW data can be created and fit using Si positions from published models of Si surface reconstructions, and the results can be compared to the measured Si 1s XSW data to determine the correct reconstruction of

the Si surface. This is the technique used in Chapters 5-7 for all of the AM/Si(111) interfaces studied via X-ray standing waves.

References

[1] B. W. Batterman and H. Cole, Rev. Mod. Phys. 36 (1964) 681.

[2] A. Herrera-Gómez, Ph.D. Dissertation. X-Ray Standing Wave Study of the Bi/GaAs and Bi/GaP Interfaces, Stanford: Stanford University (1994) 145-51.

[3] D. P. Woodruff, Prog. Surf. Sci. 57 (1998) 1.

[4] J. C. Woicik, T. Kendelewicz, K. E. Miyano, P. L. Cowan, C. E. Bouldin, B. A. Karlin, P. Pianetta and W. E. Spicer, Phys. Rev. Lett. 68 (1992) 341.

[5] T. Kendelewicz, J. E. Klepeis, J. C. Woicik, S. H. Southworth, C. Mailhiot, M. van Schilfgaarde, M. Methfessel, A. Herrera-Gómez, and K. E. Miyano, Phys. Rev. B 51 (1995) 10774.

[6] T. Kendelewicz, P. Liu, G. E. Brown, Jr. and E. J. Nelson, Surf. Sci. 395 (1998) 229.

[7] J. C. Woicik, T. Kendelewicz, S. A. Yoshikawa, K. E. Miyano, G. S. Herman, P. L. Cowan, P. Pianetta and W. E. Spicer, Phys. Rev. B 53 (1996) 15425.

[8] J. C. Woicik, T. Kendelewicz, A. Herrera-Gómez, A. B. Andrews, B. S. Kim, P. L. Cowan, K. E. Miyano, C. E. Bouldin, B. A. Karlin, G. S. Herman, J. L. Erskine, P. Pianetta, and W. E. Spicer, J. Vac. Sci. Tech. A 11 (1993) 2359.

[9] C. M. Garner, I. Lindau, C. Y. Su, P. Pianetta, and W. E. Spicer, Phys. Rev. B 19 (1979) 3944.

Figure 3.1 (a) Reflectivity R(E) described by equation (4) as a function of photon energy around the (111) backreflection condition for Si. Reflectivity width and shift from the Bragg energy (1977.16 eV) are a result of dynamical diffraction theory. (b) Phase $2\pi\nu(E)$ between the incident and reflected X-ray electric fields as described by equation (4), as a function of photon energy around the (111) backreflection condition for Si. The phase changes by π over the width of the reflectivity.

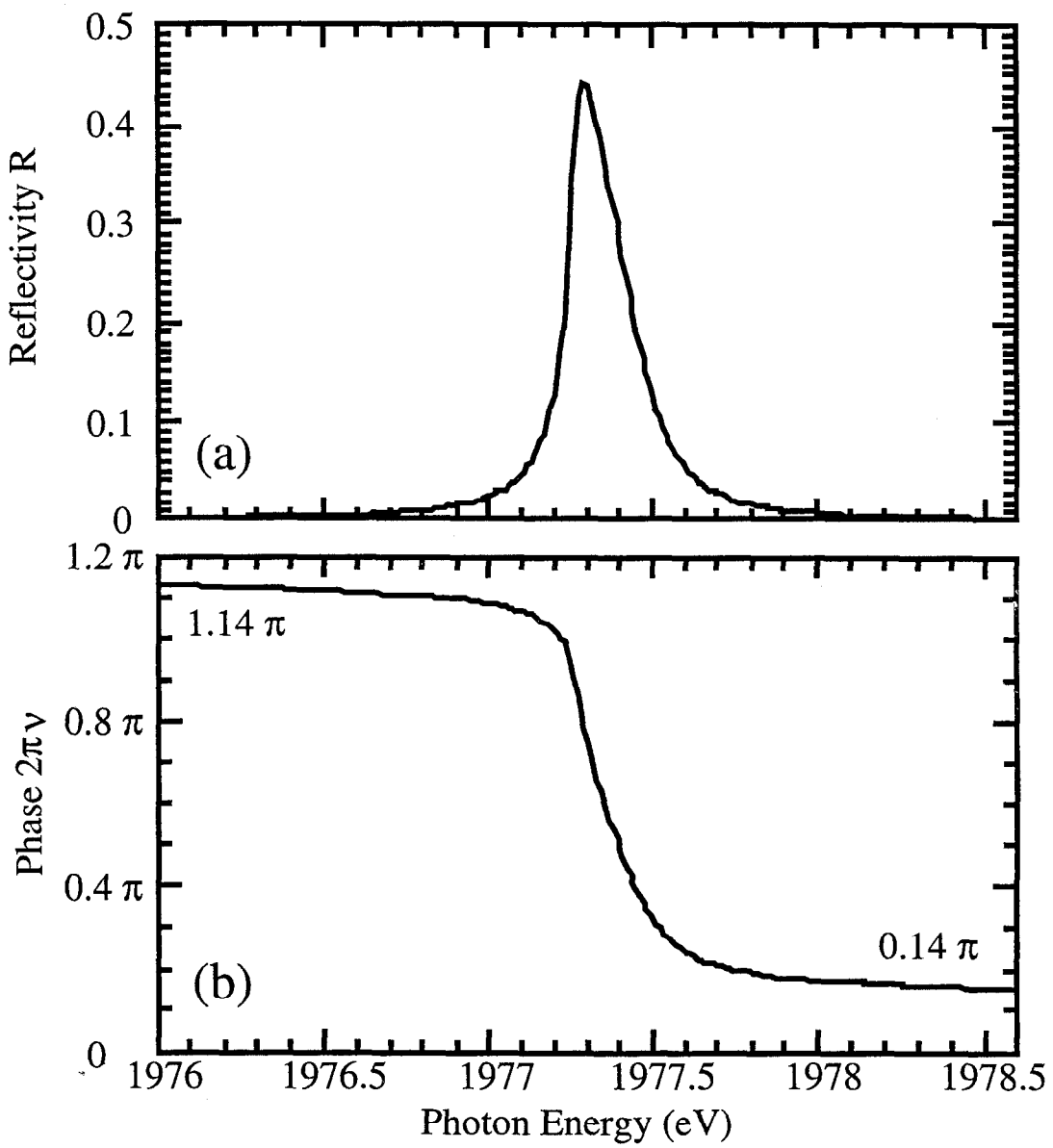

Figure 3.2(a). X-ray standing wave absorption yield lineshapes for a range of values of the coherent distance D_c (in plane spacings) for the (111) backreflection of Si. f_c is fixed at its maximum value of 1. Theoretical lineshape is convoluted with a Gaussian peak of 0.70 eV full width at half-maximum to simulate experimental broadening. Noticeable changes in the lineshape are observed for changes in D_c of 0.1 plane spacings or less.

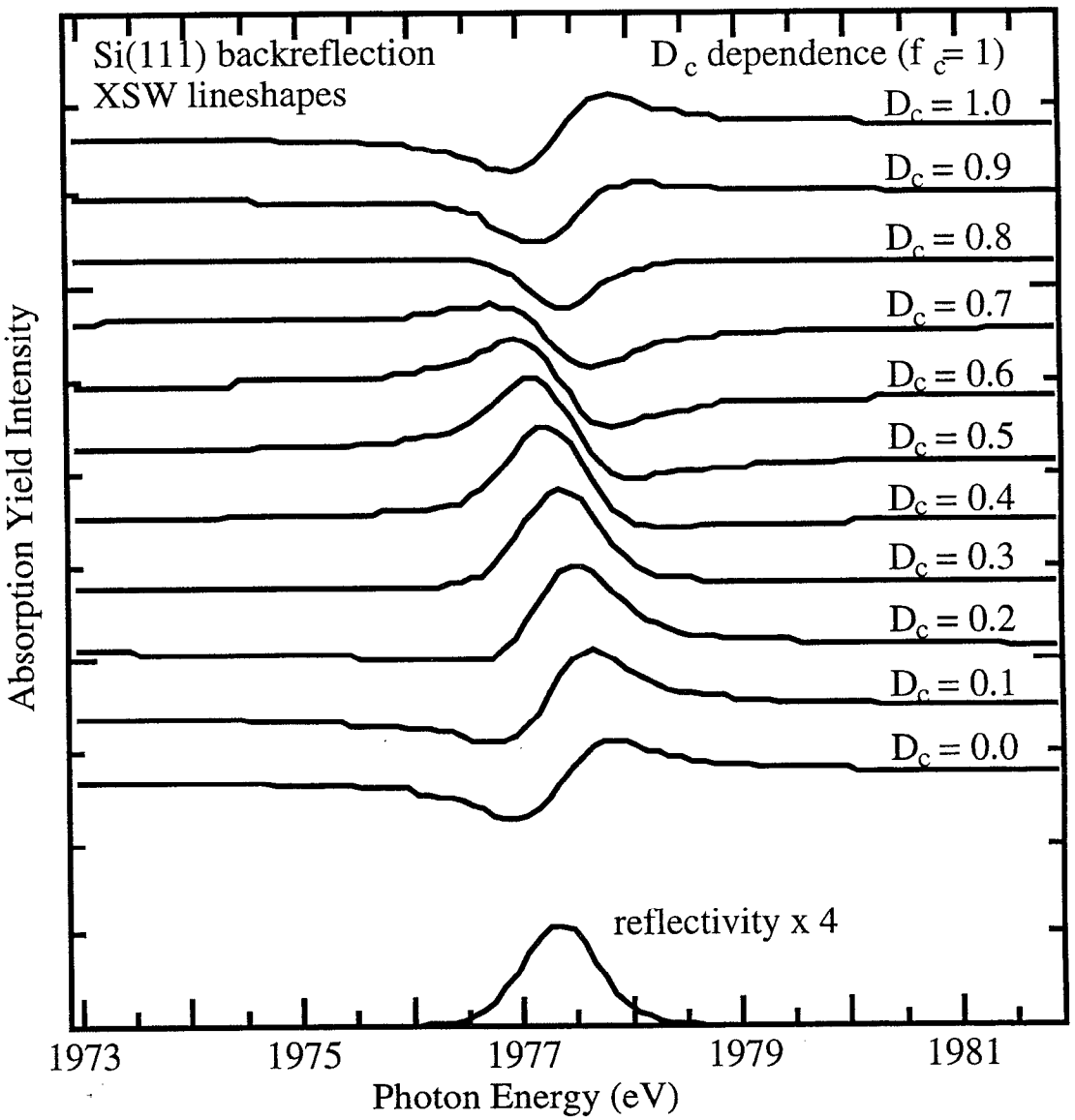

Figure 3.2(b). X-ray standing wave absorption yield lineshapes for a range of values of the coherent fraction f_c for the (111) backreflection of Si. D_c is fixed at 1 (the position of the diffracting plane). Theoretical lineshape is convoluted with a Gaussian peak of 0.70 eV full width at half-maximum to simulate experimental broadening.

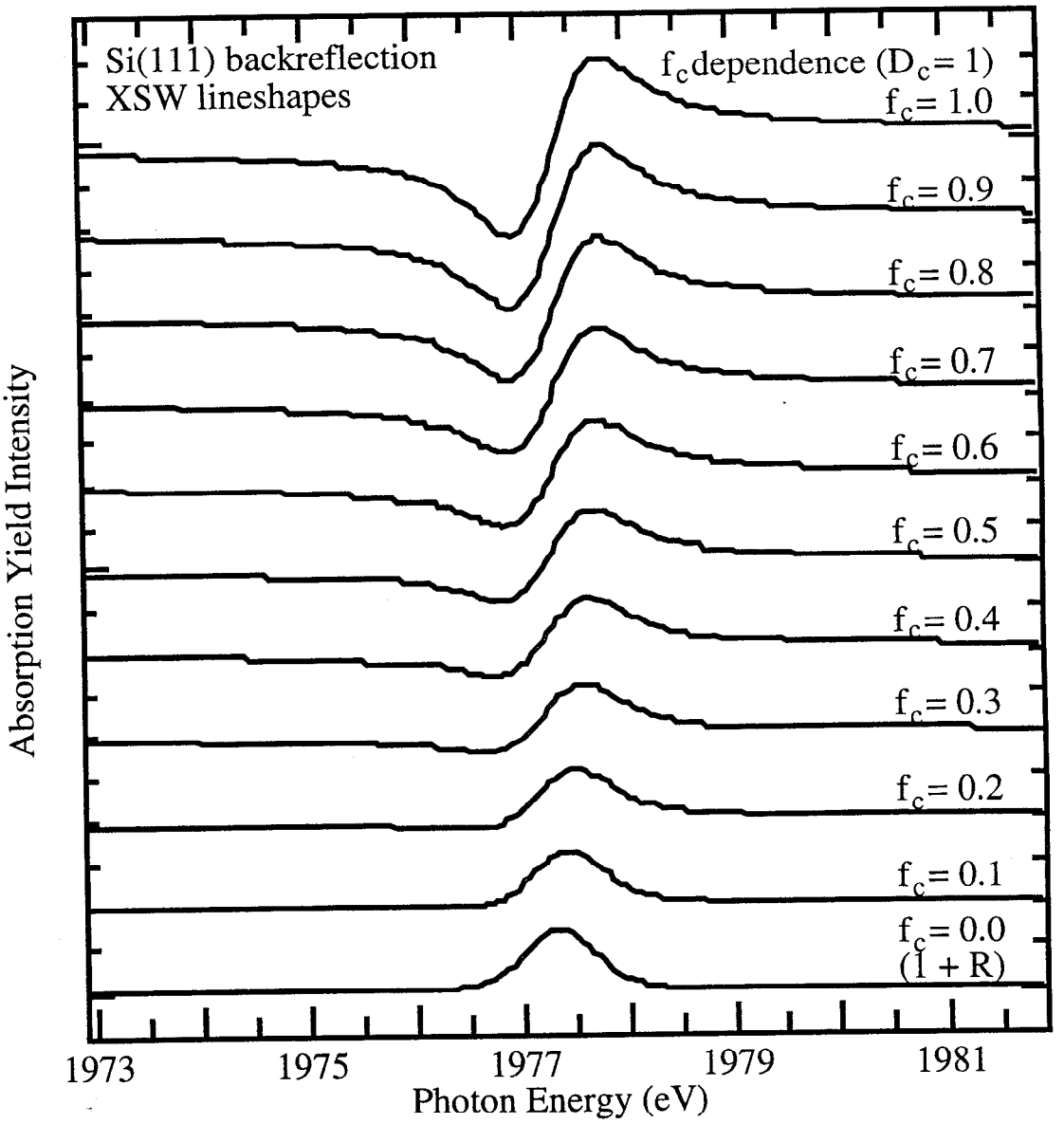

Figure 3.3. $(1\bar{1}0)$ plane projection of the atomic structure of bulk Si. The position of the (111) and $(11\bar{1})$ diffraction planes is indicated. Half of the Si atoms are located 1/8 plane spacing above the diffracting plane, and the other half is 1/8 plane spacing below.

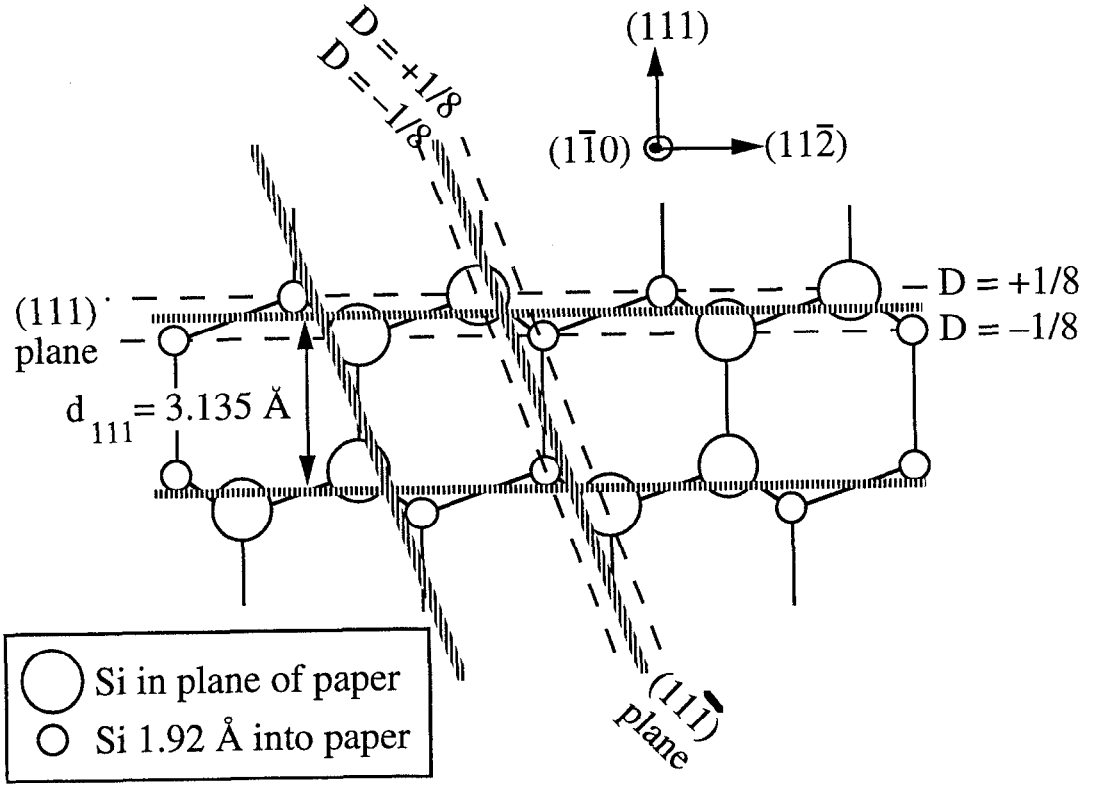

CHAPTER FOUR

COVERAGE-DEPENDENT LEED AND PHOTOEMISSION STUDIES OF ADSORPTION OF NA, K, AND CS ON THE CLEAVED SI(111)2X1 SURFACE

Introduction

In order to determine the surfaces that are most suitable for study using X-Ray Standing Waves (XSW), we initially studied the electronic structure and structural order of alkali metal / Si(111) surfaces via photoemission spectroscopy (PES) and LEED. We have taken photoemission spectra of alkali metal photopeak peaks, the surface-sensitive Si 2p photopeak, and the valence band region as well as work function (secondary electron cutoff) data for many room-temperature dosed Na, K, and Cs coverages on the cleaved Si(111)2x1 surfaces ranging from the clean surface to 100% alkali metal saturation of the surface. In addition, spectra were taken for the annealed cleaved Na/Si(111)3x1 surface and the annealed cleaved and annealed wafer K/Si(111)3x1 surfaces. Some of this data previously have been taken by others. In particular, the annealed wafer Na/Si(111)3x1 and K/Si(111)3x1 surfaces are well-

studied. Work function and angle-resolved inverse photoemission data had been taken on the cleaved Na/Si(111) [1], K/Si(111) [2], and Cs/Si(111) [3] surfaces by Reihl and Magnusson. Tochihara *et al.* took photoemission data on the Cs 5p and valence band of the cleaved Cs/Si(111) surface [4-5]. Our work function data are in agreement with Reihl and Magnusson for all three surfaces, while our photoemission data of the Cs/Si(111) surface match that of Tochihara *et al.* The new contributions of our work include detailed LEED phase diagrams for all three alkali metal / Si(111) surfaces; photoemission data for adsorbate and substrate atoms for Na/Si(111) and K/Si(111) surfaces at many coverages; the discovery that annealed 3x1 phases can be produced on cleaved Si(111)2x1 surfaces under similar conditions as on the Si(111)7x7 wafer surface; X-ray standing wave data on many of these surfaces which provide structural information of adsorbate and substrate atom positions; and conclusions about the structure of these surfaces which are supported by the independent techniques of LEED, photoemission, and X-ray standing waves.

There are few papers discussing the subject of potassium adsorption on the clean cleaved Si(111)2x1 surface. In a recent experimental study of this interface[2], Reihl and Magnusson found that the 2x1 reconstruction of the clean surface is stable against K adsorption, and at the saturation coverage of one monolayer (where the number of adatoms equals the number of Si surface atoms) the surface is metallic. This result agreed with the theoretical calculation of the surface by Ciraci and Batra[6] which predicted that at 1 ML coverage on the K/Si(111)2x1 surface, the substrate is metallized. However, Reihl and Magnusson's results contradicted Batra and Ciraci's second calculation[7], which found the ideal-bulk-terminated substrate (1x1 reconstruction) with 1 ML K adsorbed to be 0.3 eV more stable than the π-bonded Si(111)2x1 with 1 ML K adsorbed. A later calculation by Ye Ling and Fu Huaxiang[8] examined the adsorption site of K adatoms on the bulk-terminated Si(111)1x1 surface at low coverage, and found the threefold hollow (H_3) and fourfold top (T_4) sites to have almost equal chemisorption energies, while the on top (T_1) site was energetically unfavorable.

In contrast to Reihl and Magnusson's paper, we observe six surface phases for room temperature dosing of K on the cleaved Si(111) surface, including a room-temperature-dosed one-domain K/Si(111)3x1 phase. To our knowledge, this is the first observation of the 3x1 phase on a nonannealed AM/semiconductor surface. The K/Si(111) surface shows a 1x1 LEED pattern at 1 ML saturation coverage. In addition, we observe a 3-domain 3x1 pattern on the cleaved K/Si(111) surface upon annealing. We will provide photographs of the new phases observed with LEED. We also will set

limits on the K coverage required for these phases using results from photoemission and secondary electron cutoff measurements. Tentative models for these surfaces will be proposed. These results indicate that the Si(111) cleaved surface is more interesting than previously perceived.

An explanation of the LEED surface phase diagrams

In each of the phase diagrams Figure 4.1(a)-(c), the points represent observed coverages at which the corresponding LEED pattern was seen. The horizontal bars indicate outer limits on the coverage for the surface phases as determined from multiple dosing runs. These bars are drawn at points halfway between consecutive doses, and the dosing run chosen for the limit is the one for which the width of the coverage range is maximized. The phase diagrams indicate overlapping coverage limits for several phases; this overlap is seen in the observed coverage data points as well as with the estimated coverage limits. A description of the LEED pattern for each surface phase is given to the side of the corresponding horizontal bar.

The dosing limits given above are approximate, as later runs which tried to achieve a particular LEED pattern in a quick one or two doses required shorter dosing times than those for the dosing progressions above. The difference in these times is more than can be accounted for by possible errors in the estimate of the idle time subtracted from the actual time of each dose. The cleanliness of the surface may have an effect on the required dose, as the surfaces undergoing quick dosings certainly were cleaner than the surfaces later in the dosing progressions. That the quick dosing method produced cleaner surfaces was seen from the lack of a characteristic oxygen peak in VB photoemission spectra, and also by the lower work functions of surfaces prepared in this way. Figure 2 shows the work function difference data as a function of potassium monolayer fraction, which is calculated from the ratio of the measured K 3p photoemission peak intensity divided by the peak intensity for the saturation coverage surface. We observed that surfaces prepared through quick dosings have larger work function differences (by 0.3-0.8 eV) than surfaces at the same monolayer fraction produced in a dosing progression. That contamination reduces the work function difference has been demonstrated before[2,9].

K/Si(111)

Work Function and Photoemission Results (for Coverage Determination)

Figure 4.2 summarizes the results of our two experimental room temperature (RT) dosing runs on Beam Line 8-1. Figure 4.2 plots work function difference versus alkali metal coverage, represented by percentage of K 3p photopeak area saturation. The figure also indicates the observed LEED patterns during the dosing runs in order to provide work function difference values for the various phases. The corresponding plots for Cs and Na adsorption on the cleaved Si(111) surface are given in Figures 4.14 and 4.22, respectively. For all three alkali metals, the work function difference $\Delta\Phi$ decreases linearly with percentage photopeak area saturation until it reaches a minimum. This linear decrease is consistent with a linear increase in the number of surface dipoles as more alkali adatoms attach to the surface. Also, photopeak area scales linearly with evaporation time up to saturation, with no increase in area for dosing times after saturation coverage is reached. Thus, these plots of work function difference versus alkali photopeak area saturation can be compared to plots of work function difference versus dosing time in the literature.[1-3] The work function difference is determined by measuring the change in the energy of the secondary electron cutoff relative to the clean surface. The two experimental runs show a slight minimum in the WF between 83% and 100% of K 3p photopeak area saturation. The values of the WF minima were $\Delta F_{min} = -3.56 \pm 0.30$ eV and -3.20 ± 0.30 eV for the two runs. The averaged result of -3.38 ± 0.20 eV agrees well with the previous result of Reihl and Magnusson[2] of $\Delta F_{min} = -3.45$ eV for room temperature K dosing on the Si(111)2x1 surface, as well as the result of $\Delta F_{min} = -3.2$ eV for RT dosing of potassium on the Si(111)7x7 surface[9,10]. One of the runs (squares) has smaller work function difference values throughout when compared to the other; this may be due to oxidation of the surface from an insufficiently outgassed LEED filament. Valence band photoemission spectra indicated significant oxidation throughout the run. This oxidation may transfer some charge away from the semiconductor and towards oxygen atoms atop the alkali adatoms, thus reducing the dipole strength. Looking at the area under the K 3p photopeak, the amount of potassium on the surface saturates at the WF minimum for the first experimental run. The second experimental run is missing a final dose to show the saturation of the K 3p peak area, but the shape of the photopeak for the last dose of this run was found to be identical to that of the peaks for the saturation doses of the first run, both by visual inspection and by comparison of the relative weights of the components of a fit to the photopeak (which required two components plus a plasmon loss peak). From both types of measurements and both experimental runs, we estimate the dosing time for a saturation coverage of 1 monolayer (ML) of potassium to be

226±15 sec. Here 1 ML is defined as the coverage at which the number of K adatoms equals the number of Si surface atoms on the surface (7.83×10^{14} atoms/cm^2) and this coverage corresponds to a minimum in the WF.

LEED study – Room temperature cleaved K/Si(111) phase diagram

While taking WF and PES data of different potassium doses on the cleavable Si(111)2x1 surface, we observed an interesting new phase, which is described below. In addition, we had previously seen and taken PES and X-Ray Standing Wave (XSW) data on the K/Si(111)1x1 surface seen at saturation coverage. The fact that the existence of the 1x1 surface at saturation coverage differs from previously published experimental results[1] motivated us to study the adsorption of potassium on the cleavable Si(111) surface in more detail. As described in the Experimental section, two dosing progressions were performed concentrating on the use of LEED as a diagnostic tool of the periodicity of potassium-induced surface reconstructions and of the quality of the surface. The results presented by the photographs in Figure 4.3 are taken from the same dosing progression. The second run yielded the same patterns as the first.

A total of *seven* distinct surface phases were observed at different potassium coverages for room temperature dosing on the cleavable Si(111) surface, which initially showed a clean, single-domain 2x1 LEED pattern. As described above, Figure 4.1(a) shows the dependence of the observed K/Si(111) LEED phases upon K coverage. In the description below, the symbol F_K represents the coverage range in terms of the fraction of K 3p photopeak area saturation. As seen in Figure 4.1(a), the LEED results for this third set of data are consistent with those from the previous samples, indicating our estimate of the saturation dosing time is reasonable, as well as a linear increase of photopeak area with dosing time before saturation.Two of the three samples in Figure 4.1(a) were only measured with LEED and not photoemission. For these two samples, the coverage F_K is represented as the ratio of the effective dosing time to the estimated dosing time required for saturation coverage, 226±15 sec, as determined from the work function minimum. For each dose, an idle time of 35 sec was subtracted from the total time the evaporator was heated to determine the effective dosing time, as there was no increase in chamber pressure until after this idle time. The value of $F_K = 1.10$ for one of the data points corresponds to a dosing time greater than that required for saturation, and we expect the K 3p photopeak area would have corresponded to $F_K = 1.00$ if it had been measured.

The various phases of the room temperature dosing progression are as follows:

1. For $F_K \leq 0.16$, the LEED remains 2x1 single-domain. See Figure 4.3(a).
2. For $0.14 \leq F_K \leq 0.40$ pairs of spots appear and straddle the 4th order positions halfway between the 2x1 spots. No photograph was digitized for this K/Si(111) phase, but the corresponding Cs/Si(111) pattern is identical and appears in Figure 4.15(b). This pattern is identical to that seen for Cs adsorption on Si(111) for coverages of $0.08 \leq F_{Cs} \leq 0.40$. A line from a 2x1 spot to a paired spot makes an angle of ~20° with the horizontal $[11\bar{2}]$ axis, i.e. the axis along which the 2x1 spots appear and which is perpendicular to the π-bonded chains in the Si(111) surface plane. In addition, the spacing is consistent with being $\sqrt{7}$ times the bulk lattice spacing. For this reason, we name this pattern "2x1 + $\sqrt{7}$x$\sqrt{7}$–R19°?". The question mark indicates that the pattern does not correspond to the typical $\sqrt{7}$x$\sqrt{7}$–R19° pattern, which does not have mirror symmetry about the horizontal axis as this LEED pattern does. The observed mirror symmetry may indicate two domains of $\sqrt{7}$x$\sqrt{7}$–R19° periodicity on the surface.
3. For $0.12 \leq F_K \leq 0.46$, LEED shows a pair of spots on either side of the horizontal $[11\bar{2}]$ axis, as seen in Figure 4.3(b). If a line is drawn between 2 second-nearest neighbor 1x1 LEED spots, the spot is 1/6 of this distance, corresponding to a $2\sqrt{3}$x$2\sqrt{3}$–R30° pattern. However, only the spots nearest the 1x1 spots appear, and the third domain, which would have spots along the vertical $[\bar{1}10]$ direction, is absent. In addition, the 2x1 spots are still strong. This pattern has been seen once before, by Gobeli et al.[11] in their study of RT dosing of Cs on the cleaved Si(111) surface. We shall call this pattern "2x1 + $2\sqrt{3}$x$2\sqrt{3}$–R30°." We also observe this pattern for Cs dosing on the Si(111) surface, at a Cs coverage of $0.21 \leq F_{Cs} \leq 0.57$.
4. For $0.31 \leq F_K \leq 0.60$, the 2x1 spots split in two and migrate towards the 3x1 positions with increasing coverage. Different spacings of these spots have been seen, from very close together (almost 2x1) to almost 3x1. A later run using small dosing increments around this coverage range verified that the LEED spots do migrate smoothly from 2x1 to 3x1 positions as the K coverage is increased. It appears that a LEED pattern corresponding to any given point in the migration can be achieved with the appropriate K dosage. In the photo (Figure 4.3(c)) one can see a weaker spot to the right of these pairs. This particular spot has been seen often and appears to be part of an interference pattern between the 2x1 and 3x1 LEED patterns.

5. For $0.43 \leq F_K \leq 0.76$, a simple *one-domain* 3x1 pattern is observed, as seen in Figure 4.3(d). To our knowledge this is the first observation of the 3x1 phase on a nonannealed AM/semiconductor surface, and the first observation of a *single-domain* 3x1 phase on any AM/semiconductor surface. 3x1 patterns seen from annealing are always 3-domain. This pattern was also achieved at a total dosing time corresponding to a coverage of $\Theta = 0.38$ ML. In this instance only two short doses were made on the surface to go right to this coverage, instead of the five doses used in the progression.
6. In a small coverage range, $0.58 \leq F_K \leq 0.76$, we have seen a strange-looking pattern, as seen in Figure 4.3(e). There are spots along the lines 30° off either side of the horizontal $[11\bar{2}]$ axis. The spacing of the spots is 1/4 the distance between second-nearest neighbor 1x1 spots, and all of the spots are visible, except for the third domain, which would have spots along the vertical $[\bar{1}10]$ direction. The result is the zigzag pattern seen in the photograph. In addition, 3x1 spots are still seen in the pattern along the $[11\bar{2}]$ direction, but they are considerably weaker than the other spots and are probably from a different section of the sample. The 3x1 spots were absent from the pattern on other samples with the zigzag pattern. We identify this pattern as a two-domain $\sqrt{3}$x2 superstructure, and explain our model of this surface in the Discussion. The photograph was taken from a different surface from the two LEED runs but the RT dosing preparation was done in only two doses and corresponds to $F_K = 0.42$ ML. This pattern also was seen in one of the LEED dosing progression runs in the small coverage range above. This pattern was also observed on the Cs/Si(111) surface at Cs coverages of $0.77 \leq F_{Cs} \leq 0.94$.
7. For $0.70 \leq F_K \leq 1.00$, the pattern reverts to a 1x1 pattern (Figure 4.3(f)). This is the pattern at saturation coverage ($F_K = 1.00$).

Annealed K/Si(111)3x1 surface phase

In addition to the room temperature dosings above, the cleaved Si(111)2x1 surface produced a 3-domain 3x1 LEED pattern (Figure 4.4) via two different K dosing procedures involving sample heating. In the first case, the sample was first dosed with K at RT to about 1 ML coverage (a 1x1 pattern was observed at RT). The sample was then heated above 600 K for 8-10 min. The 3x1 pattern appeared as the sample started to cool and remained at RT. The surface dosed at RT to 0.42 ML to give a two-domain $\sqrt{3}$x2 surface also produces a 3x1 3-domain pattern upon annealing. The 3-domain 3x1 pattern could also be achieved by dosing for ~8 min (in two 4 min segments) on a

surface heated to 600 K. To our knowledge the 3x1 pattern has not been achieved previously for K dosing annealing on a *cleavable* Si(111) surface. It is not surprising that the 3x1 phase was seen, however, since the Si(111)7x7 wafer surface changes to a 3x1 phase upon dosing while the surface is heated.

The work function differences for the various surfaces are given in Table 4.1. Values from preparation via the cleaner, quick dosing method are listed when possible.

After observing the numerous phases of K on the cleaved Si(111) surface, we studied the stability of these surfaces with respect to contamination, in order to see if any of the surfaces could be studied with techniques which would take longer to collect data than PES and LEED. We dosed the surfaces in one or two quick shots to get to the LEED pattern in question, and then let the surface sit in the UHV environment. The surface was checked with LEED periodically, and the "lifetime" of the surface is defined as the time it took for the LEED pattern to revert to a 1x1 pattern due to contamination. The lifetimes of the various surfaces and the chamber pressures are given in Table 4.2.

For the annealed K/Si(111)3x1 3-domain surface, we did not see the surface change to a 1x1 pattern even after 14 hrs. The room-temperature one-domain 3x1 pattern also was maintained for 7 hrs, considerably longer than the other three phases listed. It appears that the annealed K/Si(111)3x1 surface is passivated against oxygen adsorption. Passivation to oxygen also has been observed by Tikhov for the annealed Na/Si(111)3x1 surface[13], which suggests passivation of the AM/Si(111)3x1 is connected to the substrate reconstruction and not the specific AM adsorbed.

Discussion of LEED results

These results contrast with the results of Reihl and Magnusson[2], who contend that the Si(111)2x1 reconstruction is stable upon K adsorption, even at saturation coverage (1 ML). From our data, the 2x1 pattern is stable only up to about 0.16 ML of K coverage. And the saturation coverage shows a 1x1 pattern. We do not understand how the LEED patterns of Reihl and Magnusson could have been observed, as their WF data appear similar to ours and their pressures are similar to ours. We have found six surface phases produced by RT potassium adsorption on the Si(111) cleaved surface, and have observed a 3x1 3-domain pattern on the annealed K-dosed cleaved surface. In the following paragraphs we discuss each of the surface phases of interest. We emphasize that all models proposed below are tentative, and rely solely on the periodicity and symmetry of the LEED pattern and the measured K adatom coverage.

Quantitative structure measurements are needed to verify or refute our proposed surface atomic geometries. In Chapter 7 we study the annealed and nonannealed K/Si(111)3x1 surfaces using back-reflection X-Ray Standing Waves (XSW).

1. The 2x1 + $\sqrt{7}$x$\sqrt{7}$–R19° phase was not reported in our published article about the K/Si(111) LEED patterns[12]. After observing similar phases for Cs dosing on cleaved Si(111) (see below), we reviewed our photographs of the K dosing runs and realized that an additional 2x1 + $\sqrt{7}$x$\sqrt{7}$–R19° phase was seen for $0.14 \leq F_K \leq 0.40$. The similarity of the 2x1 + $\sqrt{7}$x$\sqrt{7}$–R19° and 2x1 + $2\sqrt{3}$x$2\sqrt{3}$–R30° phases led us to mislabel the 2x1 + $\sqrt{7}$x$\sqrt{7}$–R19° phase upon first inspection. As the K coverage is quite low for this phase and the pattern still has a strong 2x1 character, we expect this phase represents K adsorbing on top of the 2x1 π-bonded chain, with a model similar to that for the 2x1 + $2\sqrt{3}$x$2\sqrt{3}$–R30° phase discussed in the next paragraph, but with different spatial periodicity.

2. The 2x1 + $2\sqrt{3}$x$2\sqrt{3}$–R30° surface retains the 2x1 π-bonded chain of the clean surface, with the K adsorbing on sites between the chains in a $2\sqrt{3}$x$2\sqrt{3}$–R30° geometry. A tentative model of the surface atom structure is given in the left half of Figure 4.5. This figure corresponds to 1/3 ML with clusters of four K adatoms in a $2\sqrt{3}$x$2\sqrt{3}$–R30° geometry. Lower coverages with this LEED pattern could correspond to fewer K adatoms in each cluster, or to a mix of clean and K-adsorbed regions, with the clean regions reinforcing the 2x1 part of the pattern. Although from a classical viewpoint the surface dipoles caused by each K adatom adsorbed would repel one another and prevent clustering, substrate surface restructuring upon adsorption of the adatom could make adsorption sites near the first adsorption site energetically favorable. Since the spots for the third domain of the $2\sqrt{3}$x$2\sqrt{3}$–R30° aspect of the pattern are absent, the LEED pattern shows a preferred direction across the chains, and we would expect the Si chains to remain in the K-adsorbed regions. That the 2x1 + $2\sqrt{3}$x$2\sqrt{3}$–R30° surface includes substrate reconstruction is supported by the fact that this reconstruction also has been seen for low coverages (Θ = 0.23–0.27 ML) of Cs on the cleaved surfaces[11]. This reconstruction is not seen for Na, which is a smaller atom than both K and Cs. So it appears to be easier for the larger K and Cs atoms to just "decorate" the 2x1 surface at lower coverages as their size restricts their motion deeper into the surface.

3. The mixed 3x1 + 2x1 pattern appears to be an interference of the LEED patterns from the 2x1 and 3x1 patterns which occur at lower and higher coverages, respectively. This pattern does *not* correspond to a surface with different relative

populations of regions with 2x1 or 3x1 periodicity, as the LEED pattern from such a surface would not appear as an interference of the 2x1 and 3x1 patterns, but rather as a sum of the 2x1 and 3x1 patterns, with the relative intensity of the contributing patterns proportional to the regions' relative populations. As Figure 4.3(c) depicts, there are no spots in the positions for the 2x1 and 3x1 patterns. Also, it appears that a LEED pattern corresponding to any given point in the migration of the spots from 2x1 to 3x1 positions can be achieved with the appropriate K dosage. This suggests a gradual restructuring process in which the adsorbate and substrate change the periodicity of the surface as K adsorbate coverage increases. The ability to "freeze" this process in time by controlling the K dose provides a unique opportunity to study the kinetics of adsorption and reconstruction on an AM/semiconductor interface.

4. The one-domain 3x1 pattern has not been seen before, because heating of the surface destroys the direction preference of the surface, and all 3 domains become possible. This is seen in our annealed cleaved surfaces, which produce 3-domain 3x1 surfaces. The direction of the 3x1 LEED pattern is the same as that of the 2x1 surface at lower coverages, suggesting a 3x1 substrate reconstruction in a direction determined by the clean surface reconstruction. The fact that the RT-dosed one-domain 3x1 LEED pattern is seen over a range of coverages ($0.43 \leq F_K \leq 0.76$) suggests that the 3x1 periodicity is determined by the substrate and not the adsorbate atomic structure.

Current models for the K/Si(111)3x1 surface conflict with the observed room-temperature-dosed 3x1 surface. These models involve Si π-bonded chains with a 3x1 periodicity, either as a Seiwatz chain with a missing row of Si[14,15], or an extension of the alternating sevenfold and fivefold rings of Pandey's 2x1 structure[16] by adding a sixfold (bulk-like) ring to the sequence[17]. Both models introduce the site of K adsorption as a single dangling bond on top of a more bulk-like structure, with the site in the valley created by the missing Si row for the former model, and on top of the sixfold ring for the latter. The simplicity of an extension of the bulk surface to accept the K adatoms appears to conflict with the complex restructuring process of the mixed 2x1 + 3x1 phase directly proceeding the 3x1 surface. Both models also prefer a 1/3 ML coverage, while we have seen a range of coverages above 1/3 ML ($0.43 \leq F_K \leq 0.76$) for the RT-dosed one-domain 3x1 surface. Lastly, the 3x1 reconstruction was produced at room temperature, so there is not enough thermal energy to remove the Si atoms to create the missing rows in the missing row and Seiwatz chain model.

We emphasize that this does not disallow the missing row and Seiwatz chain as a model for the *annealed* K/Si(111)3x1 3-domain surfaces on the wafer and cleaved surfaces. In fact, several experimental facts indicate that the RT-dosed one-domain

K/Si(111)3x1 surface and the annealed 3-domain K/Si(111)3x1 surface *may* be different reconstructions. First, there is a large difference in the work function difference for the RT-dosed 3x1($\Delta\Phi = -3.21$ eV) and annealed 3x1($\Delta\Phi = -1.62$ eV) surfaces. Second, the RT-dosed 3x1 surface exists over the range of coverages $0.43 \leq F_K \leq 0.76$ while the annealed 3x1 surface has been determined to exist at coverages no greater than 1/3 ML[18]. Lastly, the annealed 3x1 surface is considerably better passivated against contamination than the RT-dosed 3x1 surface. However, all three of these differences could be attributed to the adsorption of additional K adatoms in less energetically favorable sites on the RT-dosed 3x1 surface, which otherwise might be similar to the annealed surface. These additional adatoms would increase the coverage to a range above 1/3 ML, would contribute to the lowering of the work function and would provide sites for oxygen adsorption and lead to reduced surface passivation for the room-temperature surface. Upon annealing these additional adatoms would be removed, lowering the coverage to the preferred 1/3 ML.

5. The fact that there are only two domains of $\sqrt{3}$x2 and not one along the $[\bar{1}10]$ direction implies that the chain still exists as the LEED pattern still has a preferred direction which is the same as that of the clean 2x1 and one-domain 3x1 patterns. This suggests that a reconstructed Si structure still exists at this coverage, and the second-order periodicity along one of the axes suggests a chain every second row of atoms. We propose the model in the right half of Figure 4.5. In this model, K adsorbs in an ordered fashion among the chains. The ordering of the vacancies of K adatoms and the underlying 2x1 chain determine the $\sqrt{3}$x2 periodicity. To produce the LEED pattern in Figure 4.3(e), two domains are required, and the second domain corresponds to the mirror reflection of Figure 4.5 across the axis of the chain, i.e. the $[\bar{1}10]$ axis. The diagram corresponds to a coverage of 3/4 ML, but one adatom can be removed from inside the given unit to produce a coverage of 1/2 ML and retain the $\sqrt{3}$x2 periodicity. This model can then explain the lower coverage of $F_K = 0.42$ for this surface, as could inhomogeneity of coverage on the cleaved Si(111) surface.

6. The 1x1 phase at higher coverage could indicate a reversion to the bulk-terminated surface with K adsorbing on the symmetry sites. Alternatively, the remaining K adatoms adsorb on the vacancies in the $\sqrt{3}$x2 model above, and the higher K adatoms determine a 1x1 pattern. Whether the 1x1 LEED pattern from the adatoms is reinforced by a bulk-terminated surface or the Si chain remains below the K monolayer cannot be determined from this data.

In contrast to Reihl and Magnusson's phase diagram of the 2x1 reconstruction surviving room-temperature potassium adsorption, we present a complex RT phase diagram (Figure 4.1(b)) involving four phases apart from 2x1, and a region of gradual structural transformation between the 2x1 and 3x1 phases. Included in the observed LEED patterns are the unusual 2x1 + $2\sqrt{3}$x$2\sqrt{3}$–R30° and two-domain $\sqrt{3}$x2 patterns, as well as a previously unobserved single-domain 3x1 phase, and a 1x1 surface at the saturation coverage of 1 ML. All RT-dosed surface phases except 1x1 show a direction preference along the direction of the chains on the clean 2x1 surface, which suggests that these phases include a surface reconstruction in a direction determined by the clean 2x1 surface reconstruction. In addition, it was confirmed that a 3x1 3-domain surface could be achieved on the annealed cleaved K/Si(111) surface, as it has been on annealed K-dosed Si(111) wafers. We measured work function difference data to provide coverage ranges for the various phases and to guide further experiments in reproducing these surfaces, and found that reducing the number of doses used to get to a given phase reduces contamination and the required K coverage for that phase. We also determined that the annealed 3-domain K/Si(111)3x1 surface is passivated against oxygen adsorption, and the RT-dosed single-domain 3x1 surface resists oxygen adsorption more effectively than the other RT-dosed phases. Since the Na/Si(111)3x1 surface also is passivated[13], it is the nature of the 3x1 substrate reconstruction which causes passivation after AM adsorption.

Tentative models for the previously undiscussed 2x1 + $2\sqrt{3}$x$2\sqrt{3}$–R30° and two-domain $\sqrt{3}$x2 patterns were presented as a starting point for discussion and require experimental confirmation. Current models of the K/Si(111)3x1 surface[14,15,17] were found to conflict with the observed RT-dosed surface.

The complexity of the phase diagram seen for RT potassium dosing on the cleavable Si(111) surface suggests further experimental study of this interface is needed. A number of experimental opportunities are provided by the RT-dosed cleavable K/Si(111) surface. The existence of a single-domain 3x1 phase would aid angle-resolved photoemission studies trying to determine the existence of chains on the 3x1 surface, as they would not be hampered by the deconvolving of data from the three domains of the annealed 3x1 surface. The gradual restructuring process of the mixed 2x1 + 3x1 phase, controllable by the amount of K dosed, could provide information on the kinetics of the adsorption and reconstruction process on an AM/semiconductor interface. The 2x1 + $2\sqrt{3}$x$2\sqrt{3}$–R30° and two-domain $\sqrt{3}$x2 phases also encourage further study, although the problem of their short contamination "lifetime" would have to be overcome.

Photoemission results and discussion - Room temperature cleaved K/Si(111) surfaces

In an experiment on Beam Line 8-1 at SSRL, four room temperature potassium dosing runs of the cleaved Si(111) interface were performed. LEED and photoemission were used to characterize the surface after each K dosing. Figure 4.1(a) of the LEED results section is the observed phase diagram as a function of K coverage. The features of the diagram are a 2x1 phase at low coverages, a 1x1 phase at saturation coverage, and five intermediate phases including a single-domain 3x1 structure. As we describe below, the differences in the shapes of the photoemission spectra for each of these phases are small, unlike the three distinct lineshapes corresponding to the LEED phases for Na dosing. In addition, the LEED phases as well as the photoemission spectra for K/Si(111) are similar to those for room temperature cesium dosing (phase diagram in Figure 4.1(b)), with the exception of the $\sqrt{3}x\sqrt{3}$–R30° phase replacing the single-domain 3x1 in the sequence of Cs/Si(111) phases. From LEED results, the photoemission results below and from XSW data we will conclude that K or Cs adsorb on top of a Si chain structure up to saturation dosage in similar overlayer arrangements and do not revert the Si surface back to bulk-terminated, unlike the case of Na adsorption. For K/Si(111) photoemission, the spectra taken at each dose include the K 3p photopeak at photon energy 65 eV, the Si 2p peak at photon energy 145 eV, and the valence band region at photon energy 65 eV. The photon energies for Si 2p and the valence band are the same as for the Na dosing runs, and were chosen to maximize surface sensitivity.

The progression of the K 3p photopeak with increasing K coverage is given in Figure 4.6. The area of the peak increased linearly with dosing time until saturation, and some of the runs in the phase diagram of Figure 4.1(a) measure K coverage directly from the dosing time using this linearity, as K 3p area data were not taken for those runs. The width of the peak does not change with coverage, suggesting only one component of the peak at all potassium coverages. At higher coverages, the peak becomes skewed as it takes the lineshape explained by Doniac and Sunjic [19] as characteristic of a singularity of losses present in metals. Beyond the apparent energy shift in the maximum of the peak at high coverage due to the skewing of the lineshape, the K 3p peak position does not move as K coverage increases. This suggests the K-Si bond energy is similar at all coverages and perhaps the positions of the Si atoms do not change throughout K dosing, so that the Si chains of the clean 2x1 surface remain under the potassium overlayer reconstructions.

While the similarity of the K 3p spectrum at all coverages indirectly suggests no change in the arrangement of the Si substrate, the Si 2p provides a direct test of this argument. Figure 4.7 displays the surface-sensitive Si 2p spectra at photon energy 145 eV for the K/Si(111) interface with increasing K coverage. These spectra change only slightly in lineshape from the clean Si(111)2x1 lineshape throughout the dosing progression. The number of components required to fit the spectra remains four throughout, and the changes in the "cleavage" between the two parts of the lineshape are explained as changes in the binding energy difference between the main surface component and the bulk component, similar to the changes for low-coverage spectra for Na/Si(111) in Figures 4.25(b) and 4.25(c). As four components are required for the fit to the Si 2p peak of the clean Si(111)2x1 surface and no drastic changes in the Si 2p spectrum occur as K is dosed on the surface, the underlying π-bonded Si chain structure of the clean surface remains intact up to saturation potassium coverage.

Unfortunately, the K dosing run measured here had considerable oxide contamination for the later doses, as seen in the valence band spectra, presented in overlaid and stacked forms in Figures 4.8(a) and 4.8(b). However, the oxide contamination peak does not affect the shape of the valence band spectra. The effect of oxidation is seen in Figure 4.9. The three spectra with similarly sized surface states at the top of the valence band are from a later dosing progression. After the first three doses no oxide peak is seen, but waiting 70 min and exposure to the LEED beam produces a bulge in the valence band around 54.6 eV kinetic energy due to the oxide. The rest of the valence band is unchanged, suggesting that oxidation's effect on the surface reconstruction is small.

The region of the spectra around the surface state at the valence band maximum does not change considerably for the K/Si(111) interface as potassium coverage increases, as seen in Figure 4.8. The changes in the valence band spectrum for Na/Si(111) (Figure 4.26) are much more dramatic, with the formation of a large peak attributed to Na-Si bonding and a bulk-terminated Si(111) surface for the 1x1 phase. The first K dose produces an increase in density near the top of the valence band, and in particular the dip seen 0.4 eV below the surface state peak fills up, and the binding energy of the peak at the valence band maximum increases by 0.2 eV. This behavior indicates some interaction between potassium adatoms and the π-bonded Si chains, which remain at low K coverage. The interaction is also seen in Figure 4.7, as the Si 2p shape changes indicating a chemical shift of the surface Si atoms photopeaks. The low coverage Na- and Cs-dosed Si(111) surfaces behave similarly (see Figures 20 and 26). For higher K coverages before the 1x1 phase, the bulk and surface states decrease

in size due to overlayer coverage, but the shape and position of the surface peak at the valence band maximum is unchanged. The similarity of the valence bands for the clean Si(111)2x1 and saturation coverage K/Si(111)1x1 surfaces is shown in Figure 4.10. For all three samples the surface peak shifts to 0.4 eV higher binding energy , while the signal from the bulk peaks decreases in size due to the potassium overlayer. Note that the lowest pair of spectra in Figure 4.10 show no oxide peak while the other two samples have different levels of oxidation, yet the behavior of the valence band upon K dosing is the same. The similarity of the clean 2x1 and K-dosed 1x1 valence band spectra and the absence of any dramatic changes in lineshape through the K dosing run (beyond the first dose) suggest the surface state of the π-bonded Si chains remains throughout K dosing and at saturation coverage. LEED also supports the stability of the Si chains to K adsorption, as the patterns retain the directionality of the clean surface 2x1 pattern throughout the K/Si(111) phase diagram of Figure 4.1(a) of the LEED section, as seen in the LEED photographs of Figure 4.3.

Previous experimental and theoretical work support the idea of the Si π-bonded chains' stability to K adsorption. In their study of K adsorption on the cleaved Si(111) surface, Reihl *et al.* [2] see a 2x1 LEED pattern up to saturation of the work function, which is completely different from our complicated LEED diagram of Figure 4.1(a). However, as the LEED pattern does not change, the π-bonded chains remain up to K saturation coverage in agreement with the conclusion of our study. Using angle-resolved inverse photoemission, they observe a Fermi level crossing for angle-resolved inverse photoemission at saturation coverage, indicating metallization of the surface. As seen in Figure 4.6, the K 3p lineshape from our saturation coverage K/Si(111)1x1 surface also indicate a metallic surface. The angle-integrated photemission valence band spectra of

Reihl *et al.* (Figure 4.1 of Ref. 2) taken at photon energy 21.2 eV are qualitatively similar to our spectra at 65 eV (Figure 4.8) at low coverages, with a shift of the surface peak by 0.17 eV after the first dose. Reihl *et al.* find that their angle-resolved inverse photoemission measurements of the empty state bands of the saturation coverage K/Si(111)2x1 surface are in agreement with the theoretical band calculations of Ciraci and Batra [6] and of Ishida *et al.* [20]. Both of these theoretical papers have models of a saturation coverage (one K atom per surface Si atom) K/Si(111) surface with a K overlayer bonding to an underlying π-bonded chain structure. In particular, Ciraci and Batra's model involves K adsorbing to the side of the π-bonded chains in tilted hexagon sites. This model is similar to the one we will present for the K adsorption site for the annealed K/Si(111)3x1 surface in the XSW study below.

We conclude that lack of large changes in the K 3p, Si 2p, and valence band photoemission spectra as K is adsorbed up to saturation coverage indicates that the π-bonded Si chains are stable to K adsorption. The complicated LEED patterns of the K/Si(111) phase diagram can be attributed to the K overlayer, while the underlying chains maintain a 2x1 part of the patterns at low coverage and keep the directionality of the patterns at higher coverage. Even at saturation K coverage, the 1x1 pattern is caused by the K overlayer which covers the 2x1 periodicity of the underlying chains. The variety of LEED patterns are attempts by the potassium adatoms to arrange themselves in an ordered fashion on the underlying 2x1 chains. The stability of the π-bonded chain is also supported by Si standing wave data which appear similar to that of the clean surface.

Photoemission results and discussion - Annealed K/Si(111)3x1 surface

The cleaved Si(111) crystal dosed with K to coverages near saturation reverts to a multi-domain 3x1 LEED phase when annealed to 625°C. The LEED pattern of the annealed K/Si(111)3x1 surface has equal intensities for all three domains with no direction preference. Potassium also produces a single-domain 3x1 phase for room temperature dosing, with the 3x1 periodicity along the same direction as the original 2x1 periodicity of the clean surface. The 3-domain 3x1 surface can also be achieved by K dosing on a clean cleaved Si(111)2x1 or wafer Si(111)7x7 surface which is heated to 625°C during dosing. As will be discussed later, this procedure also produces a 3-domain 3x1 pattern for Na dosing upon cleaved Si(111); however, in this case the domains of the LEED pattern often are unequal in intensity. There is no corresponding annealed 3x1 phase for Cs/Si(111).

The potassium coverage remaining on the K/Si(111)3x1 surface after annealing can be determined from the K 3p lineshape, presented in Figures 4.11(a)–(b). In Figure 4.11(a) we compare the coverage of the annealed 3x1 surfaces to that of the low-coverage K/Si(111) phases from the room temperature dosing run. Figure 4.11(b) shows the K 3p peak for the cleaved surface before and after annealing. The surface before annealing showed a 2-domain $\sqrt{3}$x2 LEED pattern, which is the phase before the saturation 1x1 phase in the dosing progression. By comparing the normalized area to the area of the room temperature dosed saturation coverage, we find $F_K = 0.36\pm0.06$ for the annealed cleavable surface and $F_K = 0.28\pm0.06$ for the annealed wafer surface. As the size of K adatoms are such that almost one K adatom per surface Si atom can fit on the bulk-terminated surface, so that saturation coverage is near 1 monolayer (ML),

this K 3p data points towards a coverage of 1/3 ML for the 3x1 phase, identical to the case of Na/Si(111)3x1. We have no K 3p measurement of the room temperature 3x1 phase; however, from the LEED section, four separate LEED runs established the limits of the K coverage for the room temperature 3x1 phase to be $0.43 < F_K < 0.76$, possibly indicating 2/3 ML coverage. It is possible that the room temperature and annealed K/Si(111)3x1 surfaces are different in that the annealing may allow motion of the Si surface atoms to form chains of 3x1 periodicity rather than the 2x1 chains expected to remain underneath the 3x1 overlayer of the room temperature dosed phase. In addition, annealing the surface may remove excess K adsorbed in energetically unfavorable sites that may be present on room-temperature dosed surfaces. At 2/3 ML coverage, the number of potassium scatterers may be enough to mask the LEED pattern of the underlying Si surface, so the 3x1 periodicity only reflects the overlayer periodicity. As we shall discuss in the standing wave section, Si standing wave data are all the same shape regardless of whether the surface is room temperature dosed or annealed, or is wafer or cleavable, and this shape also is similar to the clean 2x1 surface. As this measurement is only sensitive to Si positions normal to the Si(111) surface, this means chains remain underneath the K overlayer on all of these surfaces; however, the lateral periodicity of the chains cannot be determined from this measurement, i.e. whether the chains are 2x1 or 3x1 under the potassium. We will compare the annealed and room-temperature-dosed K/Si(111)3x1 standing wave data after analysis of the annealed 3x1 data in the XSW section below.

The Si 2p spectra for the K/Si(111)3x1 cleaved and wafer surfaces and their corresponding clean 2x1 and 7x7 surfaces are presented in Figure 4.12. The lineshape of the Si 2p annealed 3x1 phase on the cleavable is not much different from that of the clean 2x1 surface, although the dip between the two main peaks of the lineshape is less deep for the 3x1 surface. In the case of the annealed K/Si(111)3x1 wafer surface, the Si 2p lineshape is different from the clean 7x7 lineshape. The Si 2p spectra for 3x1 on the wafer corresponds to the spectra for 25% 3x1 patches and 75% 7x7 patches for the Na/Si(111)3x1 surface in the study of Paggel *et al.* [21]. In this work, STM photographs indicate the 3x1 phase grows in patches of single-domain 3x1 on an otherwise 7x7 surface. If it is the case that only 25% of the surface is covered by the 3x1 phase, then the coverage within the patches necessarily is greater than the 1/3 ML suggested from the K 3p data of Figure 4.11.

The valence band spectra at photon energy 65 eV look different for the wafer and cleaved annealed K/Si(111)3x1 surface, since the initial spectra of the clean 2x1 and clean 7x7 are different. Figure 4.13 compares the clean 7x7 and annealed 3x1

valence band spectra for the Si(111) wafer to the corresponding spectra for the clean 2x1 and annealed 3x1 cleaved surfaces. However, qualitative changes in the valence band from clean to annealed 3x1 are similar for the two surface types. As with the low coverages room temperature potassium dosing run (see Figure 4.8), a state in the dip 0.4 eV below the initial surface state peak increases in intensity while the bulk states decrease due to the increased length Si bulk photoelectrons must travel to escape the surface. Although spectra were not taken for the room temperature single-domain K/Si(111) 3x1 phase, the annealed 3x1 surface valence band spectra of Figure 4.13 is similar to the room temperature dosed K/Si(111) surface valence band at intermediate coverages near the coverage for the single-domain 3x1 phase, as seen in Figure 4.8. This similarity along with the chain structure seen for the annealed 3x1 phase using STM reinforces our assertion that the π-bonded Si chains remain after room temperature K adsorption. As with the Si 2p spectra, the electronic structure of the 3x1 and 2x1 periodicity π-bonded chains may be similar so that the periodicity of the Si chains for the room temperature 3x1 phase cannot be determined from the photoemission data, but we argue that there may not be enough thermal energy or energy gain from K adsorption at room temperature to convert the chains from 2x1 to 3x1 periodicity. It is interesting to note that Erbudek and Fischer [22] see a transition of the cleaved Si(111) surface to 7x7 at an annealing temperature of 670°C, and that the K/Si(111)3x1 reconstruction can be formed on a clean Si(111)7x7 wafer. The conditions on the cleavable and wafer Si(111) surfaces are similar as the 3x1 phase is formed, and it is reasonable to assume the structure of these phases are the same. Indeed, the 3x1 phase is formed by K dosing on either a clean heated cleavable or wafer surface. In the case of the wafer, there is evidence of 7x7 patches in coexistence with the 3x1 phase, while for the cleaved surface, the lack of a preferred direction in the 3-domain 3x1 LEED pattern suggests the restructuring of the original 2x1 π-bonded chains to a 3x1 periodicity.

Cs/Si(111)

Work Function and Photoemission Results (for Coverage Determination)

The Cs/Si(111) interface work function difference from the clean surface was measured from differences the secondary electron cutoff. Figure 4.14 plots work

function difference as a function of coverage, which is represented as the percentage of Cs 4d peak area saturation. The work function is minimized at 93% saturation coverage at a value of -3.56 ± 0.10 eV, in agreement with the value of -3.7 eV measured by Magnusson and Reihl[3] for the cleaved Cs/Si(111) interface. Above this coverage, the work function begins to increase. Magnusson and Reihl[3] plot work function difference versus Cs dosing time. They interpreted the work function minimum as the saturation of Cs coverage and observed the $\sqrt{3}x\sqrt{3}$–R30° LEED pattern in the region of this minimum. They attributed the increase in the work function past the minimum to an oxidation effect. However, their work does not utilize a direct probe of Cs coverage such as Cs 4d photopeak area. Our interpretation of the work function minimum is that it occurs at slightly less than saturation coverage. At saturation coverage (see Figure 4.16), the Cs 4d photopeak shows a low-energy plasmon loss tail which can be attributed to a metallic overlayer. In addition, at this coverage the surface is not significantly oxidized, as we do not observe an oxide peak in the valence band photoemission spectra (see Figure 4.20). Therefore the increase in work function at saturation coverage is due to a weakening of the Cs-Si dipole strength as charge is returned from the Cs-Si bond to the metallic Cs overlayer.

LEED study – Room temperature cleaved Cs/Si(111) phase diagram

The phase diagram for the Cs/Si(111) interface is given in Figure 4.1(b). Three samples were studied in three separate experiments. Many of the patterns seen here are also seen for the K/Si(111) interface. In Figures 15(a)-(h) we present photographs of the observed Cs/Si(111) LEED patterns and descibe them below.

1. For $0.00 \leq F_{Cs} \leq 0.15$ the sample retains the 2x1 pattern of the clean Si(111) surface, as seen in Figure 4.15(a). The clean surface indicated by O's in Figure 4.1(b) was single-domain 2x1 with a weak second domain, while the other two samples were purely single-domain 2x1. In actuality, no 2x1 pattern has been observed after Cs dosing, but the upper limit of $F_{Cs} = 0.16$ reflects the finite size of the observed exposure steps.

2. For $0.08 \leq F_{Cs} \leq 0.40$ pairs of spots appear and straddle the 4th order positions halfway between the 2x1 spots as seen in Figure 4.15(b). A line from a 2x1 spot to a paired spot makes an angle of ~20° with the horizontal $[11\bar{2}]$ axis, i.e. the axis along which the 2x1 spots appear and which is perpendicular to the π-bonded chains in the Si(111) surface plane. In addition, the spacing is consistent with being $\sqrt{7}$

times the bulk lattice spacing. For this reason, we name this pattern "2x1 + $\sqrt{7}$x$\sqrt{7}$–R19°?". The question mark indicates that the pattern does not correspond to the typical $\sqrt{7}$x$\sqrt{7}$–R19° pattern, which does not have mirror symmetry about the horizontal axis as this LEED pattern does. As mentioned in the section above, this pattern is also seen for potassium on Si(111) for coverages of $0.14 \leq F_K \leq 0.40$.

3. For $0.21 \leq F_{Cs} \leq 0.57$ the LEED pattern is similar to that of the previous phase, as seen in Figure 4.15(c); however, the spacing between the paired spots increases and becomes consistent with the locations of spots in a $2\sqrt{3}$x$2\sqrt{3}$ pattern. The 2x1 pattern of the clean surface remains strong at this coverage, and only the $2\sqrt{3}$x$2\sqrt{3}$ spots closest to the bulk 1x1 spots are present. Gobeli *et al.*.[11] observed this pattern on this interface for a Cs coverage of $0.23 \leq F_{Cs} \leq 0.27$, where F_{Cs} is the fraction of work function saturation in their case. In addition, we observed this pattern for the K/Si(111) surface (see Figure 4.3(b)) for $0.12 \leq F_K \leq 0.46$, and called the pattern "2x1 + $2\sqrt{3}$x$2\sqrt{3}$–R30°".

4. For $0.35 \leq F_{Cs} \leq 0.73$ a threefold symmetric $\sqrt{3}$x$\sqrt{3}$–R30° pattern is present as well as the single-domain 2x1 pattern in the same direction as the 2x1 pattern of the clean surface, as seen in Figure 4.15(d). We name this structure "2x1 + $\sqrt{3}$x$\sqrt{3}$–R30°". At lower Cs coverages in this range the $2\sqrt{3}$x$2\sqrt{3}$ spots of the previous pattern can also be seen, but these fade with increasing coverage. Such a pattern indicates that Cs is forming its familiar $\sqrt{3}$x$\sqrt{3}$–R30° superstructure on top of the π-bonded chains of the clean Si(111)2x1 surface rather than reverting the surface to a bulk-terminated or other structure.

5. For $0.53 \leq F_{Cs} \leq 0.83$, the 2x1 spots of the previous phase disappear and only the $\sqrt{3}$x$\sqrt{3}$–R30° pattern remains, as seen in Figure 4.15(e). This pattern was observed by Gobeli *et al.* [11] for $0.33 \leq F_{Cs} \leq 0.53$ where F_{Cs} is the fraction of work function saturation in their case. Magnusson and Reihl [3] also observed this pattern but at coverages near work function saturation (F_{Cs}~1.00). In our earlier measurements we evaporated Cs on the cleaved Si(111) surface at a closer evaporation distance of 0.8 cm, as opposed to the 3.8 cm used in the dosing runs described here. These earlier samples exhibited a normalized Cd 3d peak area three times as large as those in the dosing progression. We believe such a coverage is close to work function saturation, although no work function data were taken for the earlier samples, and these earlier surfaces may be consistent with the $\sqrt{3}$x$\sqrt{3}$–R30° pattern seen by Magnusson and Reihl [3]. Our X-ray standing wave data suggest differences in the structure of the Cs/Si(111) $\sqrt{3}$x$\sqrt{3}$–R30° surfaces at higher and lower coverages; unfortunately, we have been unable to reproduce the higher coverage $\sqrt{3}$x$\sqrt{3}$–R30° pattern in a dosing run

in order to acquire work function difference data. As described above, the "2x1 + $\sqrt{3}$x$\sqrt{3}$–R30°" pattern directly proceding this phase suggests the $\sqrt{3}$x$\sqrt{3}$–R30° LEED pattern is formed by strongly scattering Cs atoms covering a surface of Si chains whose LEED pattern is damped out by overlayer scattering. As seen below, the higher coverage phase following the $\sqrt{3}$x$\sqrt{3}$–R30° pattern also exhibits a direction preference, supporting the idea of directional Si chains surviving Cs adsorption.

6. We previously have seen the zigzag pattern in Figure 4.15(f), which appears for a Cs coverage of $0.77 \leq F_{Cs} \leq 0.94$, for the K/Si(111) interface (see Figure 4.3(e)) for $0.58 \leq F_K \leq 0.76$. This pattern is a 2-domain $\sqrt{3}$x2 pattern. The third domain of the pattern is missing, and would have corresponded to alignment of the unit cell along the direction of the chains of the clean Si(111)2x1 surface. The missing domain suggests that chains still exist in the underlying Si surface and act to restrict the arrangement of the Cs adatoms at these coverages so that a directional preference appears in the LEED pattern.

7. For a very small coverage range $0.90 \leq F_{Cs} \leq 0.94$ a star-shaped pattern of 8th order spots is observed (photo not digitized). The vertices of the star pattern occur only at the spots corresponding to a 2x2 positions and not at the bulk 1x1 spots. This pattern is threefold symmetric, possibly indicating a reconstruction of the underlying surface, although the symmetry could be from the Cs overlayer alone.

8. For $0.92 \leq F_{Cs} \leq 0.97$, we see a 2x2 pattern with a halo of spots surrounding the 2nd order spots, as in Figure 4.15(g). These halo spots are estimated to be 12th order, although 10th order is possible due to the lack of precision of measuring distances on the photographs. Also, halo spots do not appear in the directions connecting the bulk 1x1 spots, which is similar to the previous star-shaped phase. This is the pattern at saturation coverage of Cs, unlike the pure 1x1 pattern seen for saturation dosings of K or Na on the cleaved Si(111) surface.

9. For further dosing on the saturation-dosed surface, i.e. $0.97 \leq F_{Cs} \leq 1.00$, the 2x2 spots and their halos fade to leave a 1x1 LEED pattern. This is probably a result of contamination on the saturation-dosed Cs/Si(111) surface, as the area of the Cs photopeak does not change with further dosing and the work function difference decreases in magnitude from its saturation value, an effect previously attributed to contamination [3,9]. Gobeli *et al.*. [11] also observed a 1x1 LEED pattern at saturation of the work function, $F_{Cs} \sim 1$.

Unlike K and Na, upon annealing Cs does not form a 3x1 phase, but rather forms a streaky pattern with 6th order spots along the directions of the original 2x1 chains, with 2nd order spots in the other domain directions. The preferred direction of

this pattern suggests large Cs is weakly bound to the cleavable Si surface and only attaches to the π-bonded chains without reconstructing them. The fact that there is a directionality to the LEED pattern even upon heating suggests 2x1 chains are stable upon the saturation coverage surface that was heated to produce these patterns. The π-bonded chains also are stable to Cs adsorption for room temperature dosing.

As in the case of K/Si(111), for Cs/Si(111) the LEED results of Magnusson and Reihl [3] differ from ours. They observe a $\sqrt{3}$x$\sqrt{3}$–R30° phase at saturation of the Cs/Si(111) work function and at saturation Cs coverage. Furthermore, they do angle-resolved inverse photoemission on the Cs/Si(111)$\sqrt{3}$x$\sqrt{3}$–R30° surface and find no Fermi level crossing, so they conclude the surface is semiconducting, which contrasts with our Cs photopeak data and the data of Tochihara *et al.* [4-5]. As seen in Figure 4.1(b), we find the LEED pattern of the saturation Cs/Si(111) surface to be 1x1 with halos of higher order spots around the second order spot positions, while the $\sqrt{3}$x$\sqrt{3}$–R30° phase exists only up to 88% of saturation Cs coverage. It is possible we achieved a $\sqrt{3}$x$\sqrt{3}$–R30° phase at saturation Cs coverage as well in some of our earlier runs, for which the distance from Cs evaporator to sample was 0.8 cm rather than the 3.8 cm used in the dosing runs which produced the spectra of Figures 16-21. In this case possible heating of the surface from the closer evaporator could occur, which may provide enough thermal motion to produce a $\sqrt{3}$x$\sqrt{3}$–R30° phase at saturation Cs coverage. In the standing wave section we present data for the low coverage $\sqrt{3}$x$\sqrt{3}$–R30° phase and find the triangulation for the Cs adatoms suggest Cs is in high symmetry states, suggesting a bulk-terminated Si surface; however, the Si standing wave suggests a reconstruction of the Si surface beneath the Cs overlayer for this surface. We provide a tentative explanation of this discrepancy in the XSW section below. Our photoemission and LEED data suggest that the $\sqrt{3}$x$\sqrt{3}$–R30° pattern is determined by the Cs overlayer and the underlying Si surface remains in π-bonded chains.

Photoemission results and discussion - Room temperature cleaved Cs/Si(111) surfaces

In this section we present the photoemission results of room temperature Cs dosing on the cleaved Si(111)2x1 surface. We use the same experimental technique that was used for the Na and K dosing runs above, using LEED and photoemission to characterize the clean cleaved Si(111) surface and the surface after each room temperature dosing. Figure 4.1(b) of the LEED results section shows the Cs/Si(111)

phase diagram as a function of percentage Cs saturation coverage. We observed nine Cs/Si(111) phases, slightly more than the seven K/Si(111) phases of Figure 4.1(a). However, several of the phases seen for K and for Cs are identical, including the low coverage 2x1 + $\sqrt{7}$x$\sqrt{7}$–R19° and 2x1 + 2$\sqrt{3}$x2$\sqrt{3}$–R30° phases and the higher coverage 2-domain $\sqrt{3}$x2 phase. More importantly, the order of progression of the phases is the same, suggesting a similar picture for K and Cs interaction with the Si(111) surface. The main differences in the phase diagrams are the Cs/Si(111)$\sqrt{3}$x$\sqrt{3}$–R30° phase replacing the single-domain K/Si(111)3x1 phase in the dosing sequence for Cs, and the additional halos of higher-order spots on the saturation coverage Cs/Si(111)1x1 phase, which are absent for saturation coverage K/Si(111)1x1. From the similarity of the LEED phase diagrams for K and Cs, one might expect that the corresponding photoemission spectra have similar behavior, and indeed this is the case, as we shall show below. As in the potassium dosing case but not like the sodium dosing case, the differences in the shapes of the photoemission spectra as Cs coverage increases are small. From LEED results, the photoemission results below and from XSW data we will conclude that K or Cs adsorb on top of a Si chain structure up to saturation dosage in similar overlayer arrangements and do not revert the Si surface back to bulk-terminated, unlike the case of Na adsorption. Three dosing runs were taken in separate experiments on Beam Line 8-1, and all produced similar spectra. In addition, several "single-shot" doses were made to produce various Cs/Si(111) phases, and the spectra taken on these surfaces were very similar to the corresponding phases in the dosing run. Unlike the K dosing run, there was no evidence of oxide contamination in the valence band spectra throughout the Cs dosing run. For Cs/Si(111) photoemission, the spectra taken at each dose include the Cs 4d photopeak at photon energy 120 eV, the Si 2p peak at photon energy 145 eV, the valence band region plus the Cs 5p peak at photon energy 65 eV, and the valence band at 20.8 eV. The photon energies for Si 2p and the valence band at 65 eV are the same as for the Na and K dosing runs, and were chosen to maximize surface sensitivity. The 20.8 eV valence band spectrum also was taken for the Na dosing run.

Both the Cs 4d and Cs 5p photoemission peaks have small enough binding energy to be seen with the photon energy range available on Beam Line 8-1, so both were observed with increasing Cs coverage on the cleaved Si(111) surface. Figure 4.16(a)-(b) show the progression of the Cs 4d photopeak in overlaid and stacked formats, while Figure 4.17 presents the Cs 5p spectra, including the sloping background from the clean 2x1 surface. As for the alkali metal photopeaks for the Na and K dosing run, both Cs peaks grow linearly with dosing time and then saturate. For

the last four doses, from 93% to 100% saturation coverage and starting at the 2-domain $\sqrt{3}$x2 LEED phase, the Cs photopeaks become increasingly asymmetric. This asymmetry also was observed by Tochihara *et al.* [5] for Cs 5p spectra of the cleaved Cs/Si(111) interface near saturation coverage. Tochihara attributed the asymmetry to a plasmon loss from a metallic Cs overlayer. Such a loss indicates metallic behavior of the Cs/Si(111) surface near saturation Cs coverage. A similar loss was seen for the K 3p spectra near saturation K coverage on the Si(111) surface (see Figure 4.6); for both alkali metals, near saturation coverage the distance between neighboring alkali atoms approaches that of the metal, so increased alkali-alkali interaction is expected. Unlike the K 3p spectra, which do not shift in energy with increasing coverage, the Cs 4d and Cs 5p peaks shift to 0.1-0.2 eV lower kinetic energy by the third Cs dose, and then apparently shift back to higher kinetic energy by 0.5 eV at saturation coverage. Despite the shifting in energy and the asymmetry at high coverage, the overall linewidth does not change significantly throughout the Cs dosing run, suggesting only one component of the spectrum and therefore one Cs adsorption, or at most several energetically equivalent sites. The single-component nature of the Cs photopeaks is also seen for the K 3p peak in the K dosing run, but is different from the Na 2p data (Figure 4.24), which have two components at low coverage and reduces to one component at high coverage with a discrete plasmon loss peak throughout Na dosing.

The changes in the Si 2p spectra as Cs coverage is increased on the cleaved Si(111) surface are shown in Figure 4.18(a). After the first Cs dose, the dip between the main peaks of the clean surface lineshape is removed, which is similar to how the Si 2p spectrum changes for the first Na or K doses on the clean surface. This change in lineshape results from a shift of the main surface component relative to the bulk component of the Si 2p spectrum. This change is shown in detail for the low-coverage Na/Si(111) surface by comparing the fits of Figures 25(b) and 25(c). After the first Cs dose, very little change is seen in the Si 2p lineshape. As the spectrum for the first dose requires four components to adequately fit it, the spectra for all the other Cs doses require this many components. The lack of a reduction of the number of Si 2p components at higher coverage, which we do see for Na/Si(111), suggests the underlying Si structure of the Cs/Si(111) surface is similar to that of the clean π-bonded chain surface at all coverages, in that there are more than two inequivalent Si atoms on the surface, as opposed to two different Si atoms (top layer and bulk) for the bulk-terminated surface. The energy shift of the lineshape with increasing Cs coverage is monotonically towards increasing kinetic energy, with a difference of 0.45 eV between the clean and saturation coverage main peak position. This shift is similar to the Cs

photopeak at higher coverages but not at low coverage, so there may be a combination of band bending and chemical shift effects taking place at low coverage. At coverages near Cs photopeak saturation, the Si 2p also develops a loss tail at low kinetic energy. Figure 4.18(b) plots the spectrum for the eighth Cs dose in comparison to earlier doses, with the peak height of all the spectra expanded to be the same height. This loss tail, also seen for the Cs photopeaks, may indicate the Si substrate is metallized at high Cs coverages.

The full spectra taken at 65 eV photon energy, which include the Cs 5p photopeak and the Cs/Si(111) valence band, is presented in Figure 4.19. A detail of the Cs 5p peak was presented above as Figure 4.17, while the valence band is given in overlaid and stacked formats in Figures 20(a)-(b). The valence band was also taken at photon energy 20.8 eV, given in Figures 21(a)-(b), which is a photon energy close to the He I line (21.2 eV) and at which the electron kinetic energies produce a less surface-sensitive spectrum than at 65 eV photon energy. Looking at Figure 4.20(a), we see the first Cs doses increase the electron density near the valence band maximum, and in particular the dip 0.4 eV below the surface state peak fills up while the surface state peak itself moves 0.2 eV to higher binding energy. This effect is identical to what occurs to the Na/Si(111) and K/Si(111) valence bands on the first alkali metal dose, as seen in Figures 26 and 8. As the LEED pattern still retains a 2x1 character with additional spots corresponding to the overlay arrangement, we conclude the 2x1 π-bonded chain is stable to the first alkali metal dose. The second Cs dose continues to increase electron density near the valence band maximum, as seen in Figure 4.20(a), while for later Cs doses all the features start decreasing in size, presumably due to the presence of a Cs overlayer. At higher doses the depth of the dip 0.4 eV below the surface decreases with respect to the surface state, as seen in Figure 4.20(b), but otherwise the valence band spectra do not change considerably throughout the Cs dosing run. The similarity of the higher coverage surface spectra to the spectra for the first Cs dose suggests the Si π-bonded chain remains throughout Cs dosing, as the first Cs dosed surface retains the π-bonded chains. The behavior of the valence band at 20.8 eV photon energy with increasing Cs coverage is similar to that at 65 eV, as seen by comparing Figures 20 and 21.

The valence band spectra of Figure 4.20 for our Cs dosing run look similar to the valence band spectra (photon energy 50 eV) of Tochihara *et al.* [4], who also looked at a Cs dosing progression on the cleaved Si(111)2x1 surface from the clean surface to saturation coverage. We see a shift of the surface state peak to 0.2 eV higher energy on the first Cs dose, corresponding to 33% saturation coverage, while

Tochihara *et al.* see this shift up to 31% saturation coverage. Both we and Tochihara *et al.* [4] see the Si surface state of the clean surface remain throughout Cs dosing, and we both conclude that the Si π-bonded chains are not destroyed upon Cs adsorption even up to saturation coverage. Our LEED data (Tochihara *et al.* did not report LEED data) also support this conclusion, as the 2-domain $\sqrt{3}$x2 LEED pattern at 81-98% saturation coverage maintains the directionality of the original clean 2x1 LEED pattern. Tochihara *et al.* observe a slight bulge in the slope of the cutoff near the Fermi edge and upon taking difference spectra with the bulk features aligned, they find a peak with a 1.5 eV plasmon loss which grows monotonically with Cs coverage. They attribute this peak to a Cs 6s state and claim to see a Fermi level crossing at saturation coverage, indicating a metallization of the Cs overlayer due to Cs-Cs interaction. This assertion of metallization is supported by their Cs 5p spectra which also shows a metallic loss [5], as discussed above. In our valence band spectra we see no evidence of a bulge just below the Fermi edge. As our analyzer is not fully angle-integrated and was taken at a different photon energy, it is possible we were not probing the part of the surface Brillouin zone at which the Fermi level crossing occurs. We certainly do see a metallic loss in our Cs 4d and Cs 5p at high Cs coverages in agreement with Tochihara *et al.* Thus our data compare well to that of Tochihara *et al.* [4-5] and we agree with their conclusion that Cs adsorbs weakly only the Si(111)2x1 surface, not destroying the underlying 2x1 π-bonded Si chains, and metallizing at high coverage due to increased Cs-Cs interaction. The measurements and conclusions of Tochihara *et al.* are given theoretical support by Ishida *et al.* [20]. Ishida *et al.* explain Tochihara's data using a buckled π-bonded chain model, with Cs bonding to both atoms in chain. The partial filling of their mixed Cs 6s–π^* band makes the surface metallic at this coverage. With saturation coverage Cs adsorption, the π-bonding band of the clean chain surface does not change much from the π band on the clean chain Si(111)2x1 surface, which indicates the stability of the chain to Cs adsorption. Ishida *et al.* also apply the same model of adsorption on top of the π-bonded chains for the saturation coverage K/Si(111) with very similar results, including a partially filled mixed K 4s–π^* band and an π bonding band mostly unchanged from the clean surface. The similarity of our photoemission spectra to that of the room temperature K/Si(111) dosing run as well as the number of identical LEED patterns in the phase diagrams for Cs and K also suggests that this weak interaction picture for Cs/Si(111) also applies to K/Si(111).

Na/Si(111)

Work Function and Photoemission Results (for Coverage Determination)

The work function difference $\Delta\Phi$, measured from changes in the secondary electron cutoff energy, decreases linearly with Na coverage through saturation of the Na 2p photopeak area (Figure 4.22). The value of the work function decrease at saturation coverage is $\Delta\Phi_{sat} = -2.91 \pm 0.10$ eV, which is averaged over four samples. Of these samples, only the sample in Figure 4.22 had a minimum before the saturation of the Na 2p photopeak was reached. A second sample had the work function plateau between 82% and 100% of Na 2p photopeak saturation with no increase at saturation, while for the other samples the lowest work function was at saturation coverage. This value of $\Delta\Phi_{sat}$ is in reasonable agreement with Reihl's value of $\Delta\Phi_{sat} = -2.7$ eV [1]. However, Reihl observed an actual work function minimum which he defined as 1 ML, and increase of the work function after further dosing was attributed to contamination. In addition, both our and Reihl's results are consistent with Northrup's calculated Na $\Delta\Phi_{sat} = -2.7$ eV for a bulk-terminated 1x1 surface[24].

LEED study- Room temperature cleaved Na/Si(111) phase diagram

Four Na dosing runs were performed on the cleaved Si(111) surface. The first two dosing runs, represented by X's and crossed squares in Figure 4.1(c), were done in an experiment before the reverse-view LEED optics was installed and no photographs were taken, while the other two samples both were from a later experiment and using the reverse-view LEED their LEED patterns were photographed. In addition, the evaporator-to-sample distance for the earlier experiment was 0.8 cm, while it was 3.8 cm for the later experiment.

For each sample, we observed three surface phases as Na coverage was increased. The various samples exhibited different "transition" patterns between the clean 2x1 and saturation 1x1 patterns, indicating a possible dependence of the phase diagram upon initial surface order. Photographs of the three Na/Si(111) surface LEED patterns are given in Figure 4.23.

1. For $0.00 \leq F_{Na} \leq 0.43$, the 2x1 pattern observed for the clean surface is maintained (see Figure 4.23(a)). Initial LEED patterns were single-domain (X's and crossed squares), two-domain (O's), and one-domain with weak second and third domains (triangles).

2. For two of the samples near $F_{Na} = 0.52$, the second order spots become considerably weaker than at lower coverages, and the LEED pattern approaches 1x1.

The weakening of the second order spots with increasing Na coverage appears gradual. We estimate the coverage range of this "1x1 w/weak 2x1" phase as $0.27 \leq F_{Na} \leq 0.66$. The length of the left side of the horizontal bar in Figure 4.1(c) is an artifact of choosing the midpoint of consecutive doses, as for the second sample (crossed squares) doses were larger and thus spaced further apart on the phase diagram than for the first sample (X's). If this sample is excluded from the calculation of limits, the coverage range becomes $0.43 \leq F_{Na} \leq 0.58$, which still surrounds the data point from the excluded sample ($F_{Na} = 0.53$).

3. For $0.26 \leq F_{Na} \leq 0.81$ and for three of the samples, a 2x2 phase is seen, as shown in Figure 4.23(b). This also could be three-domain 2x1, which appears identical to 2x2. However, since the clean surfaces had only one or two strong 2x1 domains (see above), a three-domain 2x1 pattern would rewuire restructuring of the Si surface domains, while a 2x2 pattern could be created from the Na overlayer alone on top of an unchanged π-bonded chain surface. For the second sample (crossed squares), this 2x2 appears on the bottom of the sample, while the "1x1 w/weak 2x1" pattern appears on the top. The clean surface of this sample was single-domain 2x1 , but the orientation of the this domain was different for the top and bottom halves of the sample. This indicates both "1x1 w/weak 2x1" and 2x2 patterns are possible transitional surface phases for intermediate Na coverage.

4. For $0.63 \leq F_{Na} \leq 0.83$, the 2x2 spots were seen to weak as Na coverage was increased and the pattern approached 1x1.

5. For $0.58 \leq F_{Na} \leq 1.00$, the LEED pattern reverts to 1x1, and remains 1x1 up to saturation coverage (see Figure 4.23(c)). This change to 1x1 near 1/2 ML and up to 1 ML agrees with the previous results of Reihl *et al.* [1]. However, they do not report observing a transitional 2x2 phase.

Photoemission results and discussion - Room temperature cleaved Na/Si(111) phase diagram

Three dosing runs of the Na/Si(111) interface were done over three experiments on Beam Line 8-1 at SSRL. One of the runs used an evaporator-sample distance of 3.8 cm, while the other two used a distance of 0.8 cm. LEED and photoemission were used to characterize the surface after each Na dosing. As seen from Figure 4.1(c) of the LEED results section, the three runs produced a similar phase diagram, characterized by a 2x1 phase at low coverages, a 2x2 transition phase around F_{Na} ~

0.5, followed by a 1x1 phase up to saturation coverage. As we describe below, the photoemission spectra of each of these phases are distinct from one another. The spectra taken at each dose include the Na 2p photopeak at photon energy 77 eV, the Si 2p peak at photon energy 145 eV, and the valence band region at photon energies of 65 eV and 20.8 eV. The photon energies for Si 2p and the valence band at $h\nu = 65$ eV were chosen so that the kinetic energies of the photoelectrons are close to the escape depth minimum of the "universal curve", making these spectra more sensitive to surface Si atoms with respect to bulk Si. The valence band was taken at $h\nu = 20.8$ eV to facilitate future comparison to spectra taken with the He I line (21.2 eV) and in hopes of improving resolution of features; these spectra are somewhat hampered by the large secondary electron background at these kinetic energies.

Na 2p spectra for Na coverages from 0 to 100% Na 2p area saturation are given in Figure 4.24(a), with the spectra labeled with the corresponding LEED pattern. The Na 2p peak area increases linearly with dosing time until saturation. Two components separated by ~0.5 eV can be seen in the peak at low coverages, and the relative weight of the component peaks depends on coverage and the corresponding LEED pattern. In addition, at lower kinetic energy plasmon loss peaks can be seen.

Figure 4.24(b) provides a detail of the Na 2p peak lineshape as Na coverage increases. The peak for the first dose, which retains the 2x1 LEED pattern of the clean surface, is about twice the width of the peak at high coverage (~1.0 eV vs. ~0.55 eV full width at half-maximum), indicating the existence of two photopeak components separated in energy by 0.5 eV. These separate components become more visible as coverage is increased and the LEED pattern becomes 2x2. For these intermediate coverages the lower binding energy (BE) component is occupied more heavily than the higher BE component, while for the first dose (2x1) they are occupied in almost equal proportion. This suggests more than one adsorption site on the low-coverage Na/Si(111) surface, such that the higher BE sites, while more readily filled by electrons donated by the Na adatoms, are less numerous on the 2x2 surface than the lower BE sites. As the LEED pattern changes to 1x1, the Na 2p peak narrows and shifts to lower BE position, indicating an overall decrease in the surface energy relative to the 2x2 surface. The reduction in number of Na 2p components suggests a single adsorption site and therefore a change in the underlying Si substrate structure such that the surface is more symmetric than the chains of the clean Si(111)2x1 surface. As described in the X-Ray Standing Wave (XSW) section of this report, XSW divided data indicate that the 1x1 surface is bulk-terminated. Both Northrup [24] and Moullet [25] model the Na/Si(111)1x1 surface as bulk-terminated and find a stable configuration with Na

adsorbed in the threefold hollow site H_3 or threefold filled T_4. The binding energy difference between the two sites is ~0.1 eV from these models, so the single Na 2p peak at this coverage could indicate either or both sites are filled.

Figure 4.24(c) provides a detail of the losses in the low kinetic energy tail of the Na 2p photopeak as Na coverage increases. At all Na coverage a loss peak is seen 2.4 eV below the peak position of the low BE component (seen in the 1x1 peak lineshape). At Na coverages near the transition to 1x1 and at higher doses another loss peak is seen 5.0 eV below the low BE peak component. These loss peaks indicate some collective effect resulting in loss of kinetic energy of photoemitted electrons. Alkali metals often exhibit plasmon losses, and we might attribute the 2.4 eV and 5.0 eV losses, to surface and bulk plasmon losses, respectively. However, ratio of bulk to surface plasmon loss energies should be $\sqrt{2}$ instead of the observed value of 2.1. The Si 2p photoemission spectra also show an increase in counts 2.4 eV below the main surface component for the larger Na doses, suggesting that the metallization required for plasmon losses is present in the silicon substrate and that the electrons donated by Na metallize the Si surface. This apparent metallic behavior conflicts with the results of Reihl et al. [1], who found the Na/Si(111) 1x1 surface to be semiconducting using angle-resolved direct and inverse photoemission spectroscopies.

The progression of the Si 2p lineshape (photon energy 145 eV) as Na coverage is increased is depicted in Figure 4.25(a). As Na coverage increases the overall area of the lineshape decreases due to the additional layer of atoms through which electrons emitted from Si atoms may inelastically scatter. The overall shape of the Si 2p peak for Na dosings corresponding to the 2x1, 2x2, and 1x1 LEED patterns are similar for dosings with the same LEED pattern and different for the three different LEED patterns. This indicates different geometrical and bonding arrangements of surface Si atoms for the three phases.

The Si 2p lineshape was fit using several component doublet peaks, convoluted with Voigt functions and using an integrated background. Figures 25(b)-(e) show the results of these fits for the clean 2x1 and Na-dosed 2x1, 2x2 and 1x1 surfaces, respectively. We use an experimental Gaussian width of 0.38 eV, a Lorentzian lifetime width of 0.07 eV, a spin-orbit splitting of 0.605 eV and a branching ratio of 2, which are the same values Woicik *et al.* [26] used in their fit of the clean Si(111)2x1 surface. As we used the same chamber, analyzer, and beam line as Woicik *et al.* did, we expect the Gaussian width to be similar. Four components were required to fit the clean surface Si 2p peak in Figure 4.3(b), with the bulk Si $2p_{1/2}$ component at kinetic energy 40.81 eV, and surface Si peaks at 0.337 eV, –0.646 eV, and –0.189 eV from the bulk

peak position. This is similar to the result of Woicik et al.[26], who find surface peaks displaced 0.415 eV, –0.64 eV, and –0.24 eV from the bulk peak. We deduce that the component labeled as bulk Si is indeed the bulk peak as its percentage of the total Si 2p peak area is stable at 34-39% for all Na doses, while the relative weights of the surface peaks varies with dosage and corresponding LEED pattern. Note that the kinetic energy chosen for the photoelectrons is very surface sensitive, with 61-66% of total Si 2p peak area coming from Si atoms in the top two bilayers of the surface.

After the first Na dose, $F_{Na} = 0.18$, there are still three surface components as for the clean surface; however, as seen in Figure 4.25(c) the main surface peak of the chain Si atoms shifts from –0.189 to –0.282 eV relative to the bulk peak. In addition, the two smaller surface peaks attributable to the second Si bilayer (lower chain of the π-bonded chain surface) change their relative weight somewhat. This suggests the Na is bonding to the Si chain atoms producing a chemical shift of –0.11 eV, and this bonding influences the 2nd layer Si atoms as well.

As Na coverage is increased into the 2x2 LEED phase, more of the spectral weight moves to the sides of the lineshape, indicating an increase in the relative areas of the smaller surface components at the expense of the main surface peak. The positions of the surface components relative to the bulk in Figure 4.25(d) (third Na dose, $F_{Na} = 0.53$) are within 0.04 eV of their values in Figure 4.25(c), indicating not much charge redistribution as the surface becomes 2x2. The change in the relative weights of the surface peaks suggests a surface relaxation such that the top and second Si layers (chains) move closer together so the component weights due to the inelastic escape depth effect become more similar. The similar energy positions suggests the bonding to Na is similar to the 2x1 case, so perhaps chains remain on the 2x2 surface. In addition, there is some weight at the left side of the spectrum (39 eV kinetic energy), which corresponds to 2.3 eV below the Si $2p_{3/2}$ part of the main surface component. This could be the formation of a surface plasmon loss at –2.7 eV, as we see in Figure 4.24(c) for the Na 2p spectrum for this Na coverage, indicating metallization of the Si substrate upon Na adsorption.

At the high coverages corresponding to the Na/Si(111) 1x1 phase, the number of components required to fit the Si 2p lineshape well reduces from four to two. Figure 4.25(e) shows the Si 2p lineshape at saturation coverage, $F_{Na} = 1.00$, which is composed of a bulk component of 36% total peak area and a single surface peak at –0.35 eV kinetic energy relative to the bulk. The loss at 39 eV kinetic energy also is more pronounced. The overall shift of the surface component at saturation Na coverage is 0.16 eV to higher binding energy relative to the bulk component when compared to

the clean surface. The existence of only one surface component supports the idea of a bulk-terminated surface, with the surface component corresponding to the Si atoms in the topmost layer which are bonded to the Na adatoms. The reduction of surface components for the 1x1 surface also was seen in the Na 2p photoemission data of Figure 4.24(b), with a conversion to only the single higher BE component at this coverage. Thus both Na 2p and Si 2p photoemission data support the idea of reduction of the number of Si surface atoms through reversion to a bulk-terminated structure, as well as indicating that the bulk-terminated surface is energetically more stable than the low-coverage chain surface since both Na 2p and Si 2p surface binding energies increase for the bulk-terminated surface.

In addition to the shifting in binding energy of the surface components relative to the bulk Si 2p component, the bulk component also shifts in absolute kinetic energy. This could indicate band bending caused by changes in the energy of surface states within the semiconductor bandgap. Unfortunately, comparison of bulk component energies are difficult since using different number of components in the fit shifts the bulk peak around considerably. All Na coverages produce an overall positive shift in kinetic energy from the clean surface value of the bulk peak energy. In the four component fits of Figures 25(c) and 25(d), the shift increases from +0.015 eV to +0.203 eV relative to the clean surface, while the two component fits of the higher Na coverage surface Si 2p peaks give +0.273 eV for the fifth Na dose and +0.209 eV for the saturation dose of Figure 4.25(e). The larger shift seen for the 2x2 and 1x1 surfaces may be a result of changes in surface states in the bandgap after the surface structure changes from the 2x1 chain structure.

Changes are also seen in the valence band photoemission spectra with increasing Na adsorption, particularly in the 4 eV region below the valence band maximum. Valence band spectra from 0% to 100% Na saturation were taken at both 65 eV and 20.8 eV photon energies, and the spectra are presented in Figures 26 and 27, respectively. For each numbered figure, graphs (a) and (b) are overlaid and stacked versions of the same series of spectra. The different photon energies used produce different surface sensitivities, as is seen by the larger surface state peak at the top of the valence band at high coverages in the 65 eV spectra of Figure 4.26 when compared to the 20.8 eV spectra of Figure 4.27. Qualitatively this surface peak is the most interesting portion of the progression of the valence band with Na dosings, and we will emphasize the changes in this peak below. The bulk Si features in the rest of the valence band (at -8.5 eV bulk 3p-like, -12.5 eV bulk 3p-3s-like, -14.5 eV bulk 3s-like) uniformly decrease in intensity as Na covers the surface and the distance photoelectrons

must travel from the bulk Si atoms to the surface without scattering increases. These bulk features also shift in energy as Na coverage changes; in particular, the feature near –12.5 eV moves to 0.3 eV higher kinetic energy by the fourth dose, then shifts back so that its position on the clean and Na-saturated surface are almost the same, as seen in Figures 27(a) and 26(b). As discussed above, the Si 2p bulk component also increases 0.3 eV in kinetic energy but ends up 0.2 eV to higher kinetic energy with respect to the clean surface. The peak at –8.5 eV, which is attributed to bulk Si 3p-like states, shifts uniformly 1.0 eV to lower kinetic energy, although it may contain surface states as well. The overall band bending effect of Na dosing on the surface is unclear from these results.

The peak at the top of the valence band exhibits a shift to higher BE as well as a large increase in intensity as Na coverage is increased. For the clean 2x1 surface, this peak corresponds to surface π states of the chain surface. After the first dose, this peak remains; however, the dip between this peak and the wide peak at –7.6 eV is not as deep, suggesting either an increase in electron density in the region of this dip (about 0.3 eV below the surface peak) or a decrease in the surface peak intensity; this change is best seen in Figure 4.27(b). This kind of change is also seen in the valence band at the beginning of the K and Cs dosing runs, including a shift of this peak by 0.15 eV to lower kinetic energy. As the LEED remains 2x1 after the first Na dose, the surface peak still can be attributed to a π-bonded chain structure. For later doses the identification of this peak as adatom or substrate-related is less clear. Through the intermediate coverages for which the LEED pattern is 2x2, the energy of this peak remains constant while its absolute intensity increases in the case of the surface-sensitive 65 eV spectra of Figure 4.26. Here Na adatoms are supplying electrons to the state at the energy of this peak, so the peak represents some bonding between the Na and Si atoms. As the LEED pattern converts to 1x1 and Na coverages increases to saturation, the valence band peak also increases and saturates, while shifting to a binding energy 0.5 eV than the original Si surface state of the clean surface. This peak's continuing increase and saturation confirms that it reflects electrons occupying an Na-Si chemical bond. This prominent feature of the Na/Si(111)1x1 valence band spectrum was observed by Reihl *et al.*[1], and they investigated the dispersion of this peak on the Na-saturated surface using angle-resolved photoemission. Their experimental results revealed a band that was fairly flat 0.5 eV below the valence band maximum for the parts of the Brillouin zone where it did not coincide with the bulk bands. These measurements, as well as angle-resolved inverse photoemission mappings of empty surface bands, coincide with the calculated bands of Northrup [24]

and of Moullet et al. [25] who both use a bulk-terminated model of the surface. The observed filled band is derived from an ionic Na 3s - Si 3p bond between the bulk-terminated top Si layer and Na adatoms in either a threefold filled (T_4) or threefold hollow (H_3) site. The K and Cs-dosed Si(111) surfaces have no such feature in their valence band spectra (see Figures 13 and 20) suggesting a distinctly different interaction with the Si(111) substrate than for Na. Thus, through Na dosing on the cleaved Si(111) surface, we see the removal of the surface state of the π-bonded Si chains at the top of the valence band and its replacement by a Na-Si bonding state also at the top of the valence band but at higher binding energy. The transition is smooth and it is unclear from the valence band spectra at what point the chain reconstruction reverts to a bulk-terminated surface, and whether the 2x2 transition phase represents coexistent patches of bulk-terminated Si and Si chains or whether it is a intermediate reconstruction over the entire surface.

The photoemission and LEED data for the room temperature Na and K dosing runs on the cleaved Si(111)2x1 surface indicate different structural and bonding interaction for each of these alkali metals. Figures 1(a) and 1(c) of the LEED section show the difference in complexity of the K and Na phase diagrams for submonolayer coverages, with the sodium diagram having three main phases (2x1 at low coverage, 2x2 at intermediate coverage, and 1x1 at a saturation coverage of 1ML) and potassium having seven. The Na 2p spectra (Figure 4.24) show two components at low coverage reducing to a single component at high coverage, while the K 3p spectra (Figure 4.6) maintain the same width throughout dosing. The Si 2p spectra show three distinct lineshapes corresponding to the three LEED phases for Na dosing (Figure 4.25), also with a reduction in the number of components at high coverage, while the corresponding spectra for K dosing (Figure 4.7) shows small changes and no reduction in the number of components. This reduction of components for the high-coverage Na/Si(111)1x1 suggests a conversion to a bulk-terminated surface, while the lack of such a reduction in the potassium case suggests the π-bonded chains of the clean surface are stable to K adsorption. Si standing wave data also suggest that the Na/Si(111)1x1 surface has a bulk-terminated Si structure while the K/Si(111)1x1 surface has underlying Si chains. The valence band data for the two alkali metals are also different, with a large peak forming for the Na/Si(111) surface (Figure 4.26) which is absent in the K/Si(111) case (Figure 4.8). This suggests a less strong interaction between K and Si on the cleaved Si(111)2x1 surface than between Na and Si, at least for room temperature dosing. While Na has multiple sites at low coverage and successfully bulk-terminated the Si(111) surface at high coverage, K adsorbs on

top of the π-bonded chains in arrangements of varying long-range periodicity but in a single adsorption site or possibly multiple sites with very similar binding energy. This difference in behavior may be due to the relative sizes of the Na and K adatoms, so that Na atoms can penetrate more readily into the Si(111)2x1 surface than the larger K atoms.

Photoemission results and discussion - Annealed Na/Si(111)3x1 surface

In addition to the three phases seen for room temperature dosing, the Na/Si(111) 1x1 surface annealed to 625°C converts to a multidomain 3x1 rcconstruction. As discussed in the LEED section, the domain of 3x1 pattern along the chain direction of the original clean 2x1 surface often has higher intensity than the other two domains. This suggests the original π-bonded Si chains either remain or are restored on the surface upon annealing, or at least that the clean surface structure influences the formation of the annealed surface structure. The multi-domain 3x1 surface is also seen by annealing high potassium coverage K/Si(111) surfaces to 625°C.

As seen in Figure 4.28, the Na 2p peak of the Na/Si(111)3x1 surface has an intensity between those of the first and second dose of the room-temperature Na dosed surface. The peak area corresponds to 28±3% saturation coverage. As the Na covalent radius is such that one Na atom per surface Si atom can fit on the Si(111) surface, saturation coverage corresponds to 1 monolayer (ML), so the 3x1 surface has an Na coverage of 0.28±0.03 ML. There has been a recent discussion of the absolute coverage of the Na/Si(111)3x1 surface. Our result agrees with the 1/3 ML coverage suggested by the photoemission data of Okuda *et al.*[27] and RHEED data of Daimon and Ino [28]. It disagrees with the conclusion of Jeon *et al.*[29] concerning their STM data which depict bright double rows of atoms on the surface. Jeon *et al.*[29] attribute the double rows to Na electronic states so that the coverage would be 2/3 ML, while Okuda *et al.* [27] suggest that these STM double rows can be attributed to states in a Si π-bonded chain with 3x1 periodicity and that Na occupies the valleys between the chains at a coverage of 1/3 ML. At 1/3 ML coverage, the Na 2p spectra in Figure 4.28 also has a loss peak at 3.1 eV below the main peak, unlike the room temperature dosed surface plasmon loss of 2.4 eV below the low binding energy Na 2p component. This spectrum and its loss peak match the Na 2p spectrum for annealed Na/Si(111)3x1 prepared on a Si(111) wafer with an initial 7x7 LEED pattern, seen in Figure 4.7 of

Paggel et al. [21]. Also, since lower coverage room-temperature dosed Na/Si(111) surfaces have two components separated by 0.5 eV, the Na 2p spectrum of our Figure 4.28 may be solely the low BE component seen at low coverages and not for the bulk-terminated 1x1 surface. The width of the Na 2p peak is smaller than that of the low-coverage RT-dosed surfaces in Figure 4.28, and is about the same width of the single-component 1x1 Na 2p spectrum of Figure 4.24(a). The energy and width of the peak suggests Na is solely bonded to the Si π-bonded chain, as the chain is expected to remain for the low coverage room temperature surfaces which have a low BE component in the Na 2p spectrum. The STM data of Jeon *et al.*[29] as well as our standing wave data support Si chain structure on the Na/Si(111)3x1 surface.

The lineshape Si 2p spectrum of the annealed cleaved Na/Si(111)3x1 surface is compared to those of the room-temperature dosed surfaces in Figure 4.29. The lineshape is most similar to that of the 2x2 surface after the 3rd room temperature dosing, with a considerable shoulder at low BE and no dip between the two main peaks overall lineshape. The comparable fit of the third RT dose Si 2p spectrum is given in Figure 4.25(c). The 3x1 lineshape on the cleavable surface looks similar to the Si 2p spectrum of the Si(111) wafer with 100% 3x1 and 0% 7x7 regions on the surface, as measured by Paggel *et al.*[21] This suggests the structure of the annealed Na/Si(111)3x1 interface is identical on the cleaved and wafer surfaces. Paggel also observes patches of single-direction chains alongside 7x7 patches using STM on the Na/Si(111)3x1 surface in the same paper. There probably are chains on the 2x2 surface as well, which is supported by the similarity of the Si 2p spectrum for the 3x1 and 2x2 surfaces.

The valence band of the annealed Na/Si(111)3x1 surface is compared to those of the different phases of the room temperature Na dosing progression in Figures 30(a) and 30(b), for photon energies of 65 eV and 20.8 eV, respectively. The large peak seen in the valence band for the higher coverage 2x2 and 1x1 LEED patterns is absent in the valence band of the 3x1 surface. The lineshape of the 3x1 valence band is closest to that of the first dose 2x1 lineshape in Figure 4.30; however, the dip seen below the surface state at the top of the valence band for the 2x1 surface is replaced by a slight peak for the 3x1 surface. The surface peak appears to remain as well, perhaps indicating a chain structure similar to the clean 2x1 surface, which has been observed with STM. The binding energy of this slight peak is greater than that of the main peak for the saturation coverage 1x1 surface, which suggests the 3x1 surface is a different and more stable bonding configuration than the bulk-terminated 1x1 surface. Since not all the Na desorbs upon annealing but rather the 3x1 reconstruction appears with 1/3

ML Na remaining, this also indicates the 3x1 surface's stability. As described later in this section, the annealed K/Si(111)3x1 valence band also fills in below the surface state with the surface state remaining. We note that the spectra of Figures 6–8 are the only photoemission data taken for the Na 3x1 surface, and they were taken on the same surface as a long room temperature dosing run; however, there is no oxide peak in the valence bands of Figure 4.30, so the surface is not contaminated during the run.

Comparing the Na and K annealed 3x1 surfaces, the Si 2p spectra for the Na 3x1 (Figure 4.29) and K 3x1 (Figure 4.12) surfaces are very similar, suggesting the Si atomic structure and type of bonding to the alkali adsorbate is the same for both Na and K. In addition, the coverage for both phases is close to 1/3 ML, and both surfaces show resistance to oxygen contamination as they can last more than a day in vacuum without degradation of the LEED and without a noticeable O 1s signal. This passivation to oxygen was previously observed for the Na/Si(111)3x1 surface by Tikhov *et al.* [13]. The passivation is strikingly different from the alkali metal induced catalysis of oxidation of other alkali metal/Si(111) surfaces. The resistance to oxidation over the time periods required for taking an XSW data set (typically 6-8 hrs) make the annealed 3x1 surfaces better candidates for an XSW study than the catalytic RT-dosed surfaces. The similarity of the structure of the annealed Na/Si(111)3x1 and K/Si(111)3x1 surfaces has been concluded by Fan and Ignatiev [23], whose measured LEED I-V curves are very similar for the two surfaces. As we describe below, the AM and Si standing wave data for these two surfaces also are similar, which also indicates the structural similarity of the annealed Na and K 3x1 surfaces.

Conclusions

We have presented photoemission spectra of alkali metal photopeak peaks, the surface-sensitive Si 2p photopeak, and the valence band region as well as work function (secondary electron cutoff) data for many Na, K, and Cs coverages on the cleaved Si(111)2x1 surfaces ranging from the clean surface to 100% alkali metal saturation of the surface. In addition, spectra are presented for the annealed cleaved Na/Si(111)3x1 surface and the annealed cleaved and wafer K/Si(111)3x1 surfaces. Some of this data previously have been taken by others. In particular, the annealed wafer Na/Si(111)3x1 and K/Si(111)3x1 surfaces are well-studied. Work function and angle-resolved inverse photoemission data had been taken on the cleaved Na/Si(111) [1], K/Si(111) [2], and Cs/Si(111) [3] surfaces by Reihl and Magnusson. Tochihara *et*

al. took photoemission data on the Cs 5p and valence band of the cleaved Cs/Si(111) surface [4-5]. Our work function data are in agreement with Reihl and Magnusson for all three surfaces, while our photoemission data of the Cs/Si(111) surface match that of Tochihara *et al.* The new contributions of our work include detailed LEED phase diagrams for all three alkali metal / Si(111) surfaces; photoemission data for adsorbate and substrate atoms for Na/Si(111) and K/Si(111) surfaces at many coverages; the discovery that annealed 3x1 phases can be produced on cleaved Si(111)2x1 surfaces under similar conditions as on the Si(111)7x7 wafer surface; X-ray standing wave data on many of these surface which provide structural information of adsorbate and substrate atom positions; and conclusions about the structure of these surfaces which are supported by the independent techniques of LEED, photoemission, and X-ray standing waves.

As seen from the LEED phase diagrams in Figure 4.1, the K/Si(111) and Cs/Si(111) phase diagrams have a similar sequence of many identical LEED patterns with increasing coverage. The behavior of all the photoemission spectra also show similar trends with increasing K or Cs coverage (Figures 6-13 for K/Si(111), Figures 16-21 for Cs/Si(111)); in particular, there is not much change in the lineshape of the alkali metal core levels, the Si 2p peak, or the valence band past the initial K or Cs dose. As the LEED of the initial dose as well as the photoemission data suggest the K/Si(111) and Cs/Si(111) surfaces retain the π-bonded Si chains after the initial dose, we can conclude from the lack of change in the spectra that the π-bonded chains remain underneath the K or Cs overlayer even up to saturation coverage. The directionality of the LEED patterns of the K/Si(111) surface and Cs/Si(111) surfaces along the original clean 2x1 chain direction (e.g. the high coverage 2-domain $\sqrt{3}$x2 phase) also support this conclusion of stable Si chains. Si standing wave data presented below also suggest the Si remains reconstructed under the alkali overlayer for the K/Si(111)1x1, K/Si(111)3x1, and Cs/Si(111)$\sqrt{3}$x$\sqrt{3}$–R30° surfaces. The experimental work of Tochihara *et al.* [4-5] and the theoretical band calculations of Ishida *et al.* [20] also confirm the stability of the π-bonded chains of the Si(111)2x1 surface to K or Cs adsorption.

The complexity of the K/Si(111) and Cs/Si(111) phase diagrams is contrasted with the relative simplicity of the Na/Si(111) phase diagram. The photoemission data for the Na/Si(111) surface with increasing Na coverage also are qualitatively different than the behavior of the K/Si(111) and Cs/Si(111) photoemission data. Instead of a lack of change with increasing alkali coverage, for Na/Si(111) we see definite changes in the Na 2p, Si 2p, and valence band spectra (Figures 24-27) corresponding to each of

the three main LEED phases of the phase diagram, i.e. 2x1 at low coverage, 2x2 at intermediate coverage, and 1x1 at saturation. In particular, we conclude that the reduction in the number of components of the Si 2p (and Na 2p) spectra for the 1x1 phase indicates a conversion of the reconstructed π-bonded Si chains of the clean Si(111)2x1 and Na/Si(111)2x1 surfaces to the bulk-terminated Si(111) structure for Na/Si(111)1x1. Unlike the K/Si(111)1x1 and Cs/Si(111)1x1 where the 1x1 LEED pattern is determined by the alkali metal overlayer and not the underlying reconstructed Si substrate, the LEED pattern of the Na/Si(111)1x1 phase reflects the substrate periodicity of a bulk-terminated Si surface. As we shall see below, Si X-ray standing wave data support the conclusion that the Si bulk structure is no longer reconstructed. In addition, the Na/Si(111) valence band spectra (Figure 4.26) shows a large peak that grows with increasing Na coverage, which is absent in the K/Si(111) and Cs/Si(111) valence band spectra, suggesting the band structure of the Na/Si(111) surface is distinct from those of K/Si(111) and Cs/Si(111). The experimental results of Reihl *et al.* [1] confirm the existence of this valence band peak, and their investigation the dispersion of this peak on the Na-saturated surface using angle-resolved photoemission was found to agree with the calculated bands of Northrup [24] and of Moullet *et al.* [25], both of whom propose a bulk-terminated model of the Na/Si(111)1x1 surface. For room tempertature dosing there are clear similarities between K and Cs adsorption upon the Si(111) surface, while Na adsorption differs. However, for the annealed AM/Si(111)3x1 surfaces, it is K and Na which are similar, with no corresponding Cs 3x1 structure. This behavior indicates the important roles of both annealing and adatom size upon interface formation and energetics. The differing behavior of K adsorption upon room temperature and annealed surfaces can be attributed to the intermediate size of potassium, and make the K/Si(111) surfaces the most complex of the three alkalis studied, in terms of determining the nature of the adsorbate/substrate interaction.

Initially, photoemission and LEED were utilized to characterize surfaces to be studied via XSW, in particular the saturation coverage surfaces of Na/Si(111)1x1, K/Si(111)2x1, and Cs/Si(111)$\sqrt{3}$x$\sqrt{3}$–R30° observed by Reihl and Magnusson [1-3]. When we observed the K/Si(111)1x1 and Cs/Si(111)1x1 patterns at saturation coverage, the photoemission and LEED studies were extended to submonolayer coverages and the room temperature phase diagrams were compiled for Na/Si(111), K/Si(111), and Cs/Si(111). From these phase diagrams, we selected the Na 1x1, K 1x1, and Cs $\sqrt{3}$x$\sqrt{3}$–R30° phases for XSW study as the coverage on these surfaces was at or near saturation, so the alkali absorption signal was maximized. As discussed above, from the changes in photoemission and LEED with increasing alkali coverage,

we expected a bulk-terminated surface for Na/Si(111)1x1 and an underlying chain for K/Si(111)1x1, and Cs/Si(111)$\sqrt{3}$x$\sqrt{3}$–R30°. In addition, we chose to study the annealed Na/Si(111)3x1 and annealed K/Si(111)3x1 phases as there were many models of these surfaces in the literature and their coverage (1/6 to 1/3 of saturation coverage) was more controllable than the room-temperature dosed surfaces. Photoemission spectra, and in particular the valence band spectra, indicated that the underlying structure of Na 3x1 and K 3x1 was similar, although K/Si(111)3x1 has a 3-domain LEED pattern with equal intensity domains, while the Na/Si(111)3x1 LEED pattern is 3-domain with the domain along the original 2x1 direction being more intense. The room-temperature dosed K/Si(111)3x1 surface, which has a single-domain 3x1 pattern, was also chosen for XSW study to compare to the annealed K 3x1 phase. Thus observing the changes in LEED patterns and photoemission spectra with increasing alkali metal coverage provided hints as to the underlying Si structure of many of the surfaces to be studied with XSW, in addition to setting limits on the actual alkali coverage.

References

[1] B. Reihl, S. L. Sorensen, R. Dudde, and K.O. Magnusson, Phys. Rev. B 46 (1992) 1838.

[2] B. Reihl and K.O. Magnusson, Phys. Rev. B 42 (1990) 11839.

[3] K.O. Magnusson and B. Reihl, Phys. Rev. B 39 (1989) 10456.

[4] H. Tochihara, M. Kubota, M. Miyao, and Y. Murata, Surf. Sci. 158 (1985) 497.

[5] H. Tochihara, M. Kubota, and Y. Murata, Sol. St. Comm. 57 (1986) 437.

[6] S. Ciraci and I.P. Batra, Phys. Rev. Lett. 58 (1987) 1982.

[7] I.P. Batra and S. Ciraci, Phys. Rev. B 37 (1988) 8432.

[8] Fu Huaxiang and Ye Ling, Surf. Sci. 250 (1991) L373.

[9] E.M. Oellig and R. Miranda, Surf. Sci. 177 (1986) L947.

[10] K.O. Magnusson and B. Reihl, Phys. Rev. B 41 (1990) 12071.

[11] G.W. Gobeli, J.J. Lander and J. Morrison, J. Appl. Phys. 37 (1966) 203.

[12] E. J. Nelson, T. Kendelewicz, P. Liu, and P. Pianetta, Surf. Sci. 380 (1997) 365.

[13] M. Tikhov, L. Surnev and M. Kiskinova, Phys. Rev. B 44 (1991) 3222.

[14] H.H. Weitering, N.J. DiNardo, R. Pérez-Sandoz, J. Chen and E.J. Mele, Phys. Rev. B 49 (1994) 16837.

[15] K. Sakamoto, T. Okuda, H. Nishimoto, H. Daimon, S. Suga, T. Kinoshita and A. Kakizaki, Phys. Rev. B 50 (1994) 1725.

[16] K.C. Pandey, Phys. Rev. Lett. 47 (1981) 1913.

[17] S.C. Erwin, Phys. Rev. Lett. 75 (1995) 1973.

[18] T. Hashizume, M. Katayama, D. Jeon, M. Aono and T. Sakurai, Jpn. J. Appl. Phys. 32 (1993) L1263.

[19] S. Doniac and M. Sunjic, J. Phys. C 3 (1970) 285.

[20] H. Ishida, K. Terakura, and M. Tsukada, Sol. St. Comm. 59 (1986) 365.

[21] J. J. Paggel, G. Neuhold, H. Haak, and K. Horn, Phys. Rev. B 52 (1995) 5813.

[22] M. Erbudak and T. E. Fischer, Phys. Rev. Lett. 29 (1972) 732.

[23] W. C. Fan and A. Ignatiev, Phys. Rev. B 41 (1990) 3592.

[24] J. E. Northrup, J. Vac. Sci. Tech. A 4 (1986) 1404.

[25] I. Moullet, W. Andreoni and M. Parrinello, Surf. Sci. 269-270 (1992) 1000.

[26] J. C. Woicik, T. Kendelewicz, K. Miyano, R. Cao, P. Pianetta, I. Lindau, and W. E. Spicer, Physica Scripta 41 (1990) 1034.

[27] T. Okuda, H. Sigeoka, H. Daimon, S. Suga, T. Kinoshita, and A. Kakizaki, Surf. Sci. 321 (1994) 105.

[28] H. Daimon and S. Ino, Surf. Sci. 164 (1985) 320.

[29] D. Jeon, T. Hashizume, T. Sakurai, and R. F. Willis, Phys. Rev. Lett. 69 (1992) 1419.

Table 4.1. Work Function Differences of the Various K/Si(111) Surfaces

K/Si(111) surface	*Work Function Difference (eV)*
2x1–>3x1 3-domain after anneal	$\Delta F = -1.62$ eV
2x1–>2x1 + $2\sqrt{3}$x$2\sqrt{3}$–R30°	$\Delta F = -2.32$ eV
2x1–>mixed 2x1 + 3x1	$\Delta F = -2.58$ eV
2x1–>one-domain 3x1 (RT dosing)	$\Delta F = -3.21$ eV
2x1–>two-domain $\sqrt{3}$x2	$\Delta F = -3.15$ eV
7x7–>3x1	$\Delta F = -0.90$ eV

Table 4.2. Contamination "Lifetimes" of the Various K/Si(111) Surface LEED Patterns

K/Si(111) surface	*Lifetime(hrs)*	*Pressure(torr)*
2x1–>3x1 3-domain after anneal	>14 hrs	$3x10^{-11}$ torr
2x1–>2x1 + $2\sqrt{3}x2\sqrt{3}$–R30°	2 hrs	$6x10^{-11}$ torr
2x1–>mixed 2x1 + 3x1	2.7 hrs	$3x10^{-11}$ torr
2x1–>one-domain 3x1 (RT dosing)	7 hrs	$3x10^{-11}$ torr
2x1–>two-domain $\sqrt{3}x2$	2 hrs	$3x10^{-11}$ torr

Figure 4.1(a). Surface phase diagrams for room-temperature K adsorption on the cleaved Si(111) surface. Error bars represent the observed range for a LEED pattern over many samples, and different samples are represented by different symbols. Coverage is determined by the fraction of the K 3p photoemission peak area relative to the area at saturation coverage.

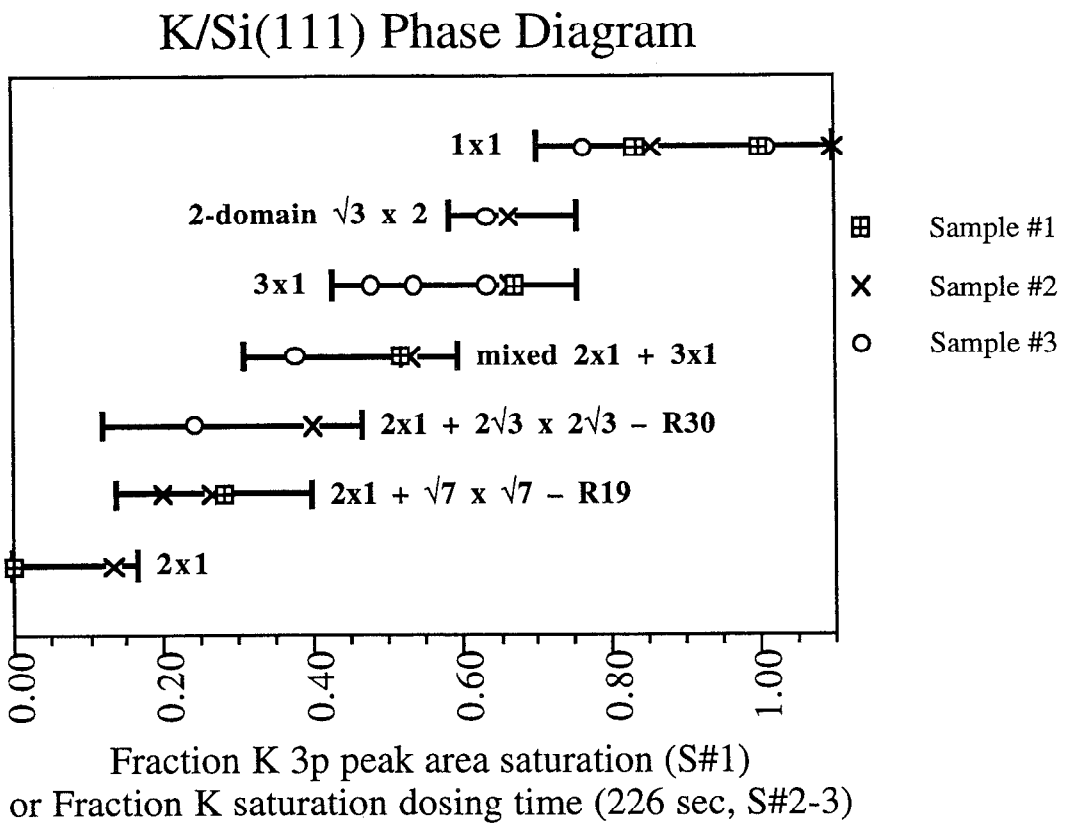

Figure 4.1(b). Surface phase diagrams for room-temperature Cs adsorption on the cleaved Si(111) surface. Error bars represent the observed range for a LEED pattern over many samples, and different samples are represented by different symbols. Coverage is determined by the fraction of the Cs 4d photoemission peak area relative to the area at saturation coverage.

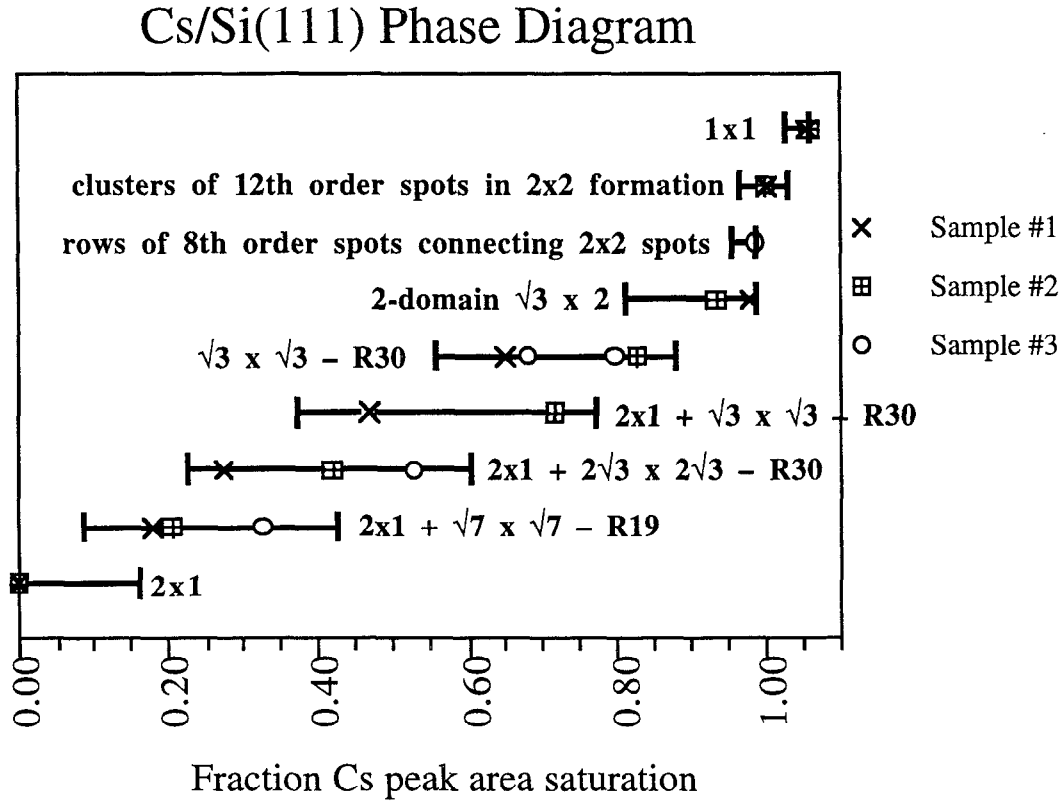

Figure 4.1(c). Surface phase diagrams for room-temperature Na adsorption on the cleaved Si(111) surface. Error bars represent the observed range for a LEED pattern over many samples, and different samples are represented by different symbols. Coverage is determined by the fraction of the Na 2p photoemission peak area relative to the area at saturation coverage.

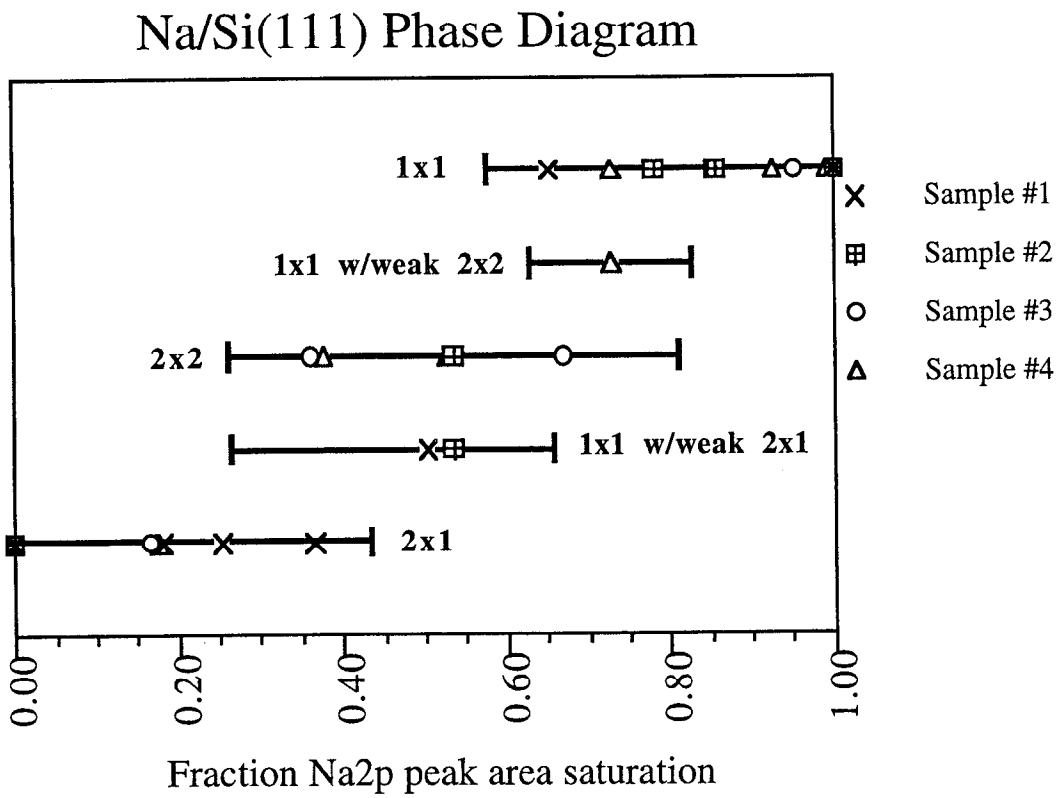

Figure 4.2. Work function difference (relative to the clean Si(111)2x1 surface) for the K/Si(111) interface as a function of K coverage, as determined by fraction of K 3p peak area saturation. Approximate ranges of observed LEED patterns are indicated.

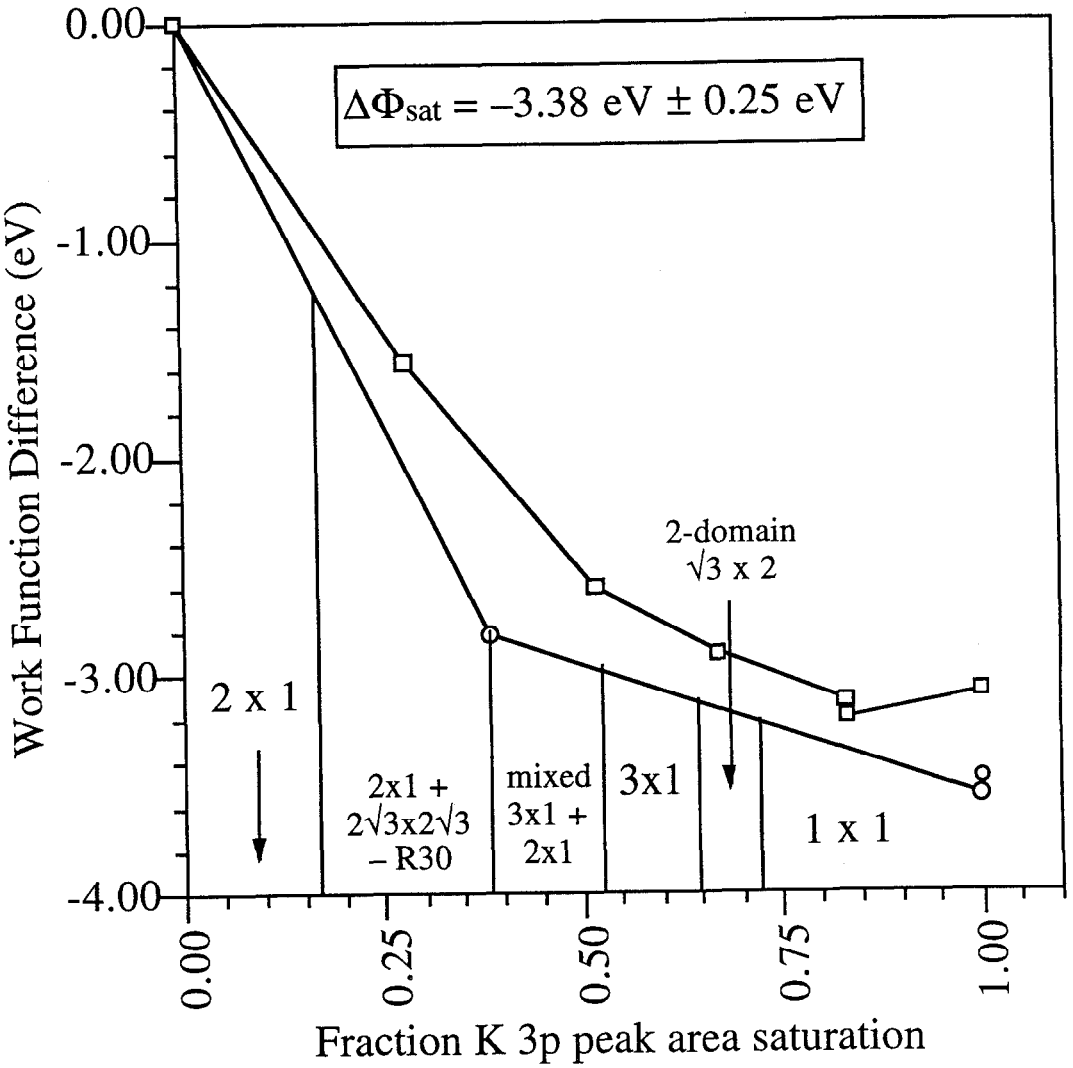

Figure 4.3(a)-(b). Photographs of the LEED patterns for the RT-dosed cleaved K/Si(111) surface with increasing K coverage. (a) Clean 2x1. (b) 2x1 + $2\sqrt{3}$ x$2\sqrt{3}$ –R30°. The incident electron beam energy is approximately 100 eV for all the photographs. The vertical axis is along the $[\bar{1}10]$ direction, and the horizontal is along $[11\bar{2}]$.

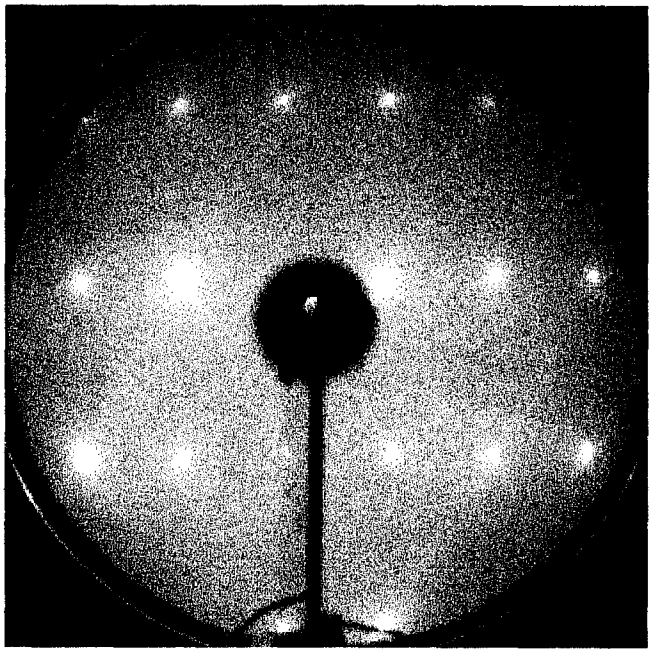

(a) 2x1

0% to 17% of K 3p
area saturation
Beam energy 79.2 eV

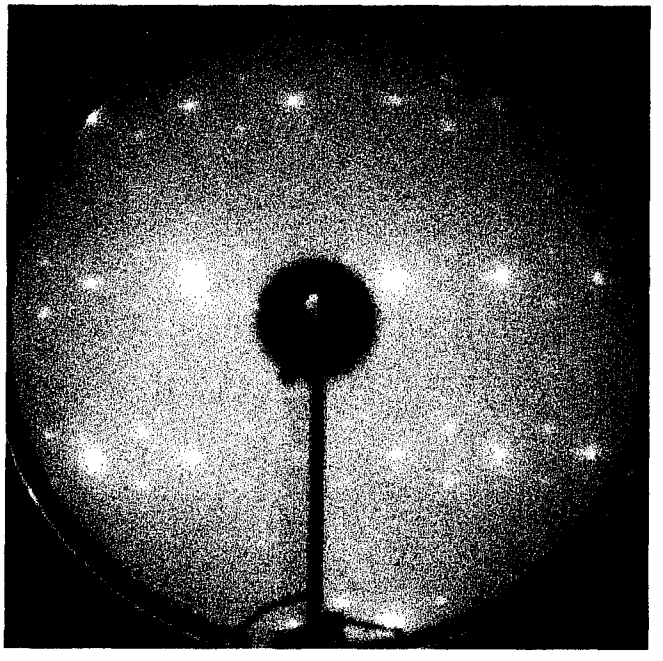

(b) 2x1 + 2√3 x 2√3 – R30

17% to 39% of K 3p
area saturation
Beam energy 78.6 eV

Figure 4.3(c)-(d). Photographs of the LEED patterns for the RT-dosed cleaved K/Si(111) surface with increasing K coverage (c) Mixed 2x1 + 3x1. (d) Single-domain 3x1. The incident electron beam energy is approximately 100 eV for all the photographs. The vertical axis is along the $[\bar{1}10]$ direction, and the horizontal is along $[11\bar{2}]$.

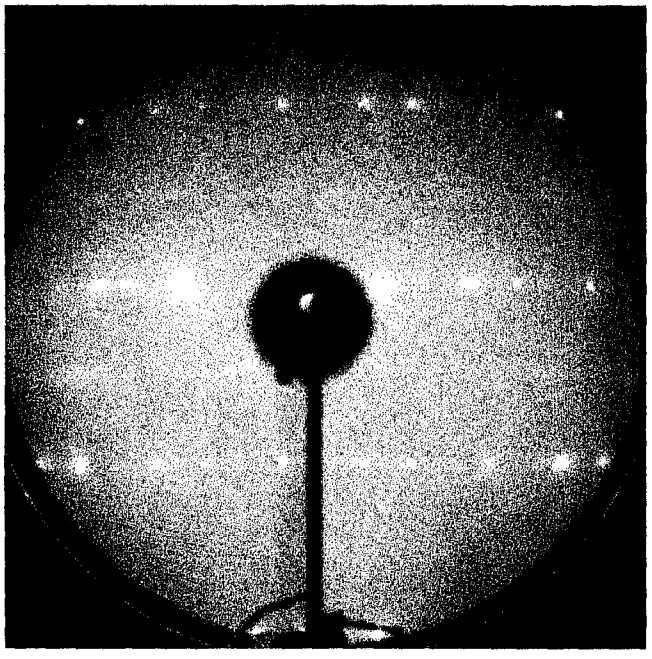

(c) Mixed 2x1 + 3x1
39% to 53% of K 3p
area saturation
Beam energy 78.4 eV

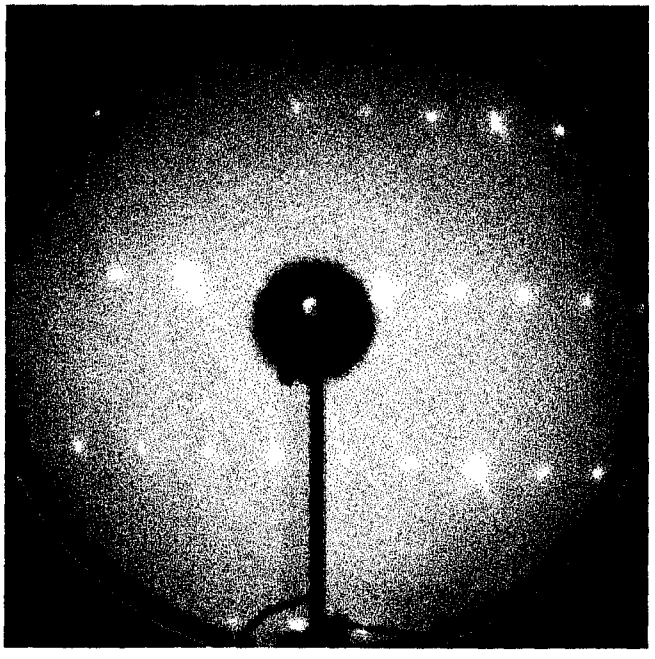

(d) 3x1
53% to 65% of K 3p
area saturation
Beam energy 80.9 eV

Figure 4.3(e)-(f). Photographs of the LEED patterns for the RT-dosed cleaved K/Si(111) surface with increasing K coverage. (e) Two-domain $\sqrt{3}$ x2. (f) 1x1 (pattern at saturation coverage, Θ = 1 ML). The incident electron beam energy is approximately 100 eV for all the photographs. The vertical axis is along the $[\bar{1}10]$ direction, and the horizontal is along $[11\bar{2}]$.

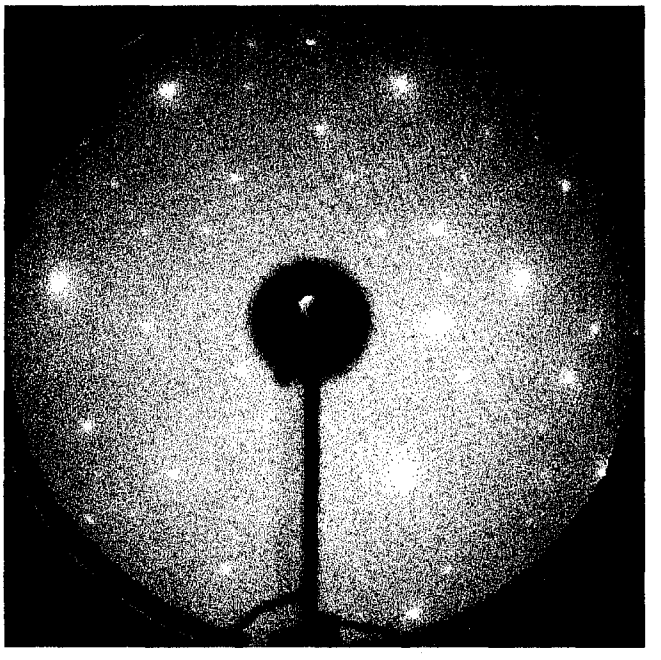

(e) 2-domain $\sqrt{3}$ x 2
65% to 72% of K 3p
area saturation
Beam energy 68.7 eV

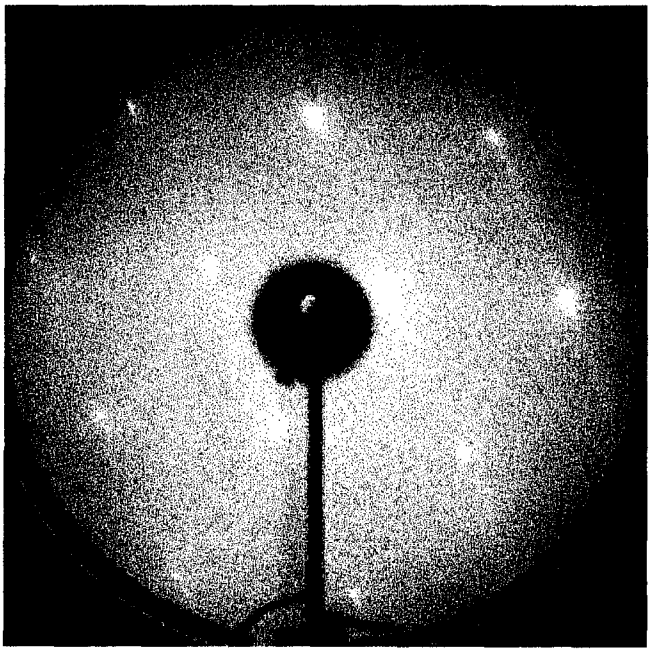

(f) 1 x 1
72% to 100% of K 3p
area saturation
Beam energy 100.1 eV

Figure 4.4. Photograph of the 3-domain 3x1 LEED pattern on the annealed cleaved K/Si(111) surface. Incident electron beam energy is 79.4 eV.

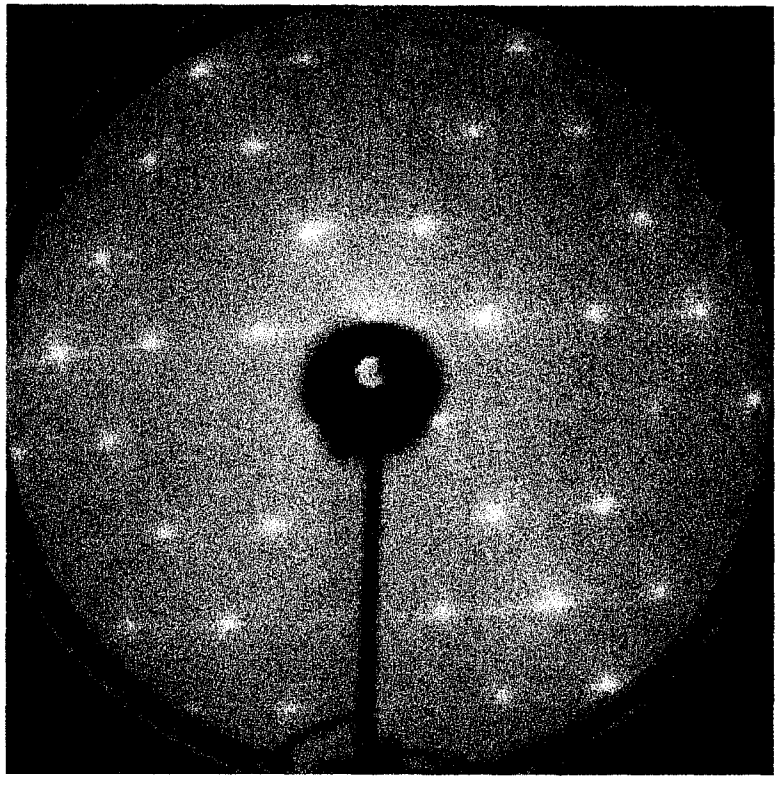

Figure 4.5(a). Tentative model of the (a) 2x1 + $2\sqrt{3}$x$2\sqrt{3}$–R30° K/Si(111) surface, in the (111) plane top view. The largest dark circles represent the K atoms, all other atoms are Si. Both models include a π-bonded 2x1 Si chain, with K adatoms bonding to Si chain atoms. Coverage is 1/3 ML K; K adatoms can be removed from either unit cell to reduce K coverage while maintaining the LEED pattern.

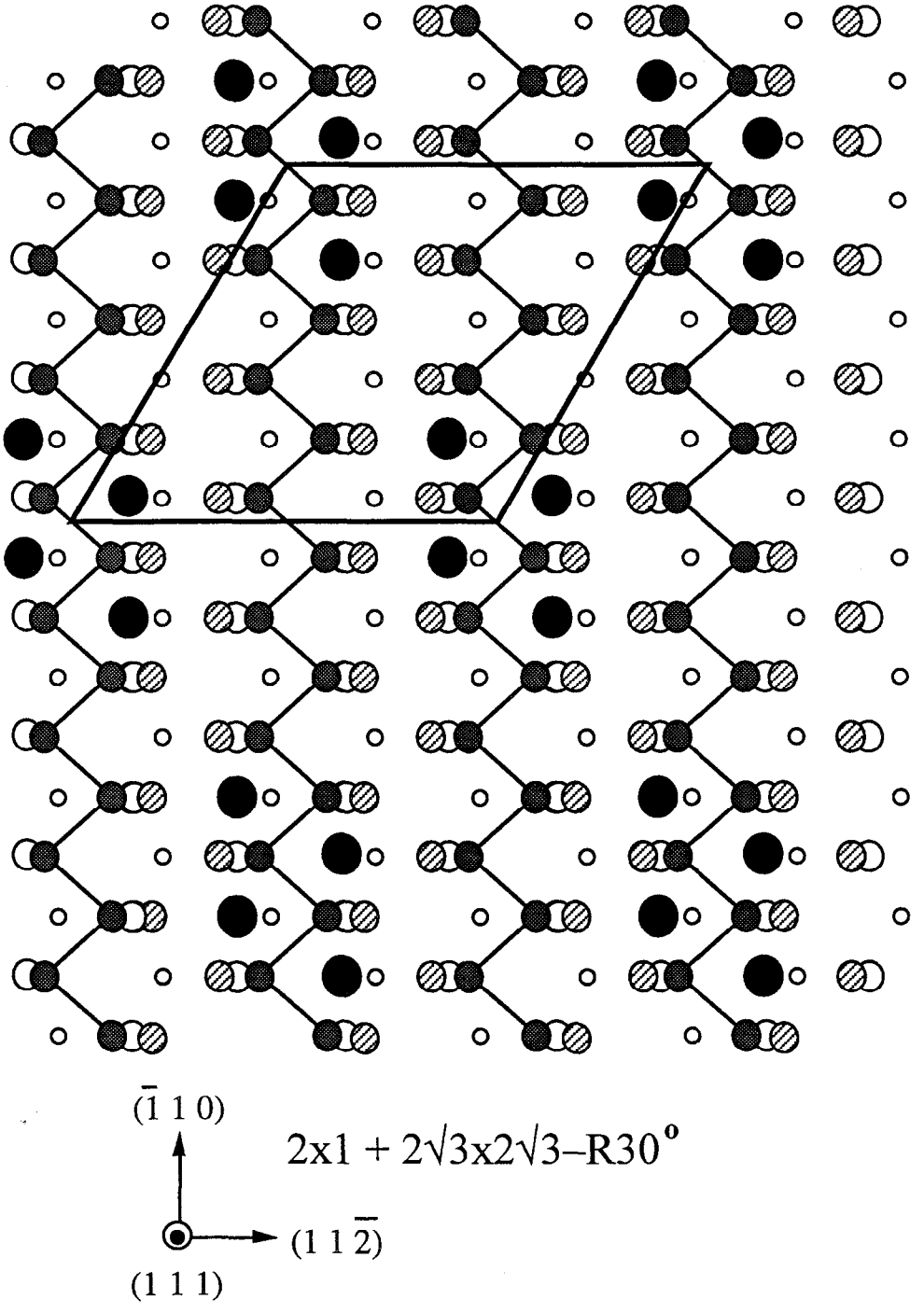

Figure 4.5(b). Tentative model of the (b) $\sqrt{3}$x2 K/Si(111) surface, in the (111) plane top view. The largest dark circles represent the K atoms, all other atoms are Si. Both models include a π-bonded 2x1 Si chain, with K adatoms bonding to Si chain atoms. Coverage is 3/4 ML ; K adatoms can be removed from either unit cell to reduce K coverage while maintaining the LEED pattern.

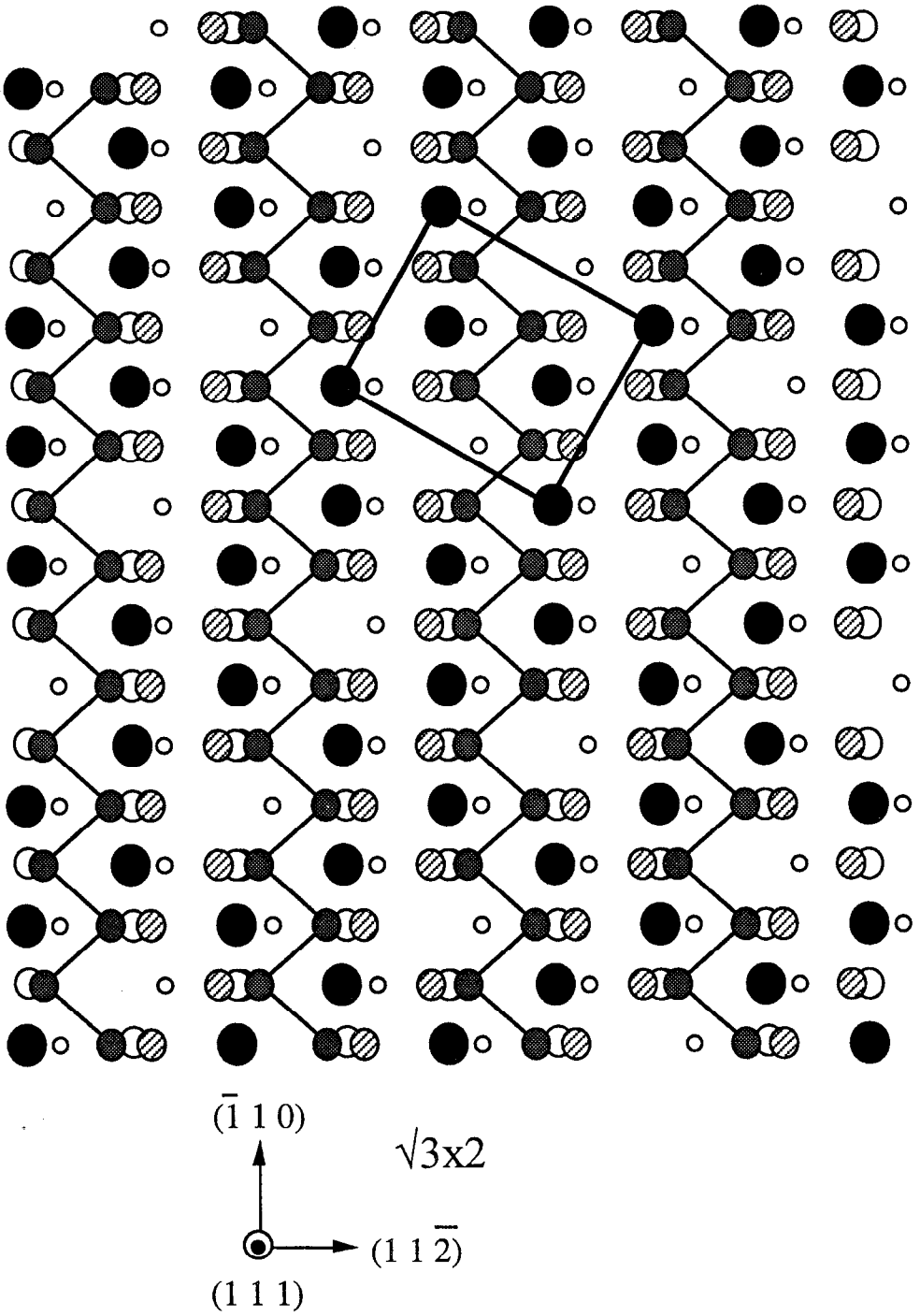

Figure 4.6. K 3p photoemission spectra, K/Si(111) room-temperature dosing progression. Photon energy 65 eV.

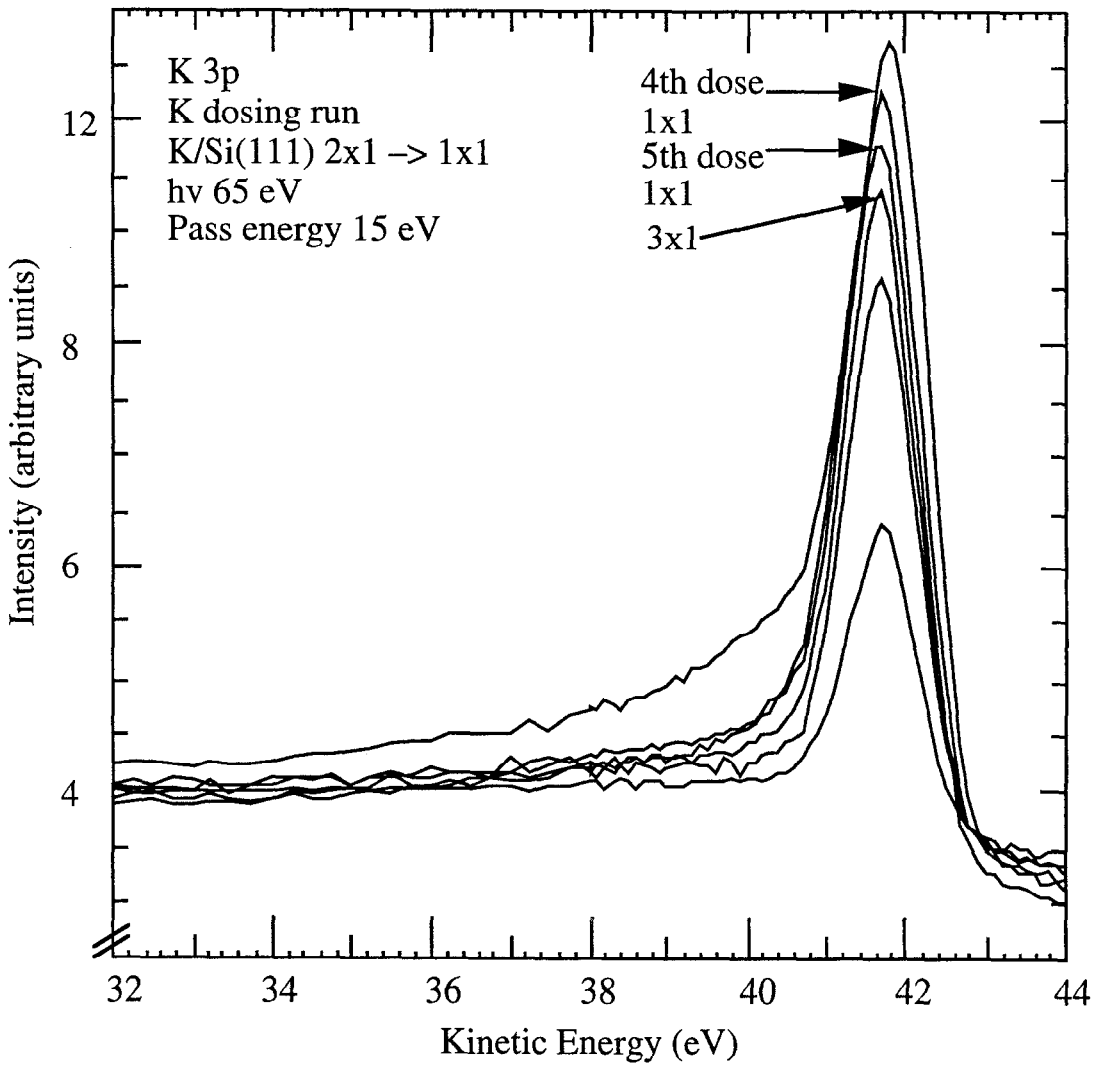

Figure 4.7. Surface-sensitive Si 2p photoemission spectra, K/Si(111) room-temperature dosing progression. Photon energy 145 eV.

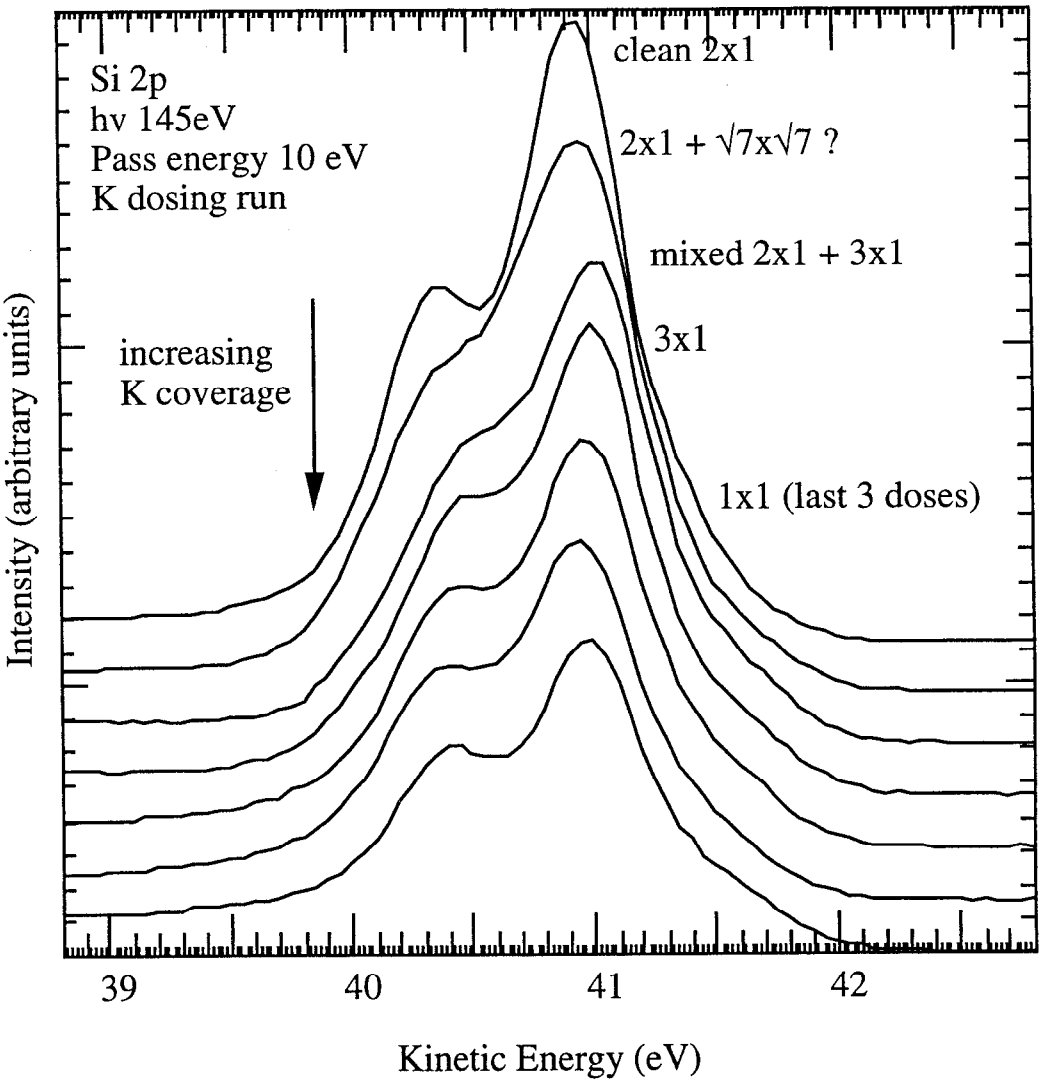

Figure 4.8(a). Valence band region photoemission spectra, K/Si(111) room-temperature dosing progression (a) overlay (b) stack. Photon energy 65 eV.

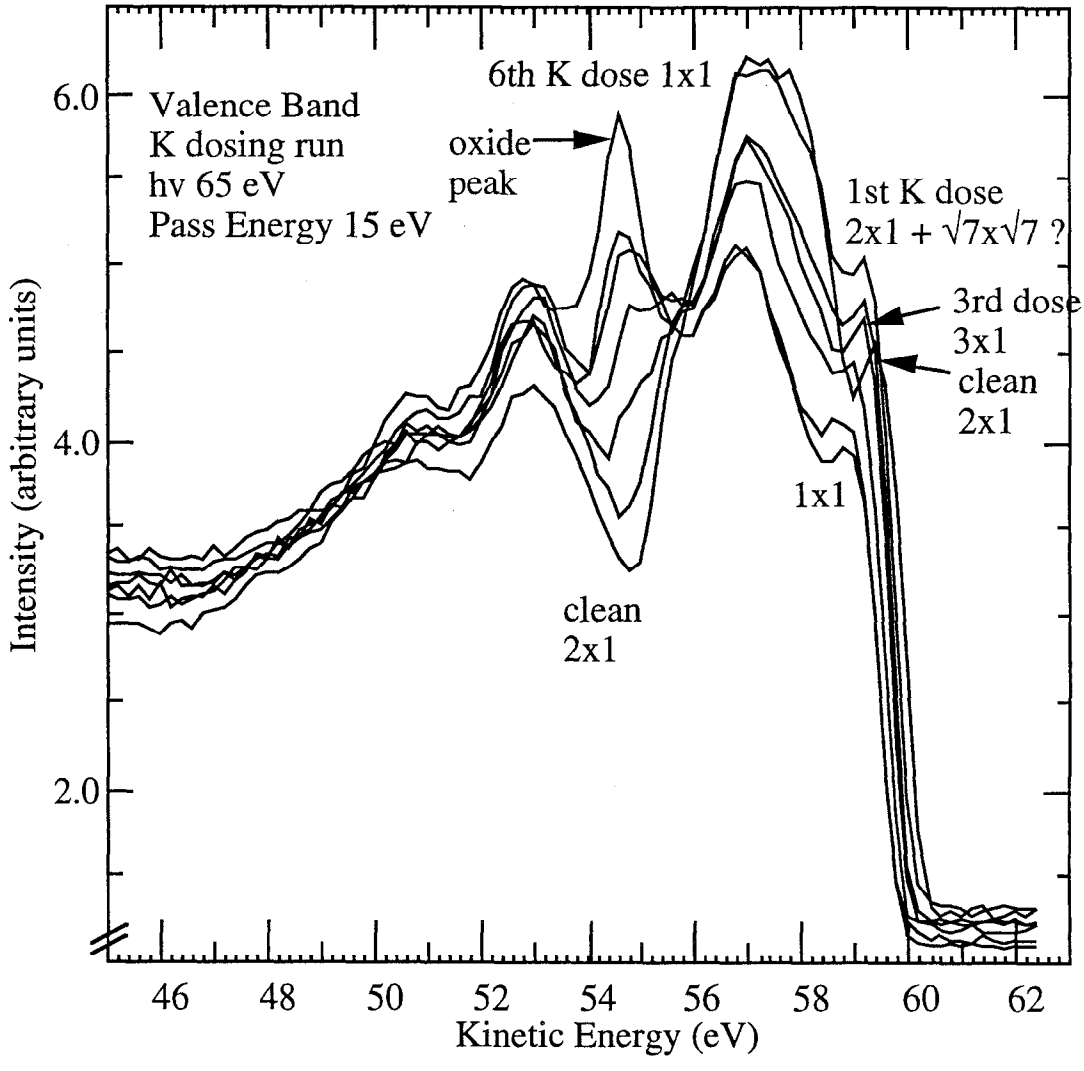

Figure 4.8(b). Valence band region photoemission spectra, K/Si(111) room-temperature dosing progression (a) overlay (b) stack. Photon energy 65 eV.

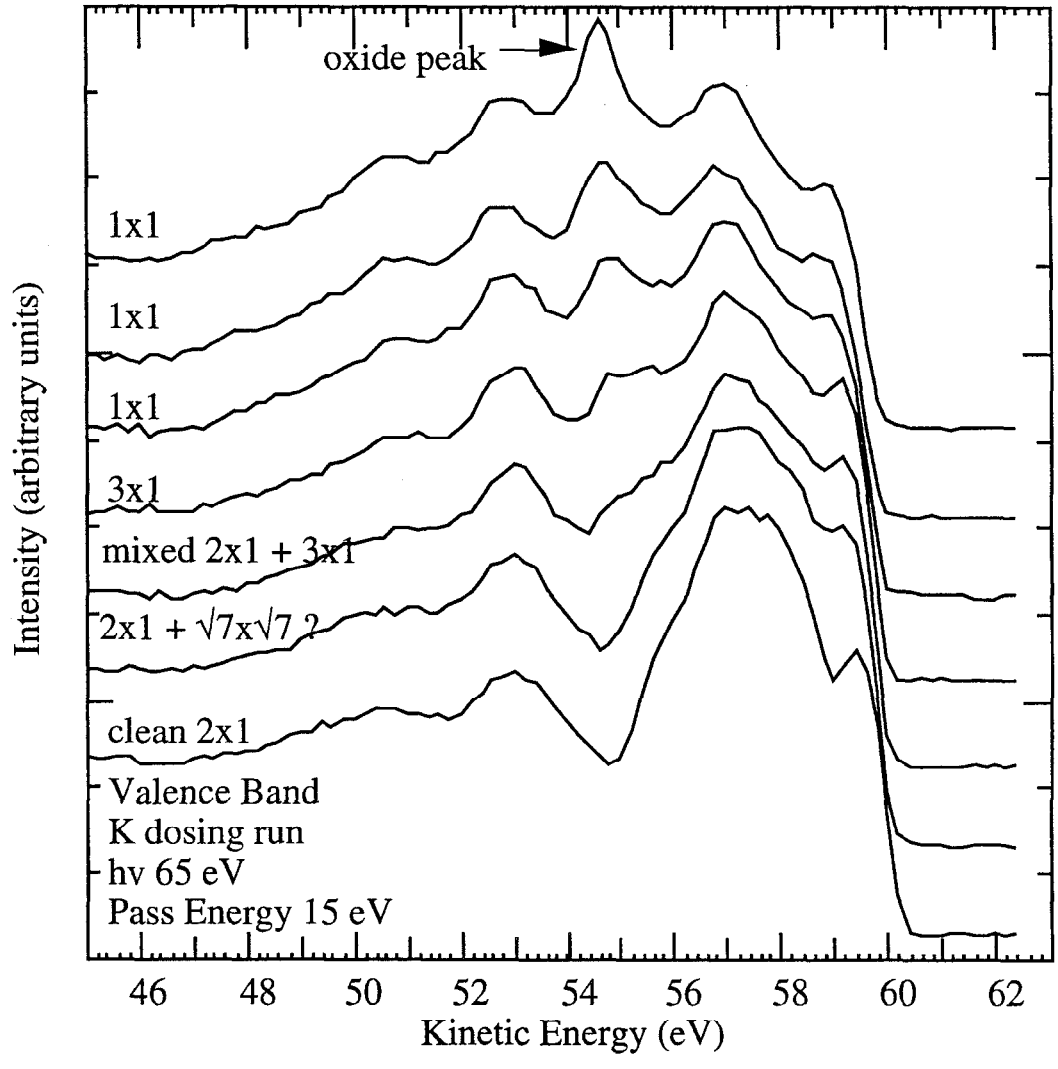

Figure 4.9. Effect of oxidation upon valence band spectra. The spectra with the largest oxide peak was taken after the final dose of a room-temperature dosing progression for K/Si(111), while the other 3 spectra show the growth of the oxide peak over time for another sample. Photon energy 65 eV.

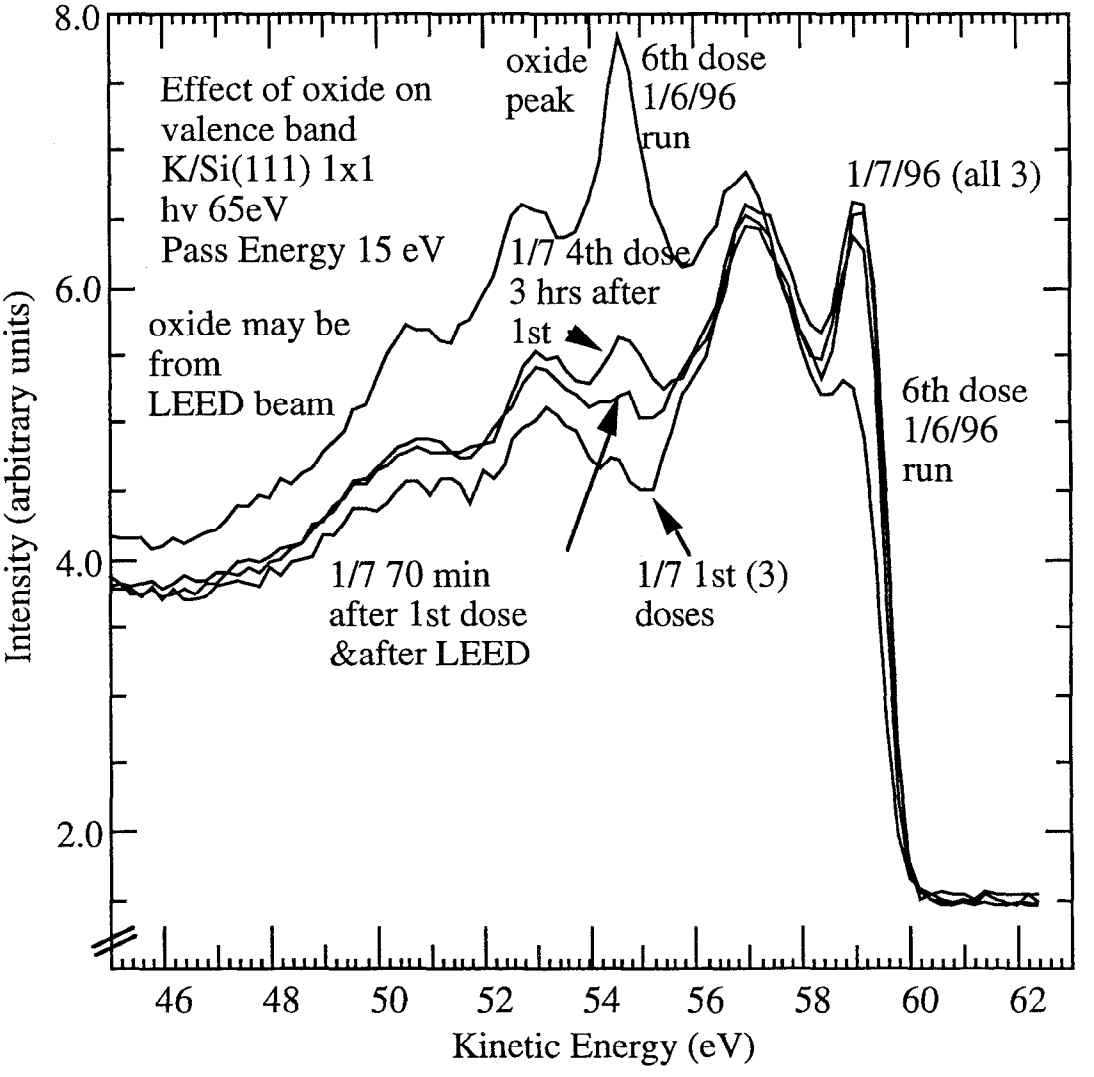

Figure 4.10. Valence band region photoemission spectra, clean 2x1 vs. K/Si 1x1 for three samples. Note how the size of the surface state in the K/Si(111)1x1 spectra depends on the size of the initial clean Si(111)2x1 surface state. Photon energy 65 eV.

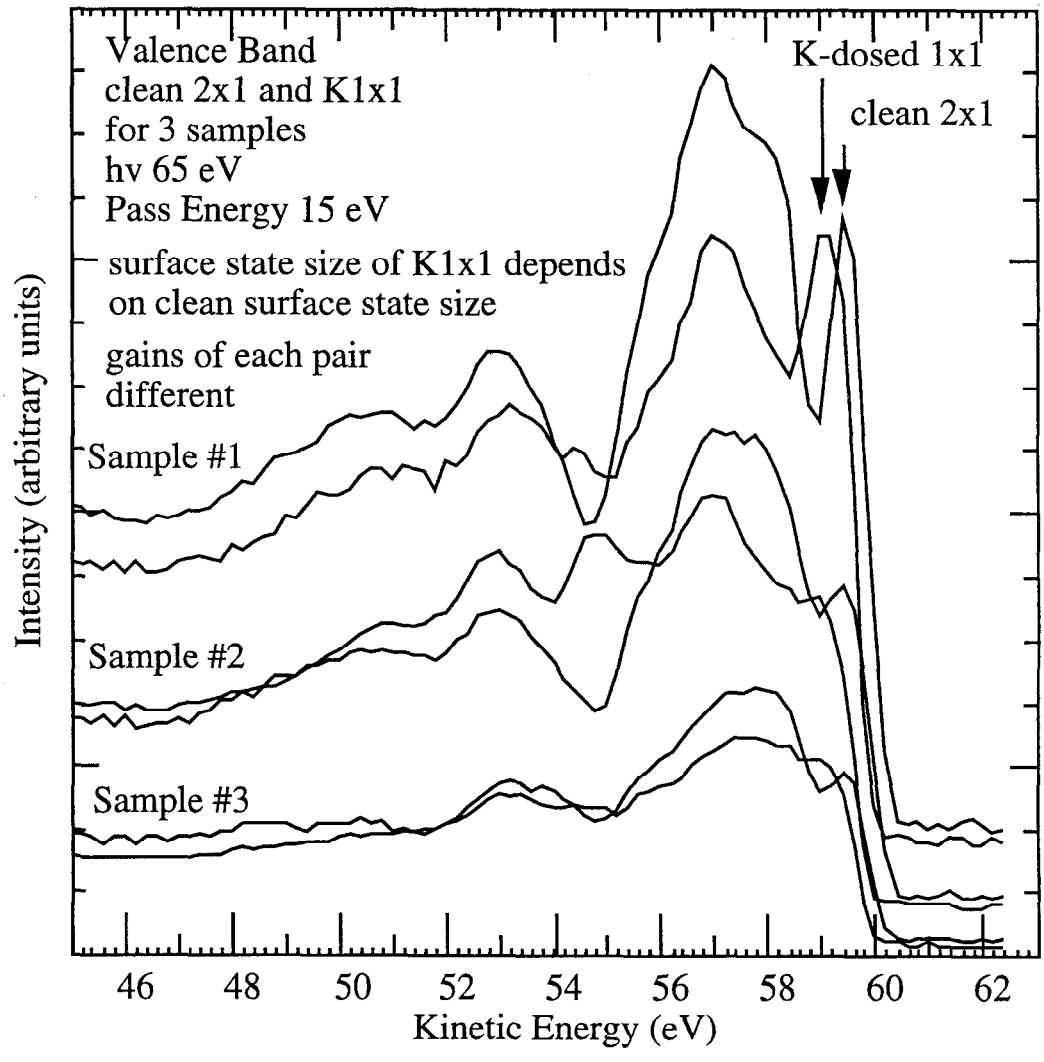

Figure 4.11(a). K 3p photoemission spectra, annealed K/Si(111)3x1 (a) annealed 3x1 vs. low coverage room-temperature dosed samples. Photon energy 65 eV.

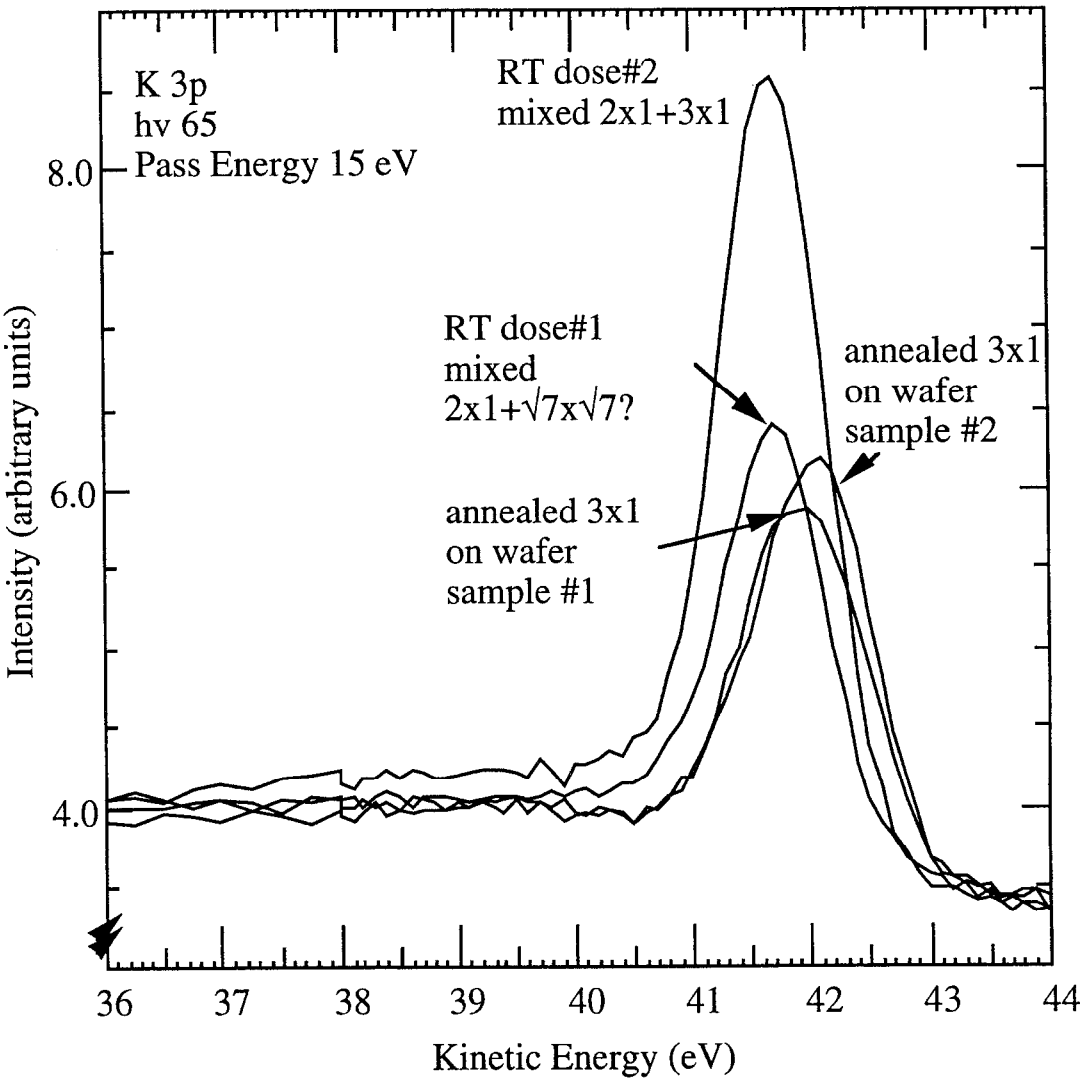

Figure 4.11(b). K 3p photoemission spectra, annealed K/Si(111)3x1 (b) coverage before and after annealing. Photon energy 65 eV.

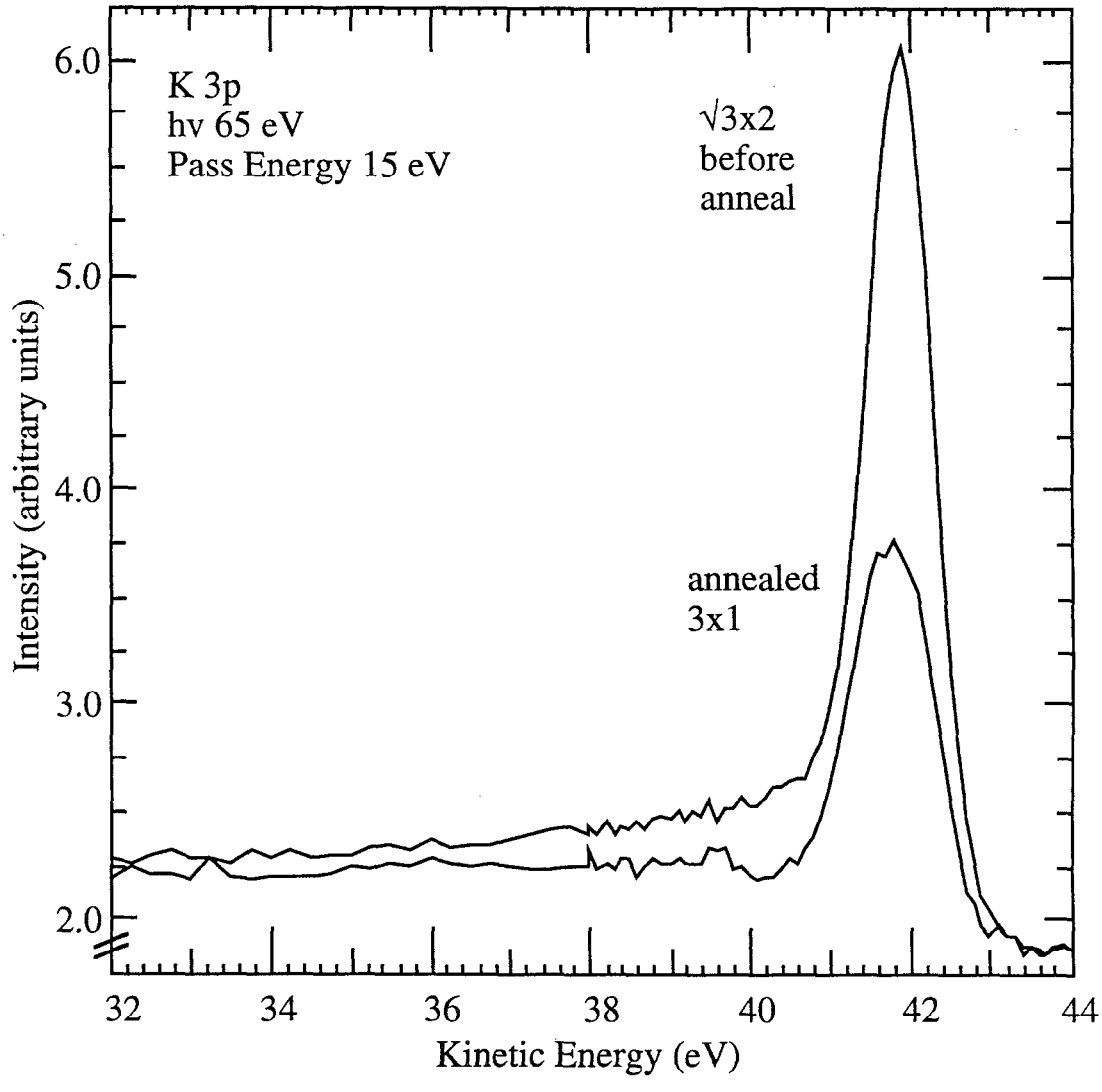

Figure 4.12. Surface-sensitive Si 2p photoemission spectra. Annealed K/Si(111)3x1 versus clean Si(111) spectra for the cleavable and wafer interfaces. Photon energy 145 eV.

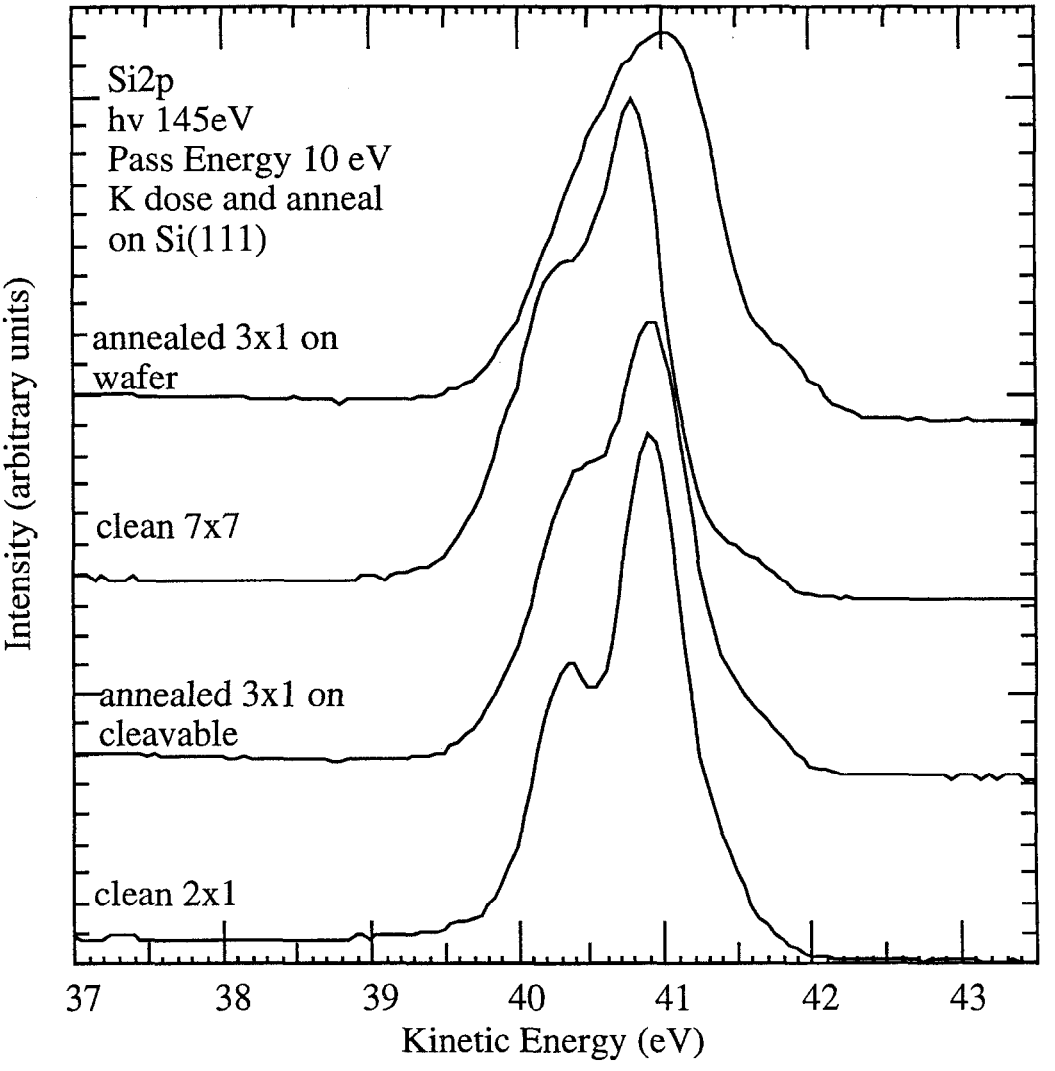

Figure 4.13. Valence band region photoemission spectra, annealed K/Si(111)3x1 and clean Si(111) spectra. Comparison of 3x1 on wafer and cleavable Si(111). Photon energy 65 eV.

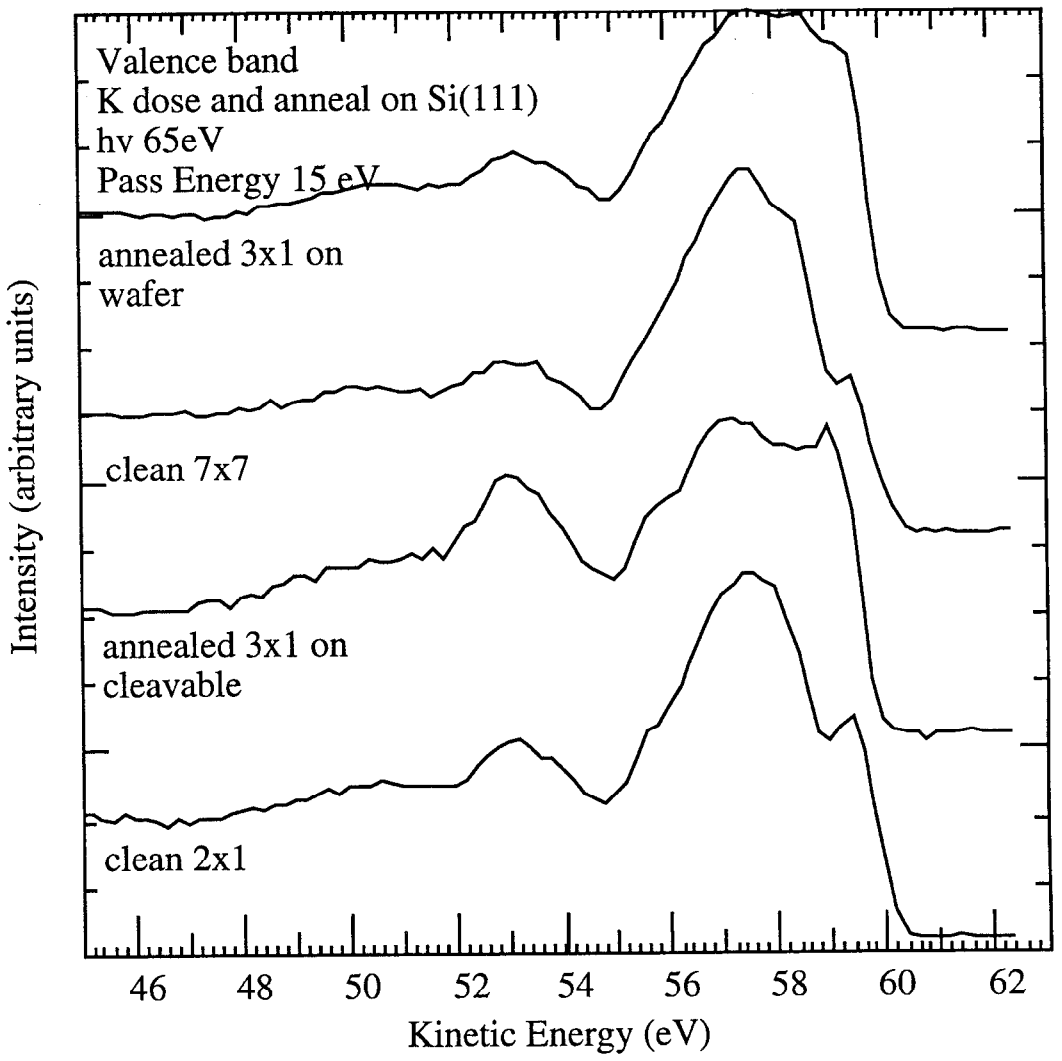

Figure 4.14. Work function difference (relative to the clean Si(111)2x1 surface) for the Cs/Si(111) interface as a function of Cs coverage, as determined by fraction of Cs 4d peak area saturation. Approximate ranges of observed LEED patterns are indicated.

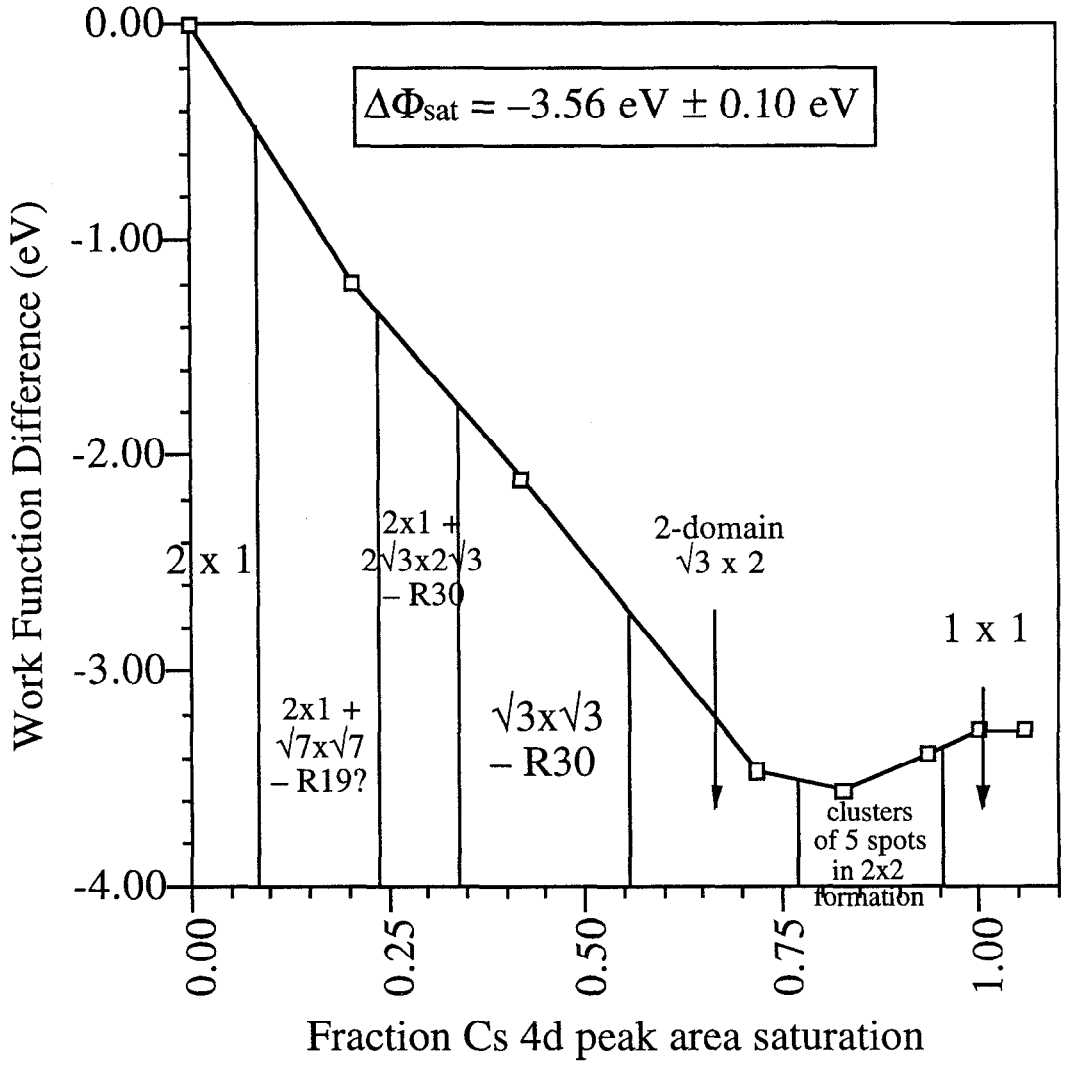

Figure 4.15(a)-(b). LEED photographs, Cs/Si(111) room-temperature dosing progression. (a) clean 2x1 surface (b) 2x1 + $\sqrt{7}$x$\sqrt{7}$–R19°?

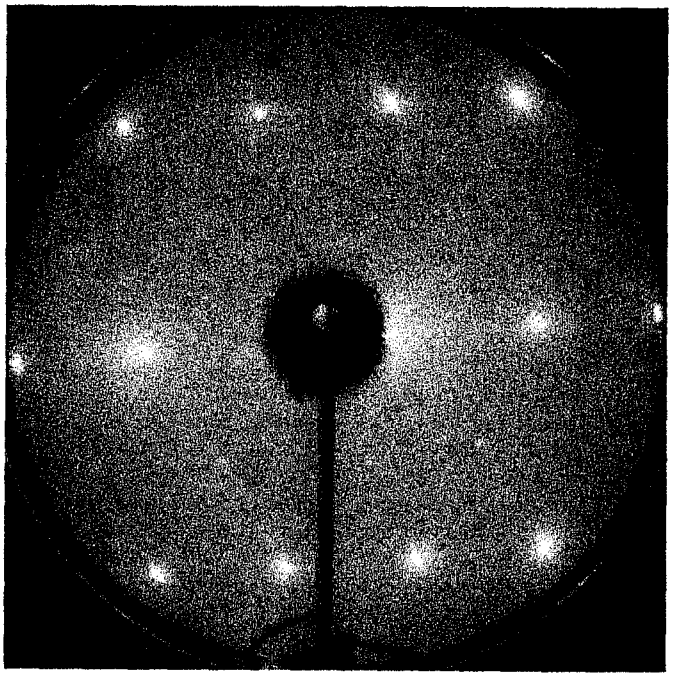

(a) 2 x 1
0% of Cs 3d area
saturation
Beam energy 47.0 eV

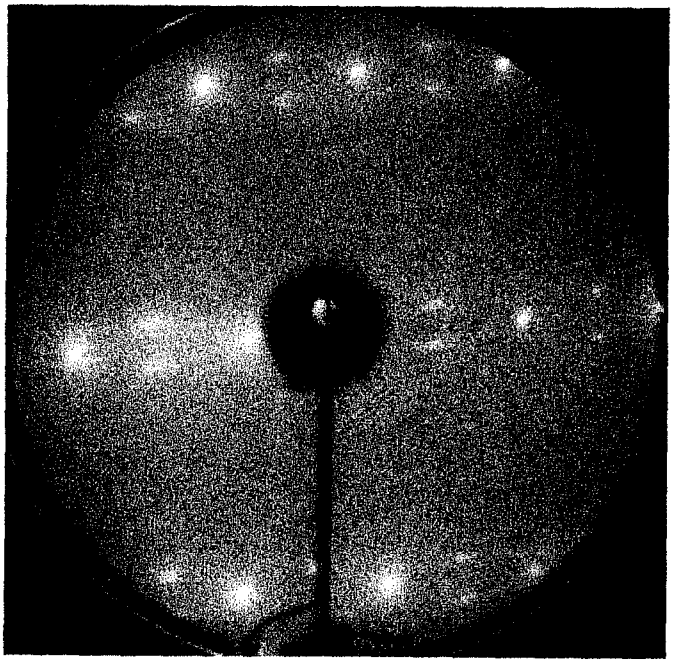

(b) 2 x 1 + $\sqrt{7}$ x $\sqrt{7}$ – R 19?
18% of Cs 3d area
saturation
Beam energy 36.9 eV

Figure 4.15(c)-(d). LEED photographs, Cs/Si(111) room-temperature dosing progression. (c) 2x1 + $2\sqrt{3}$x$2\sqrt{3}$–R30° (d) 2x1 + $\sqrt{3}$x$\sqrt{3}$–R30°

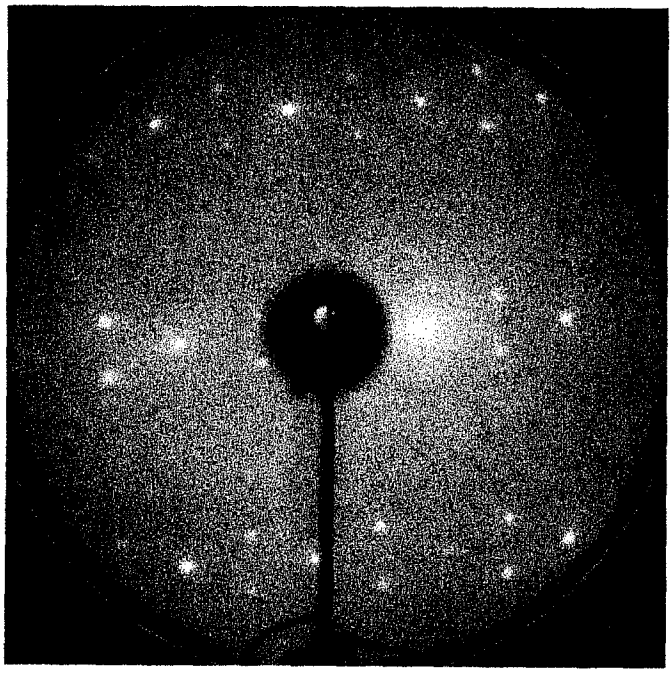

(c) 2x1 + 2√3 x 2√3 – R30
27% of Cs 3d area saturation
Beam energy 50.1 eV

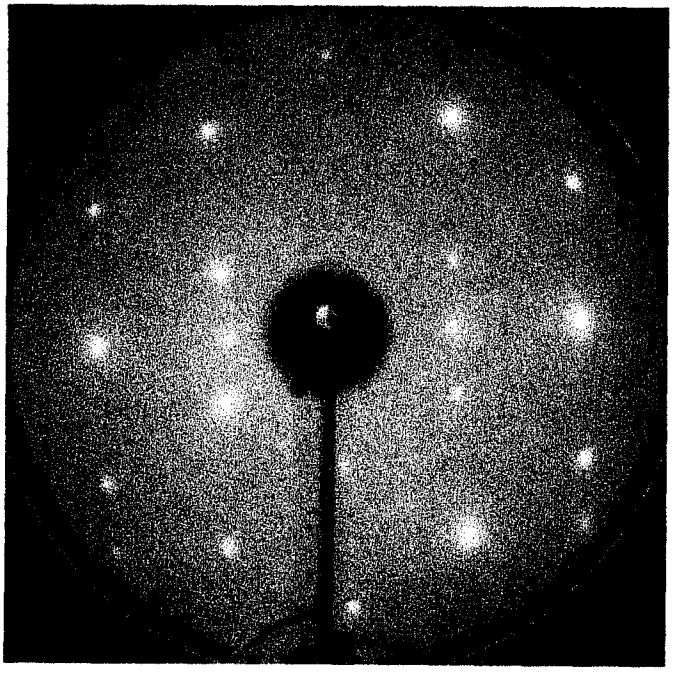

(d) 2x1 + √3 x √3 – R30
47% of Cs 3d area saturation
Beam energy 57.6 eV

Figure 4.15(e)-(f). LEED photographs, Cs/Si(111) room-temperature dosing progression. (e) $\sqrt{3}x\sqrt{3}$–R30° (f) 2-domain $\sqrt{3}x2$

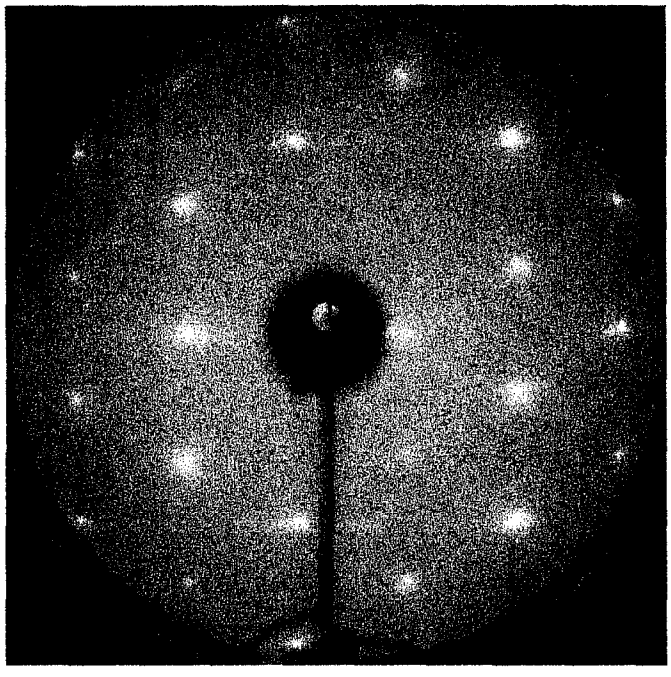

(e) $\sqrt{3}$ x $\sqrt{3}$ – R30
~ 65% of Cs 3d area saturation
Beam energy 68.0 eV

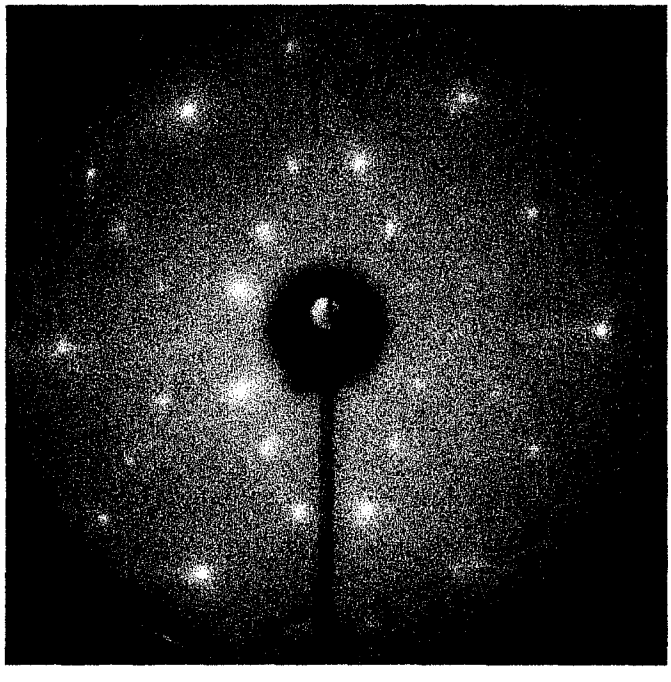

(f) 2-domain $\sqrt{3}$ x 2
~ 98% of Cs 3d area saturation
Beam energy 44.9 eV

Figure 4.15(g)-(h). LEED photographs, Cs/Si(111) room-temperature dosing progression. (g) Clusters of 5 spots in 2x2 formation (h) 1x1

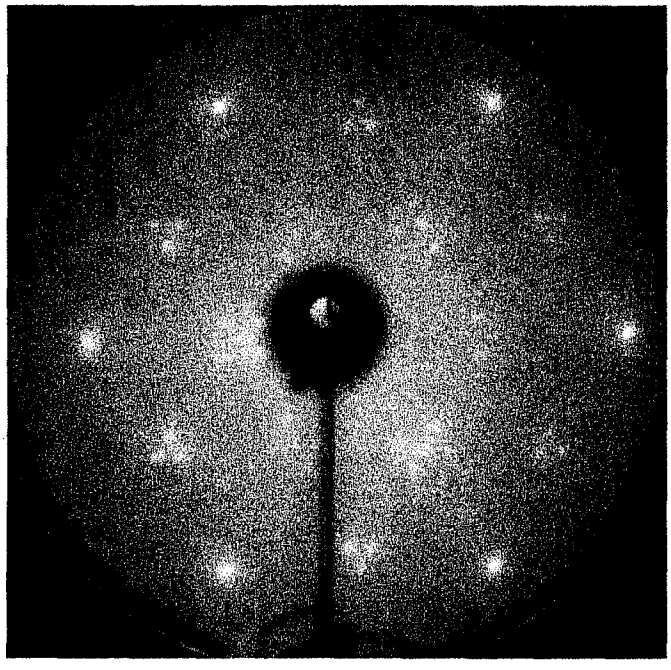

(g) Clusters of 5 spots in 2x2 formation
~ 100% of Cs 3d area saturation
Beam energy 45.3 eV

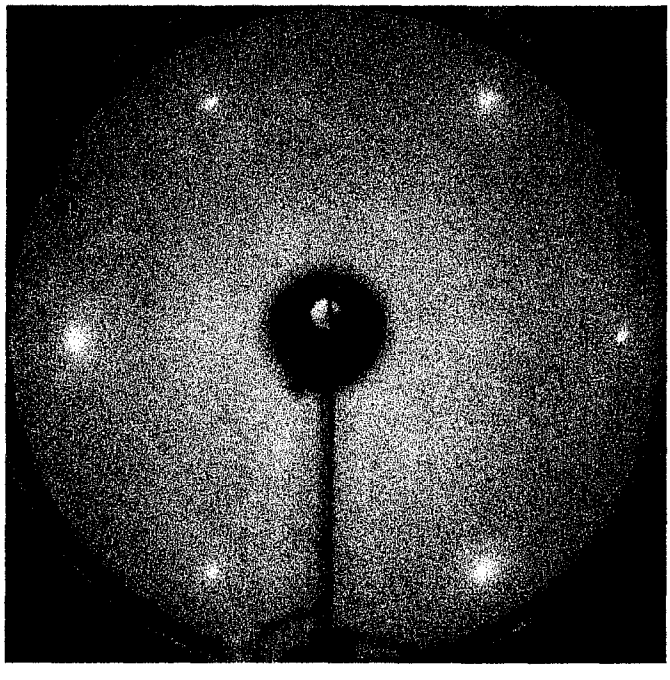

(h) 1 x 1
~ 100% of Cs 3d area saturation
Beam energy 43.7 eV

Figure 4.16(a). Cs 4d photoemission spectra, Cs/Si(111) room-temperature dosing progression (a) overlay (b) stack. Photon energy 120 eV.

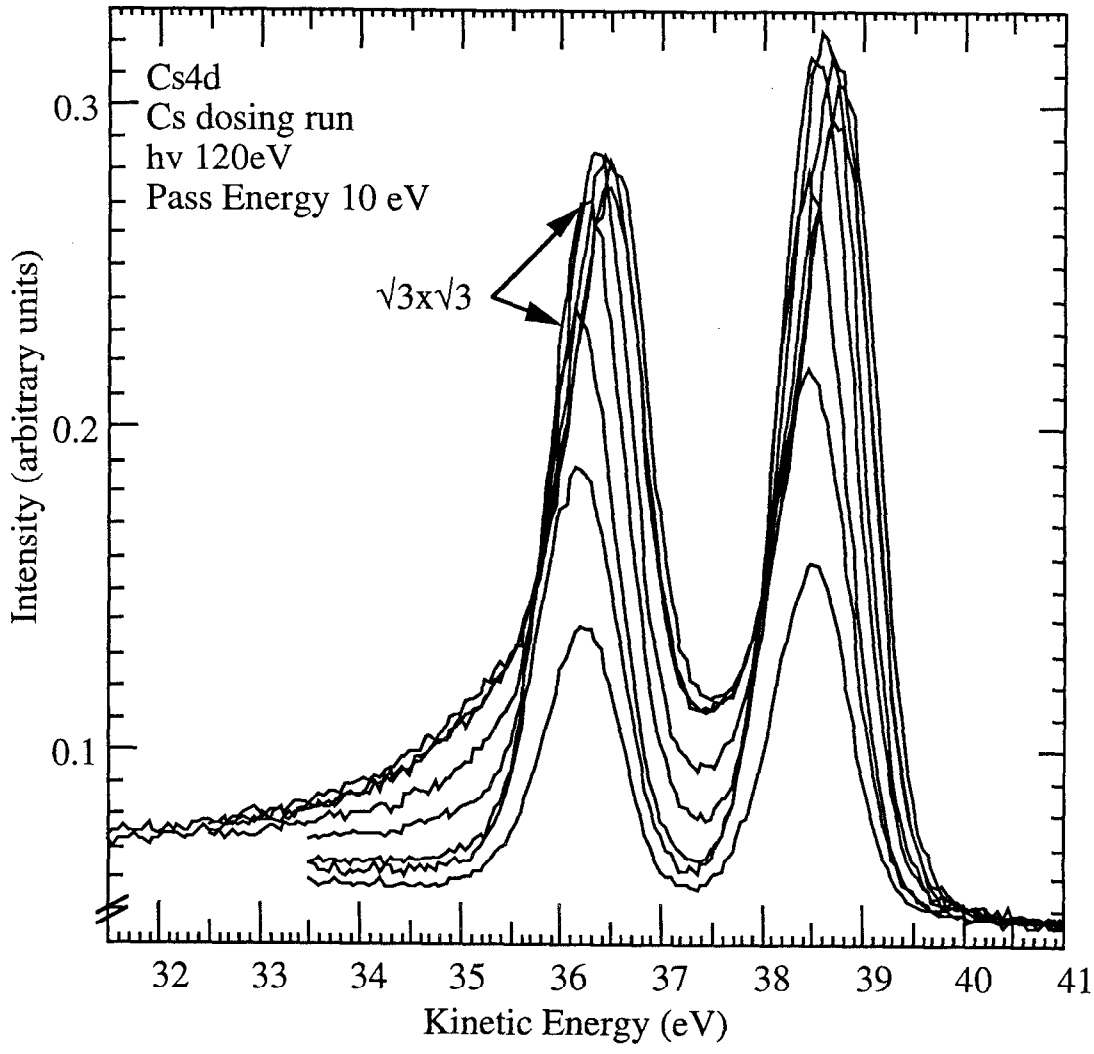

Figure 4.16(b). Cs 4d photoemission spectra, Cs/Si(111) room-temperature dosing progression (a) overlay (b) stack. Photon energy 120 eV.

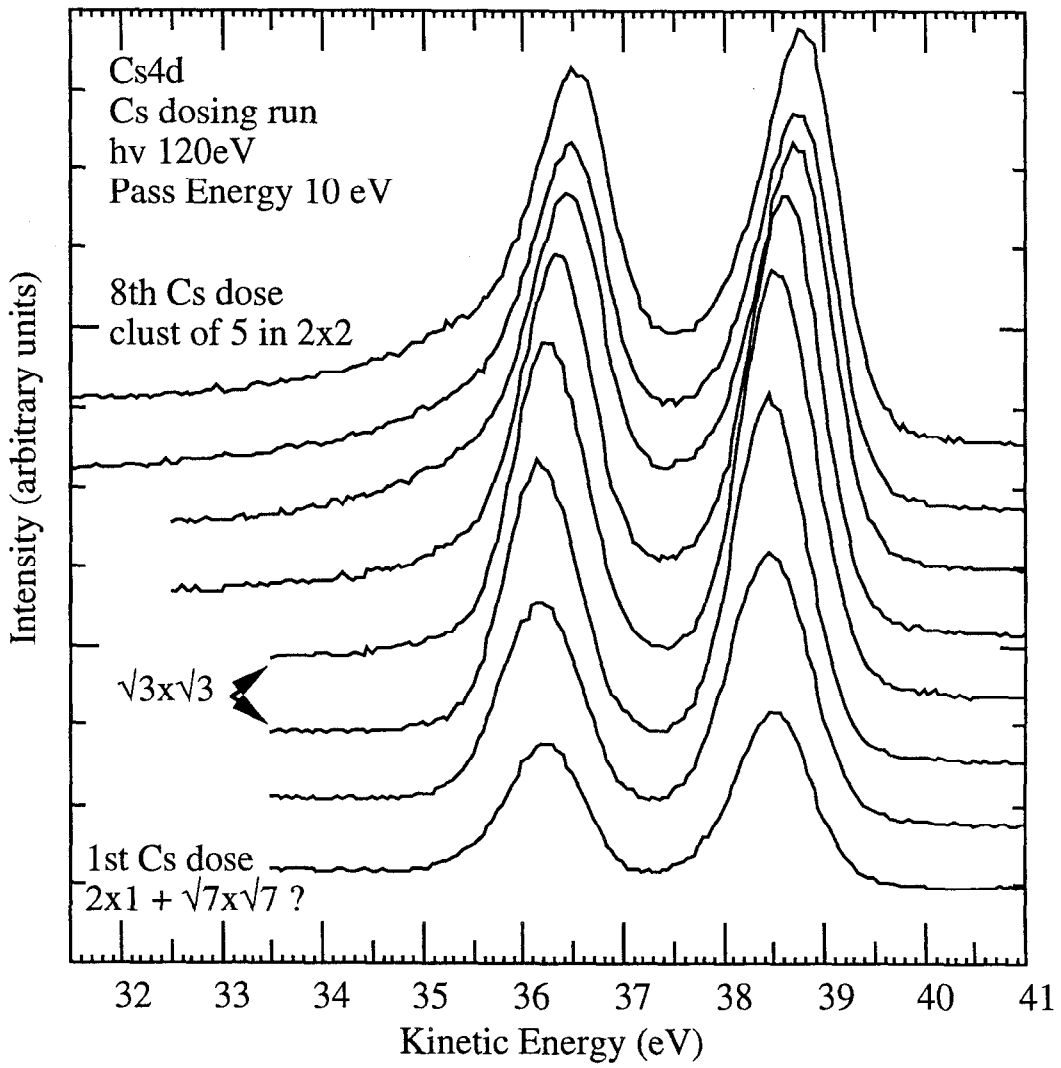

Figure 4.17. Cs 5p photoemission spectra, Cs/Si(111) room-temperature dosing progression. Photon energy 65 eV.

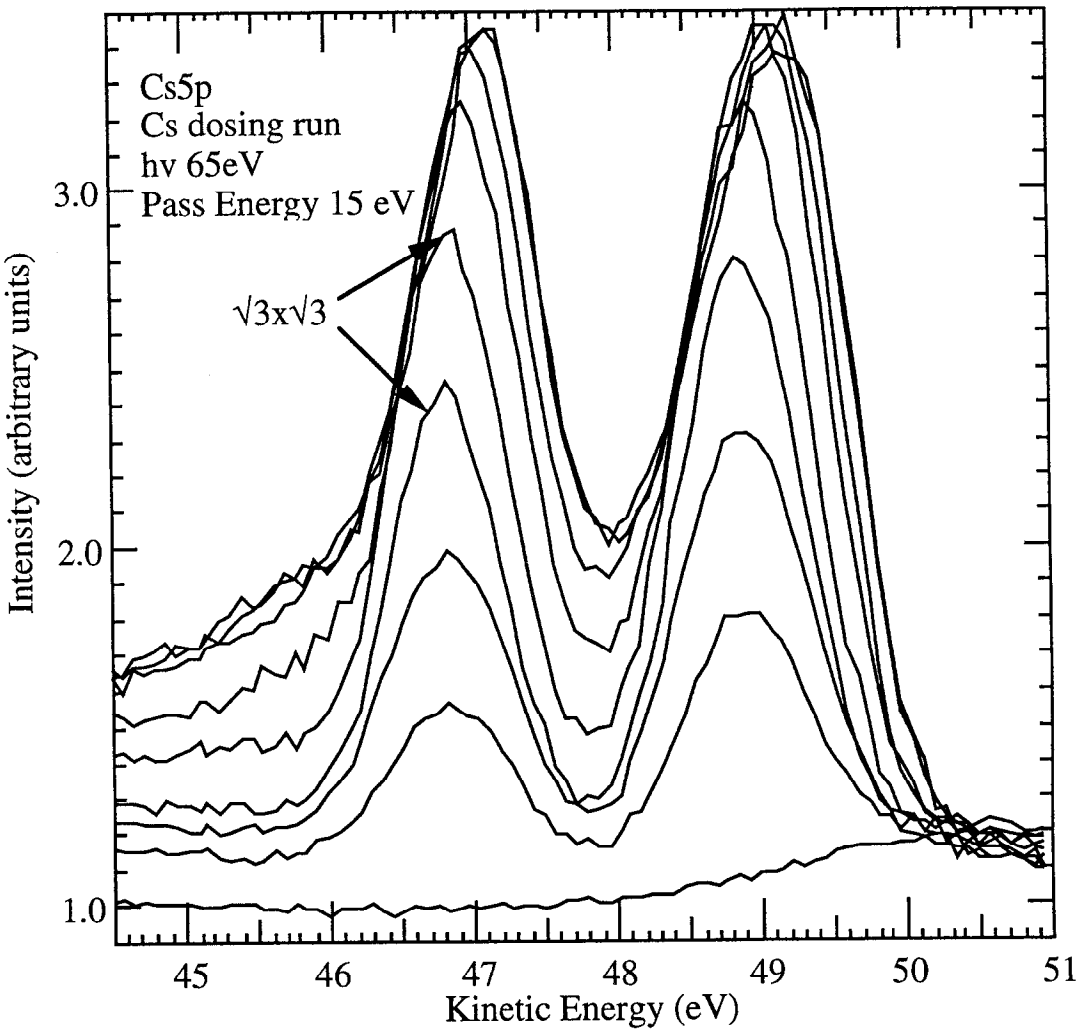

Figure 4.18(a). Surface-sensitive Si 2p photoemission spectra, Cs/Si(111) (a) room-temperature dosing progression. Photon energy 145 eV.

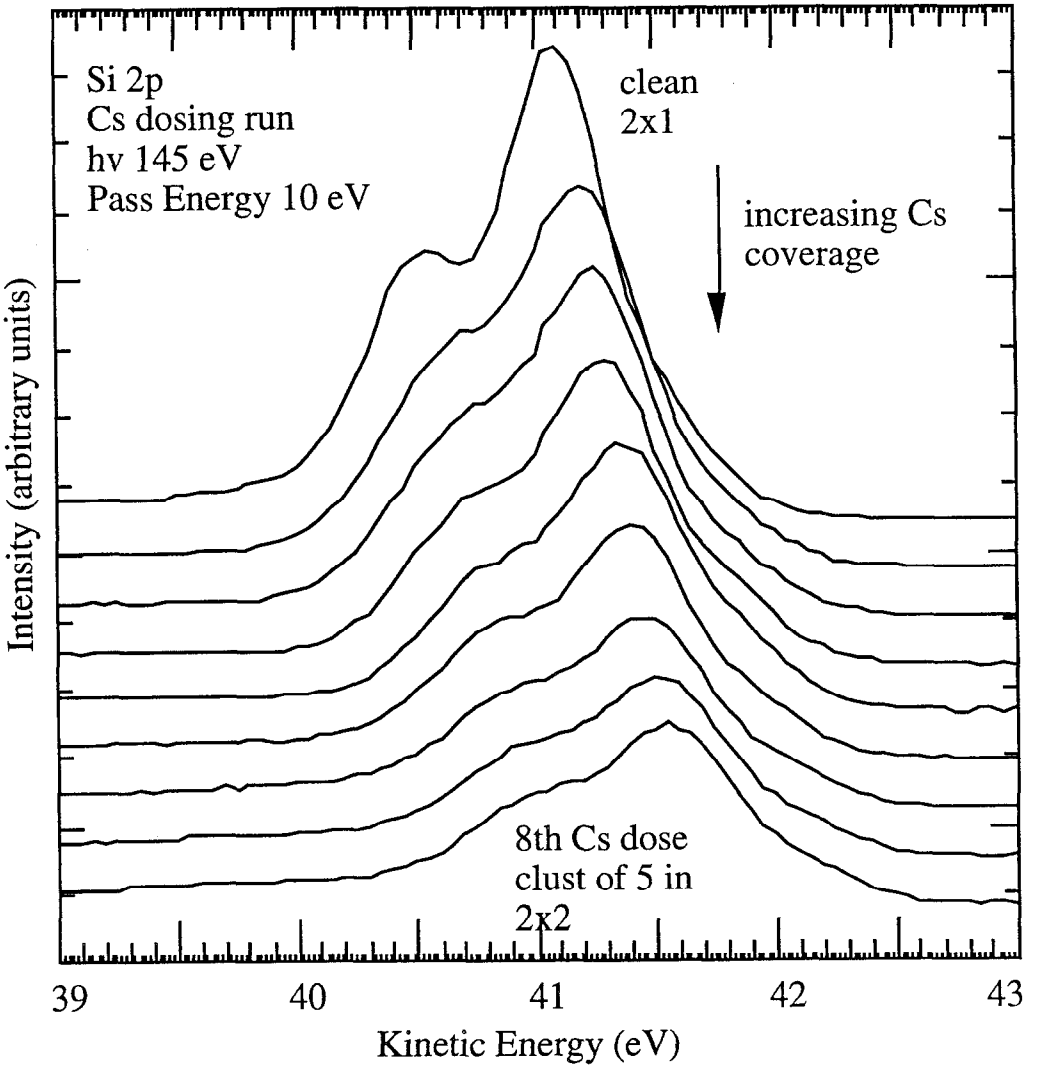

Figure 4.18(b). Surface-sensitive Si 2p photoemission spectra, Cs/Si(111) (b) loss tail seen at high coverage. Photon energy 145 eV.

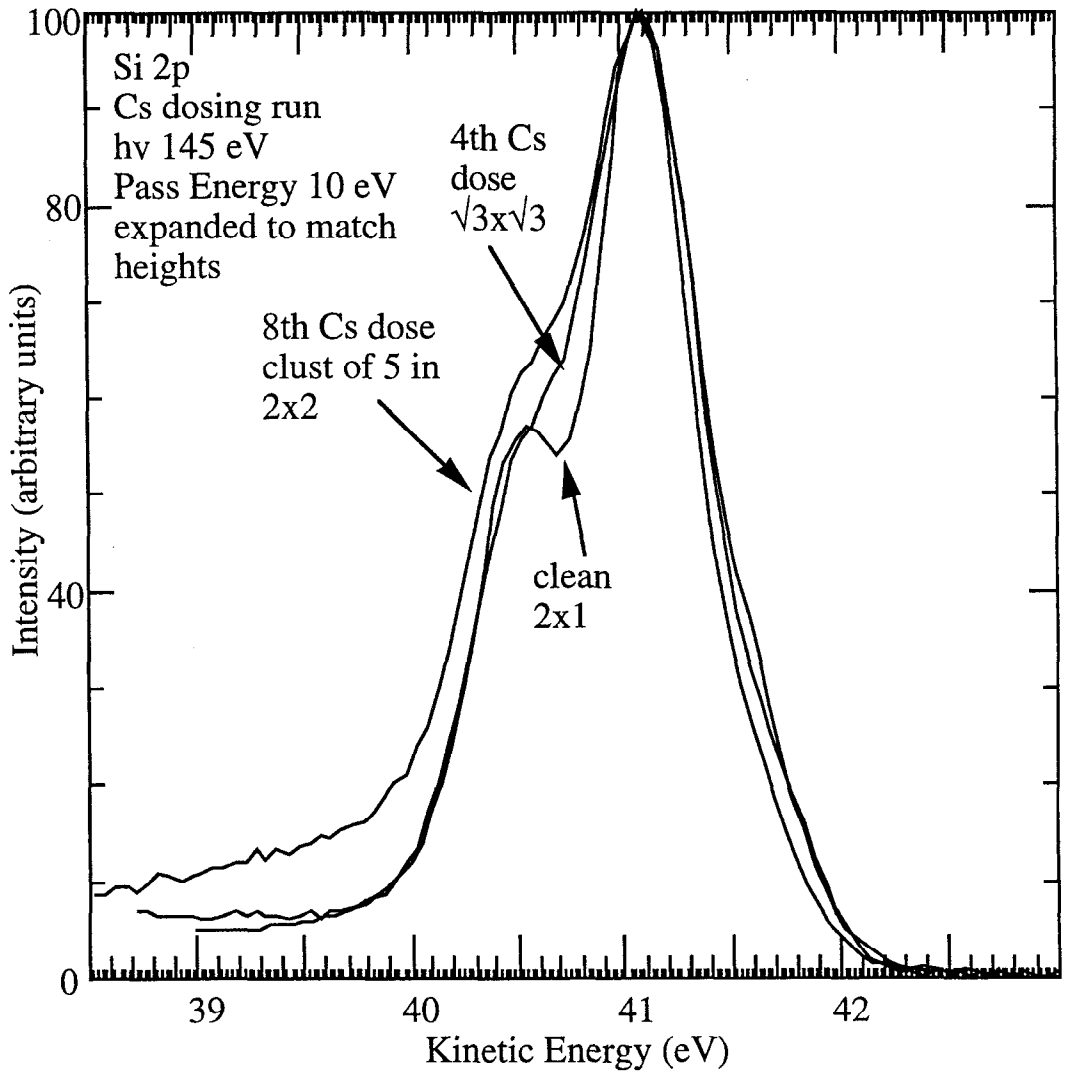

Figure 4.19. Cs 5p and Valence band region photoemission spectra, Cs/Si(111) room-temperature dosing progression. Photon energy 65 eV.

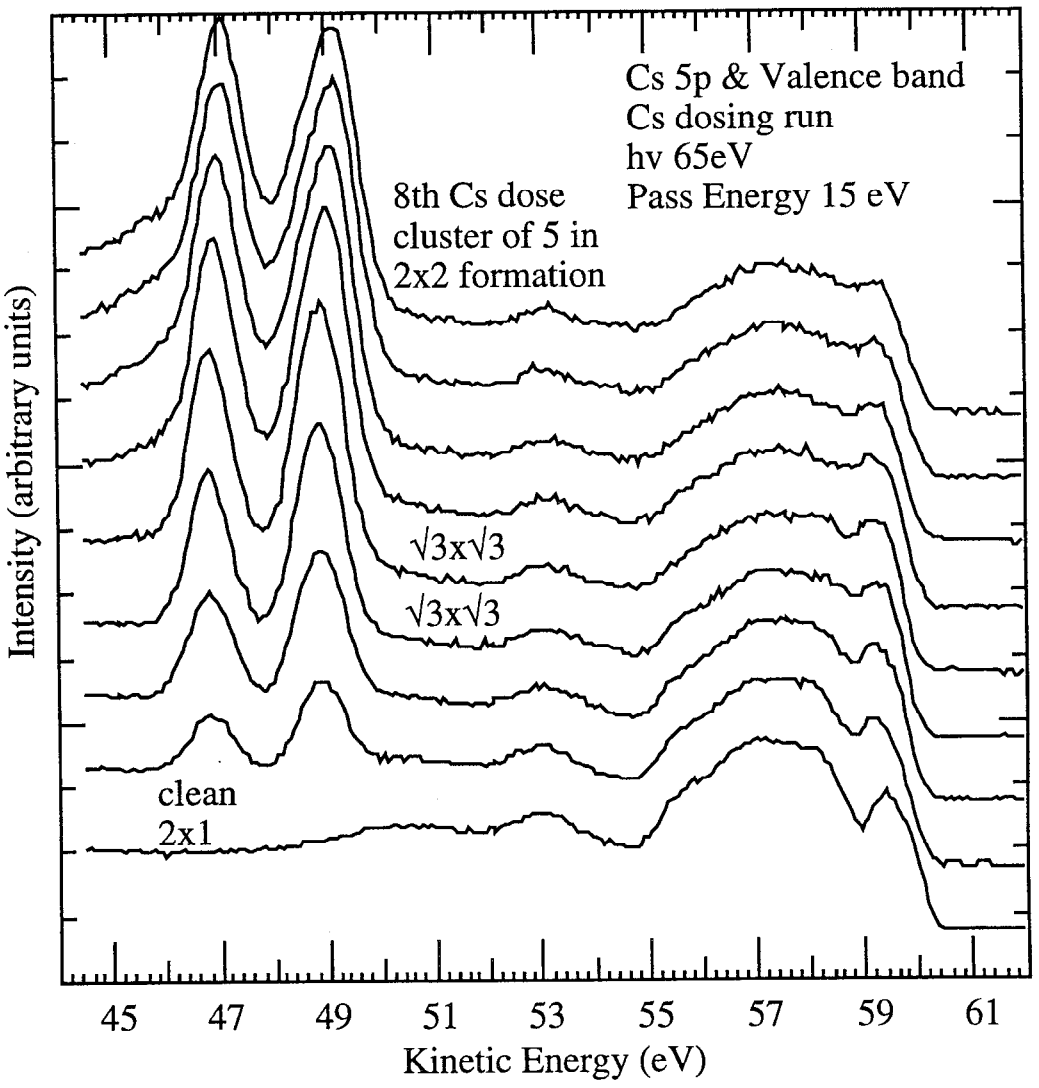

Figure 4.20(a). Valence band region photoemission spectra, Cs/Si(111) room-temperature dosing progression (a) overlay (b) stack. Photon energy 65 eV.

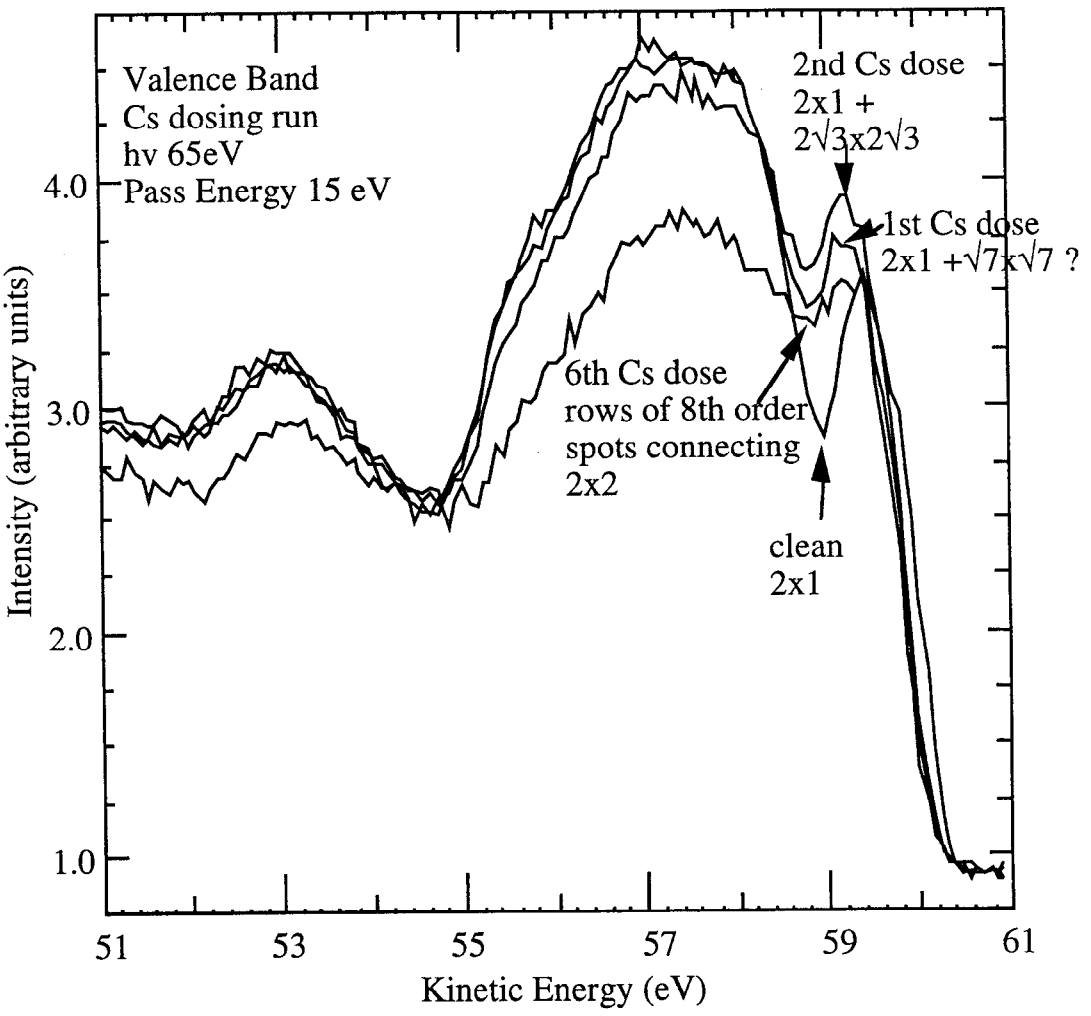

Figure 4.20(b). Valence band region photoemission spectra, Cs/Si(111) room-temperature dosing progression (a) overlay (b) stack. Photon energy 65 eV.

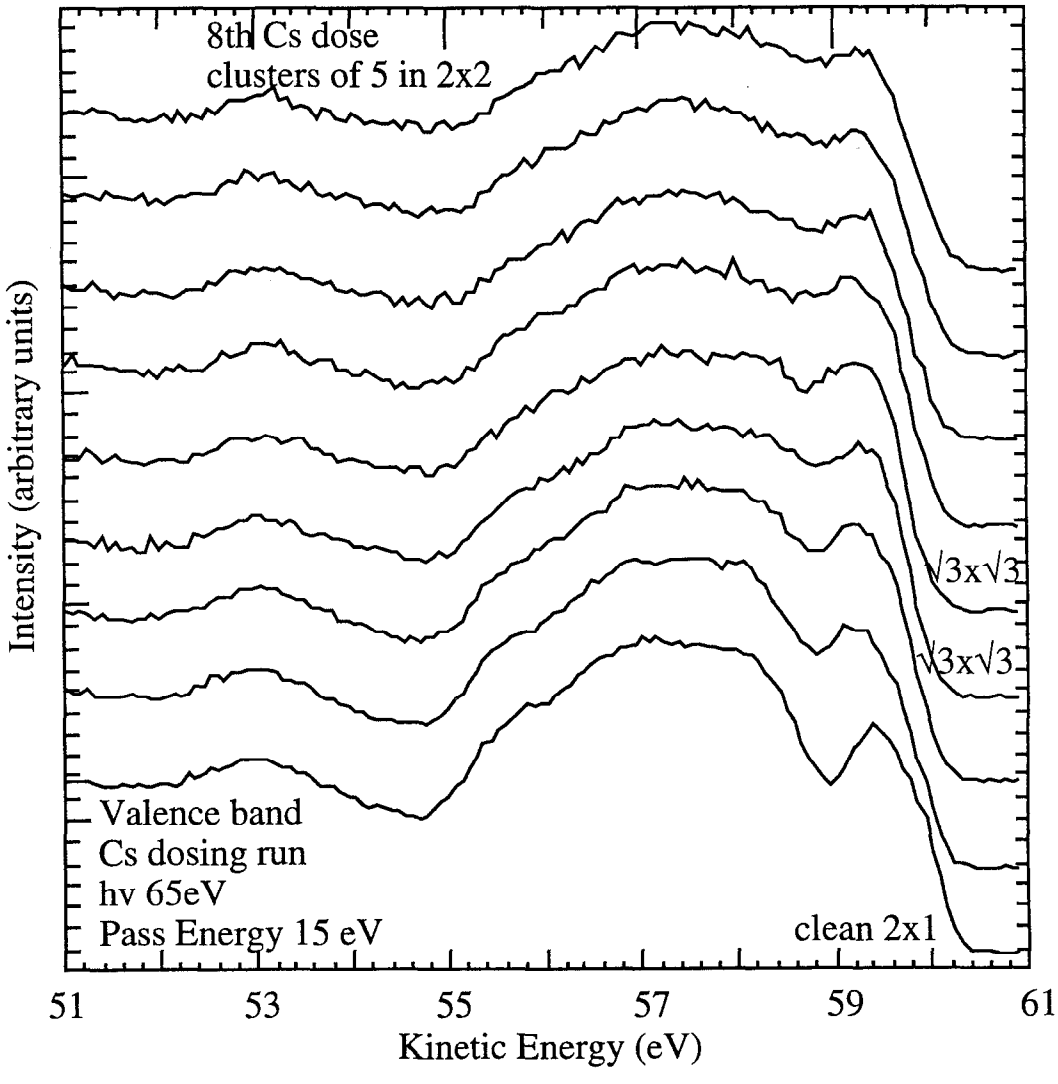

Figure 4.21(a). Valence band region photoemission spectra, Cs/Si(111) room-temperature dosing progression (a) overlay (b) stack. Photon energy 20.8 eV.

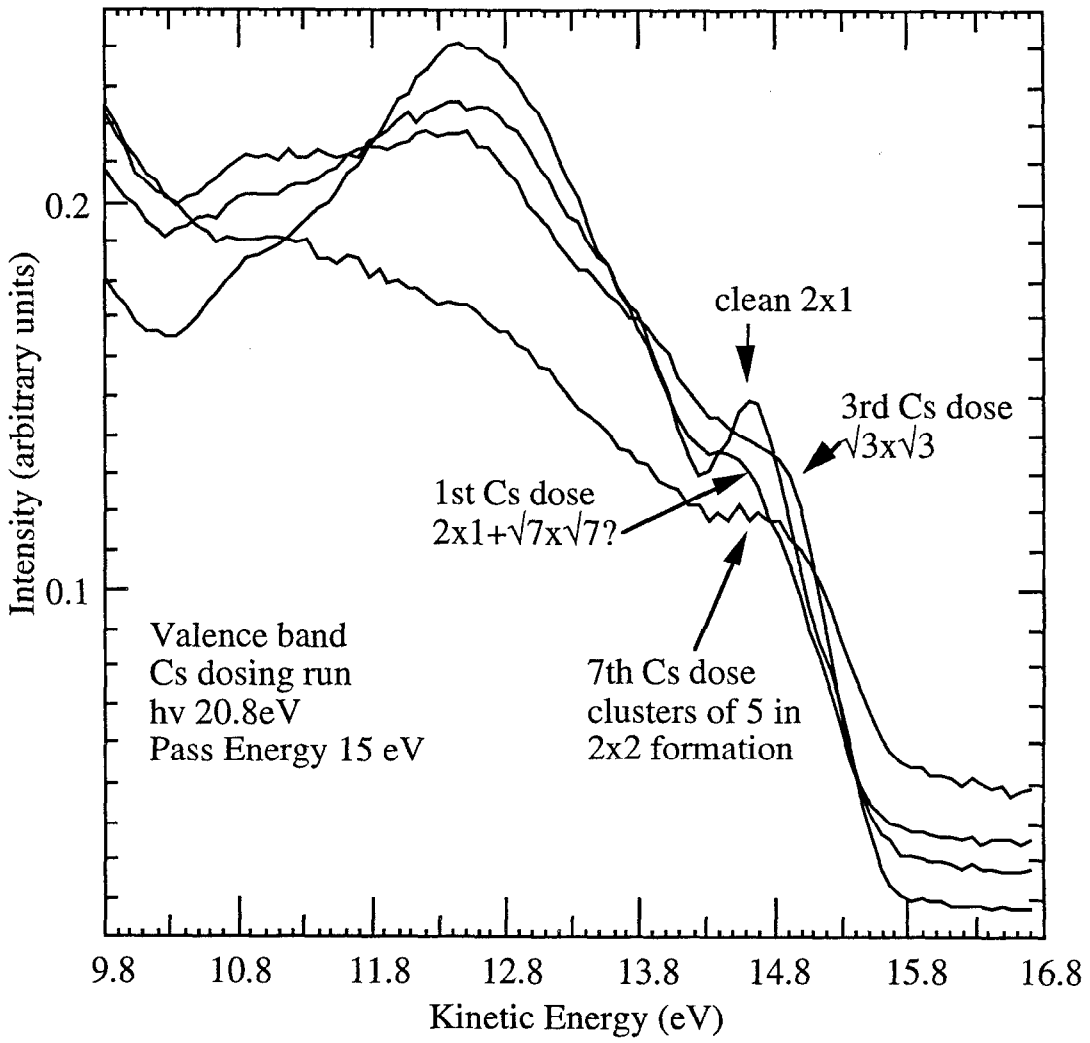

Figure 4.21(b). Valence band region photoemission spectra, Cs/Si(111) room-temperature dosing progression (a) overlay (b) stack. Photon energy 20.8 eV.

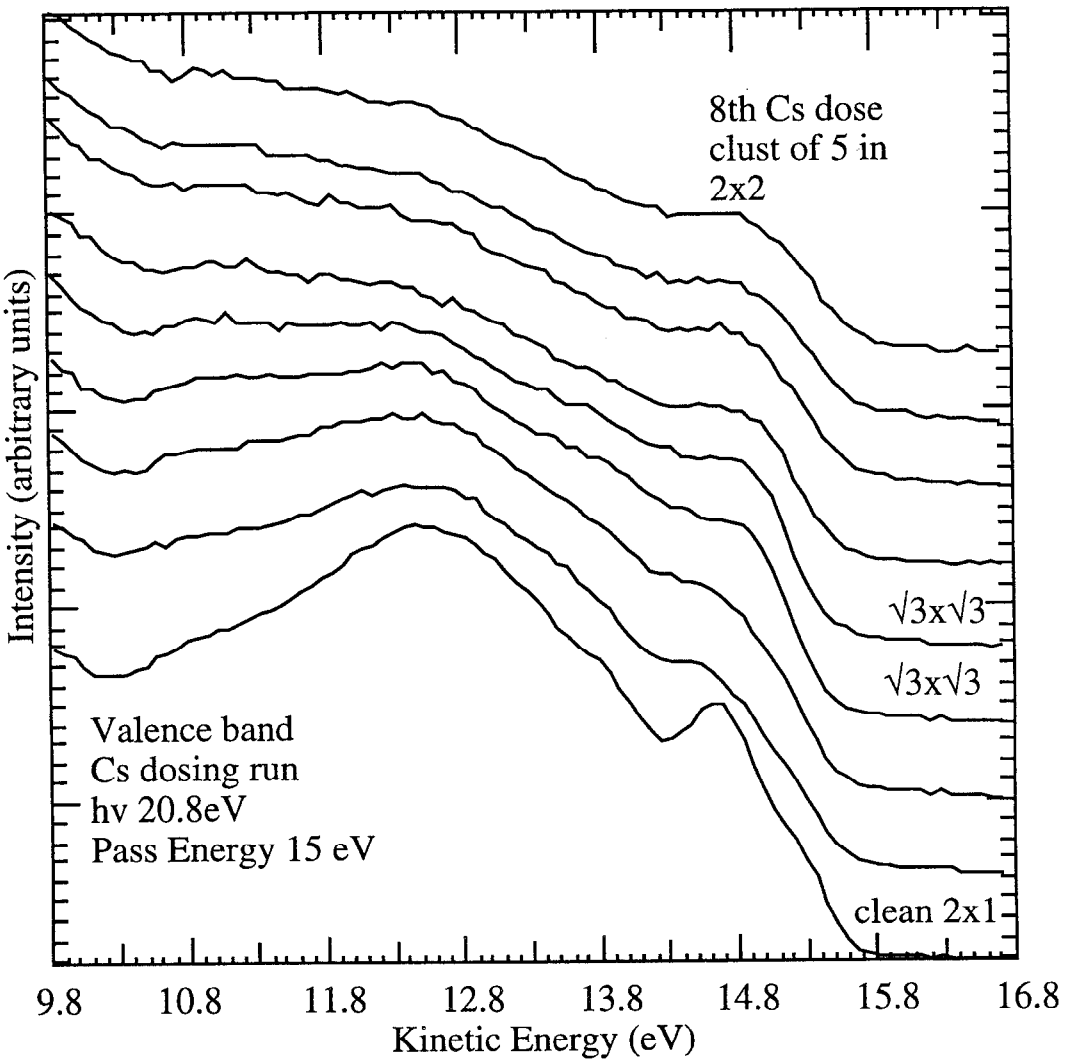

Figure 4.22. Work function difference (relative to the clean Si(111)2x1 surface) for the Na/Si(111) interface as a function of Cs coverage, as determined by fraction of Na 2p peak area saturation. Approximate ranges of observed LEED patterns are indicated.

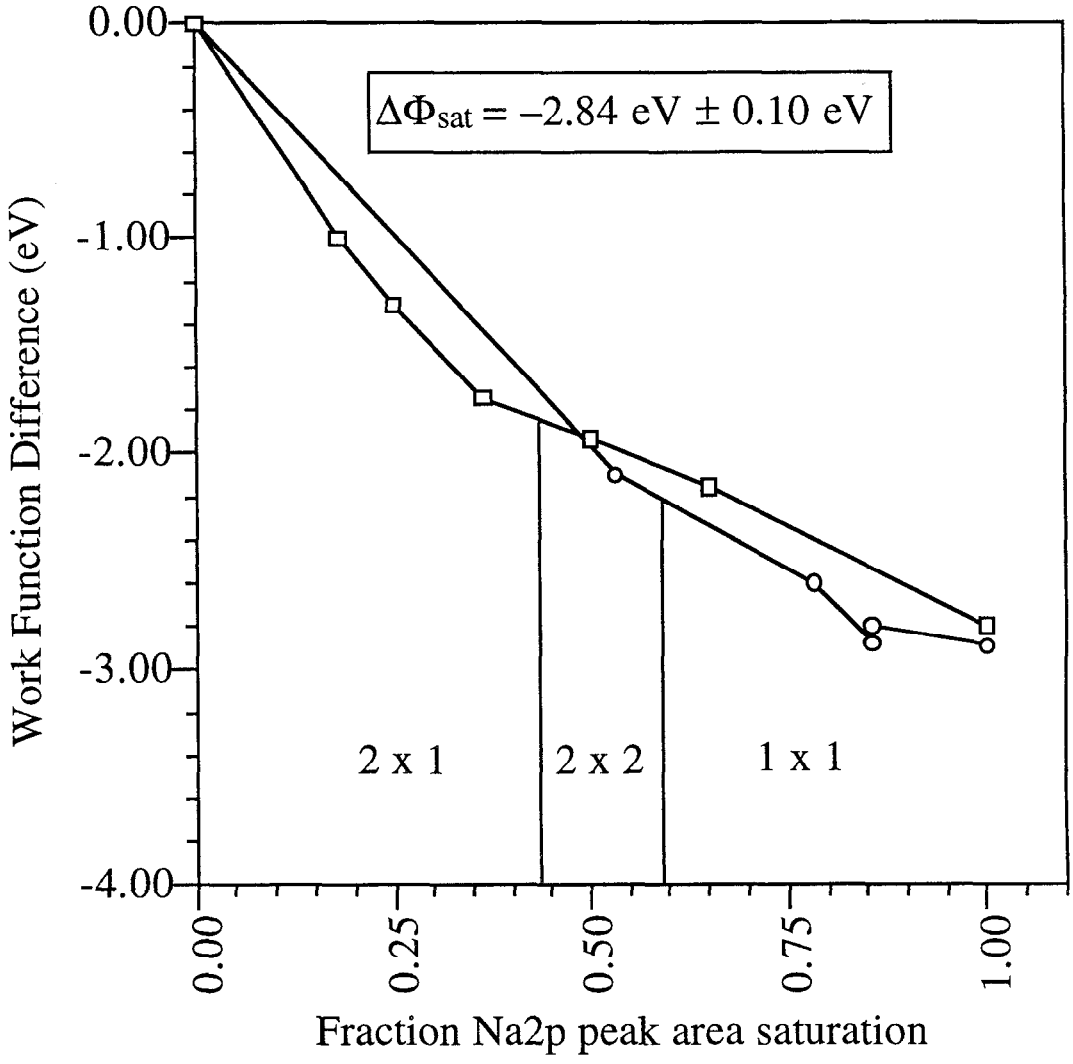

Figure 4.23. LEED photographs, Na/Si(111) room-temperature dosing progression. (a) 2x1 (b) 2x2 (c) 1x1 (pattern at saturation Na coverage).

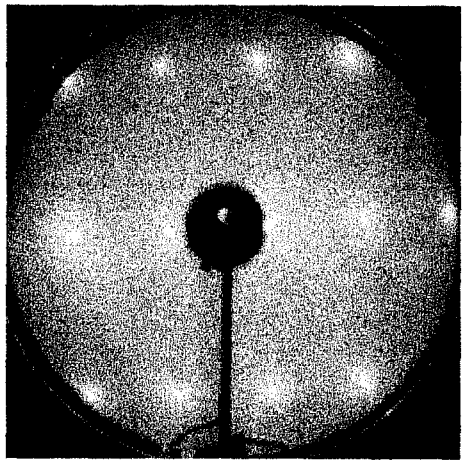

(a) 2 x 1
0% to 43% of Na 2p
area saturation
Beam energy 46.3 eV

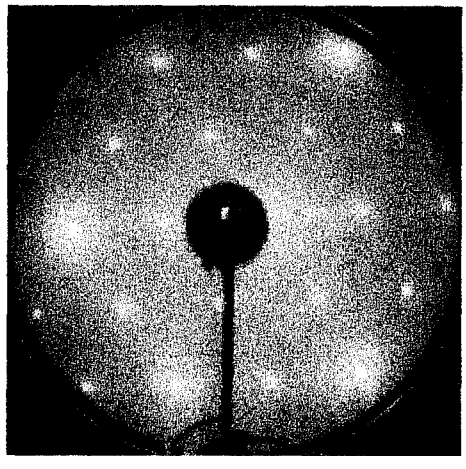

(b) 2 x 2
43% to 59% of Na 2p
area saturation
Beam energy 45.0 eV

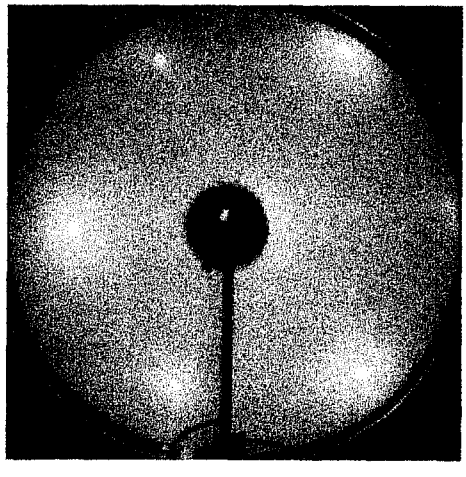

(c) 1 x 1
59% to 100% of Na 2p
area saturation
Beam energy 45.0 eV

Figure 4.24(a). Na 2p photoemission spectra, Na/Si(111) room-temperature dosing progression (a) full spectra. Photon energy 77 eV.

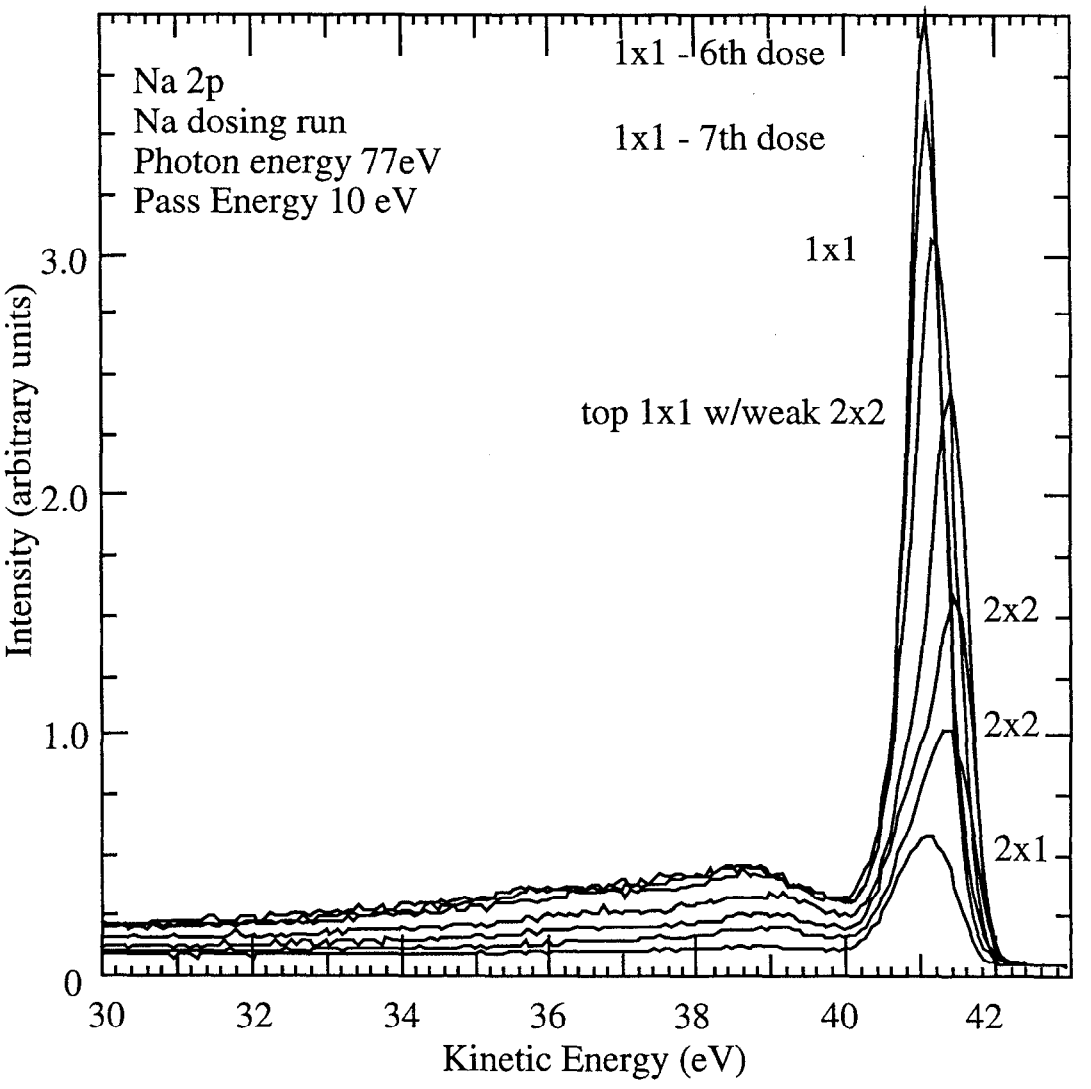

Figure 4.24(b). Na 2p photoemission spectra, Na/Si(111) room-temperature dosing progression (b) peak. Photon energy 77 eV.

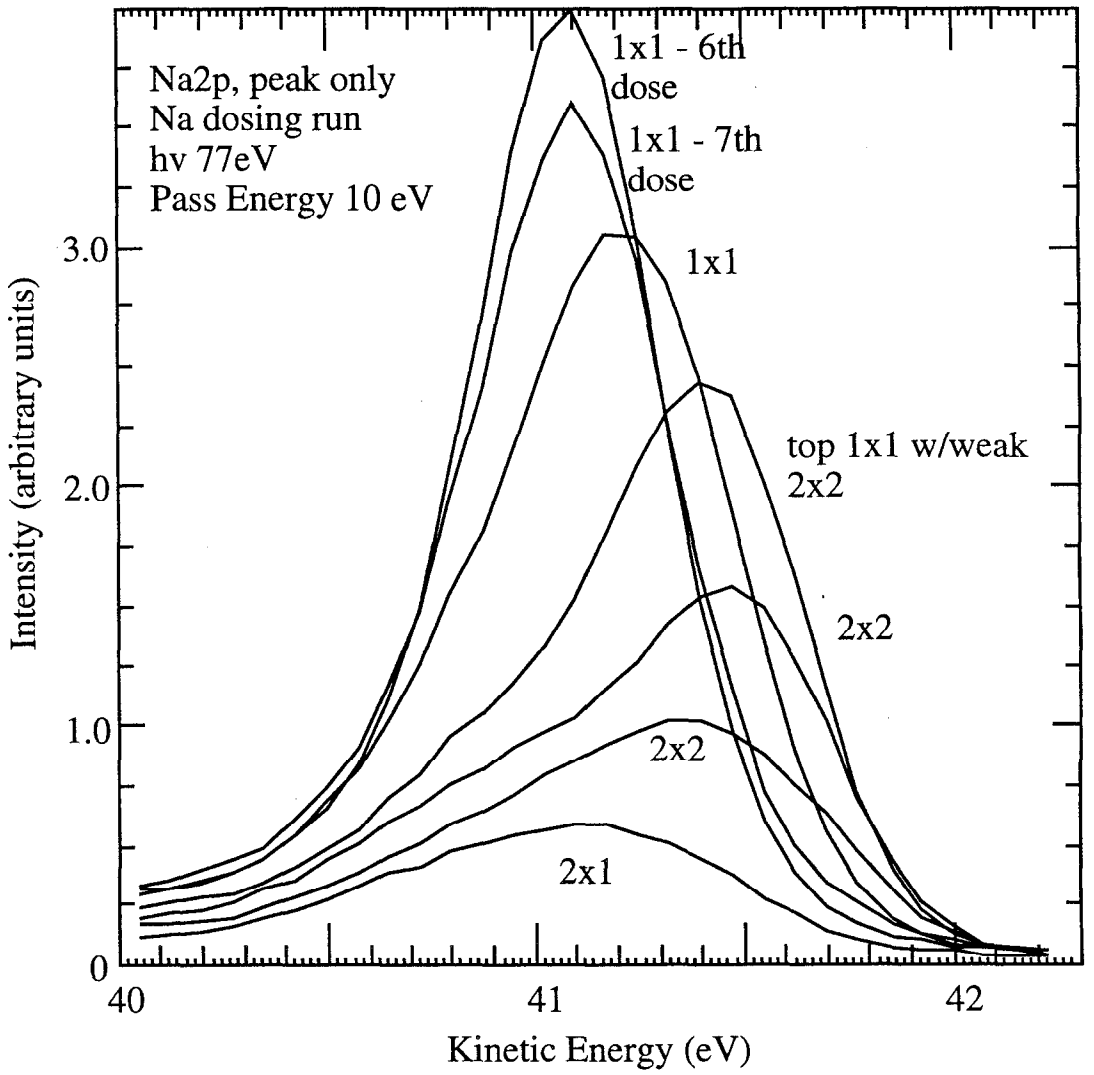

Figure 4.24(c). Na 2p photoemission spectra, Na/Si(111) room-temperature dosing progression (c) plasmon loss region. Photon energy 77 eV.

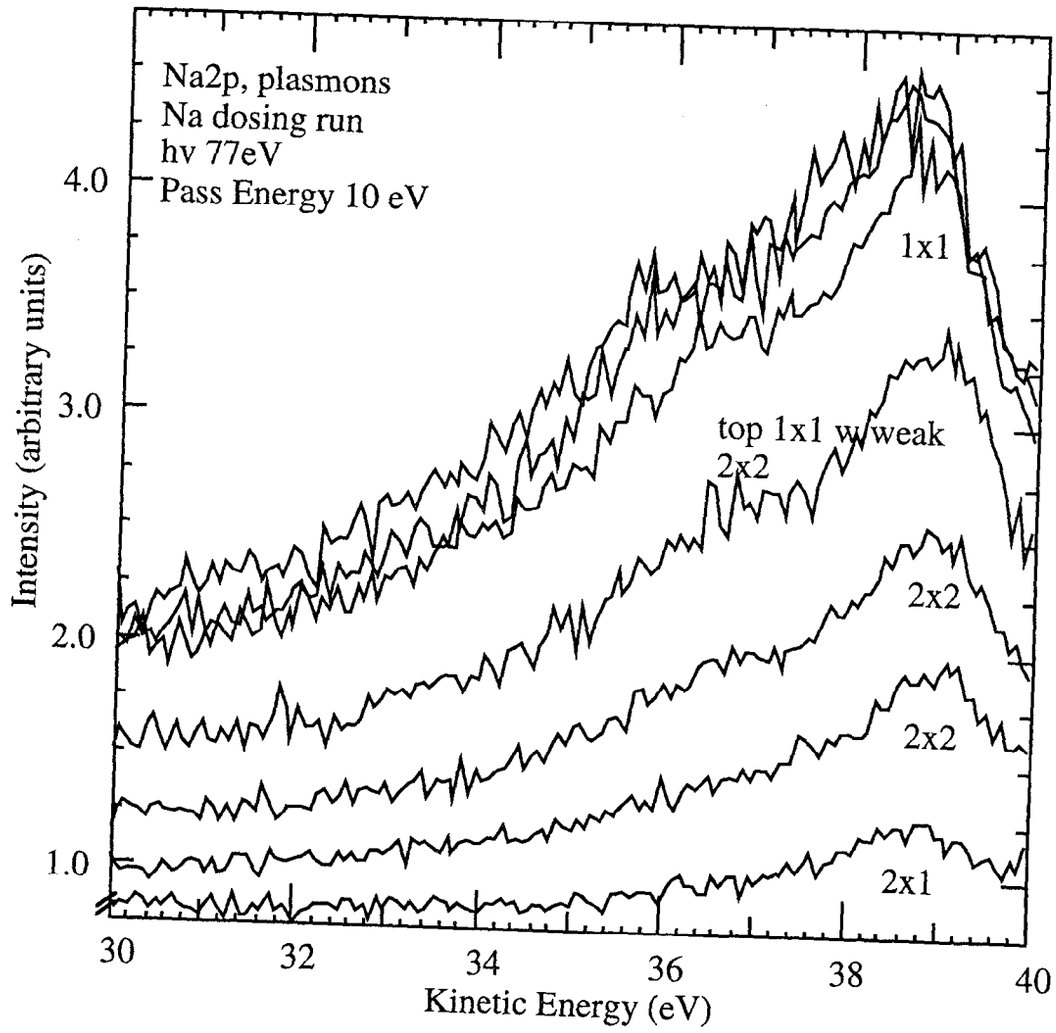

Figure 4.25(a). Surface-sensitive Si 2p photoemission spectra, Na/Si(111) room-temperature dosing progression (a) dosing run. Photon energy 145 eV.

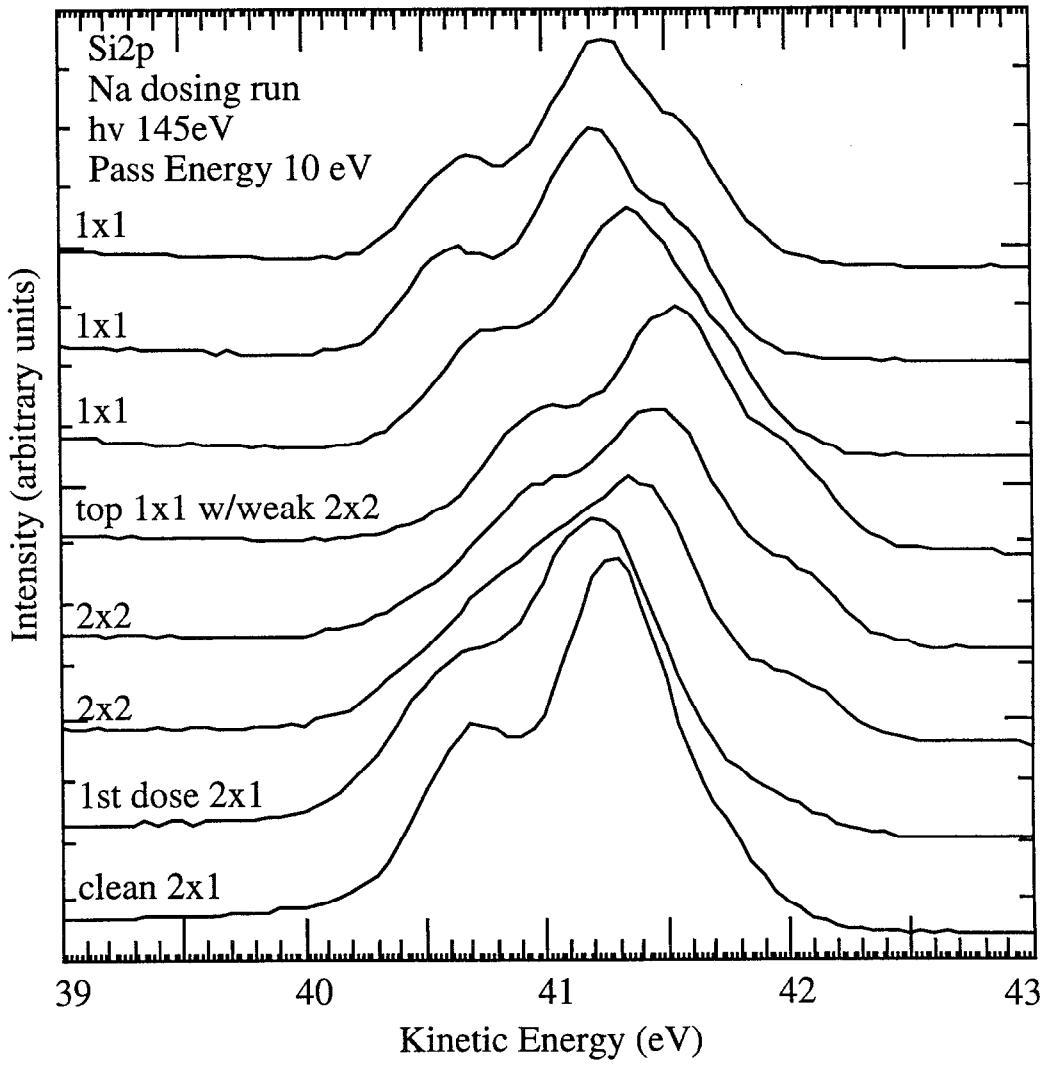

Figure 4.25(b)-(e). Surface-sensitive Si 2p photoemission spectra, Na/Si(111) room-temperature dosing progression (a) dosing run (b)-(e) lineshape fits for clean 2x1 and Na coverages corresponding to the three Na/Si(111) LEED patterns. Photon energy 145 eV.

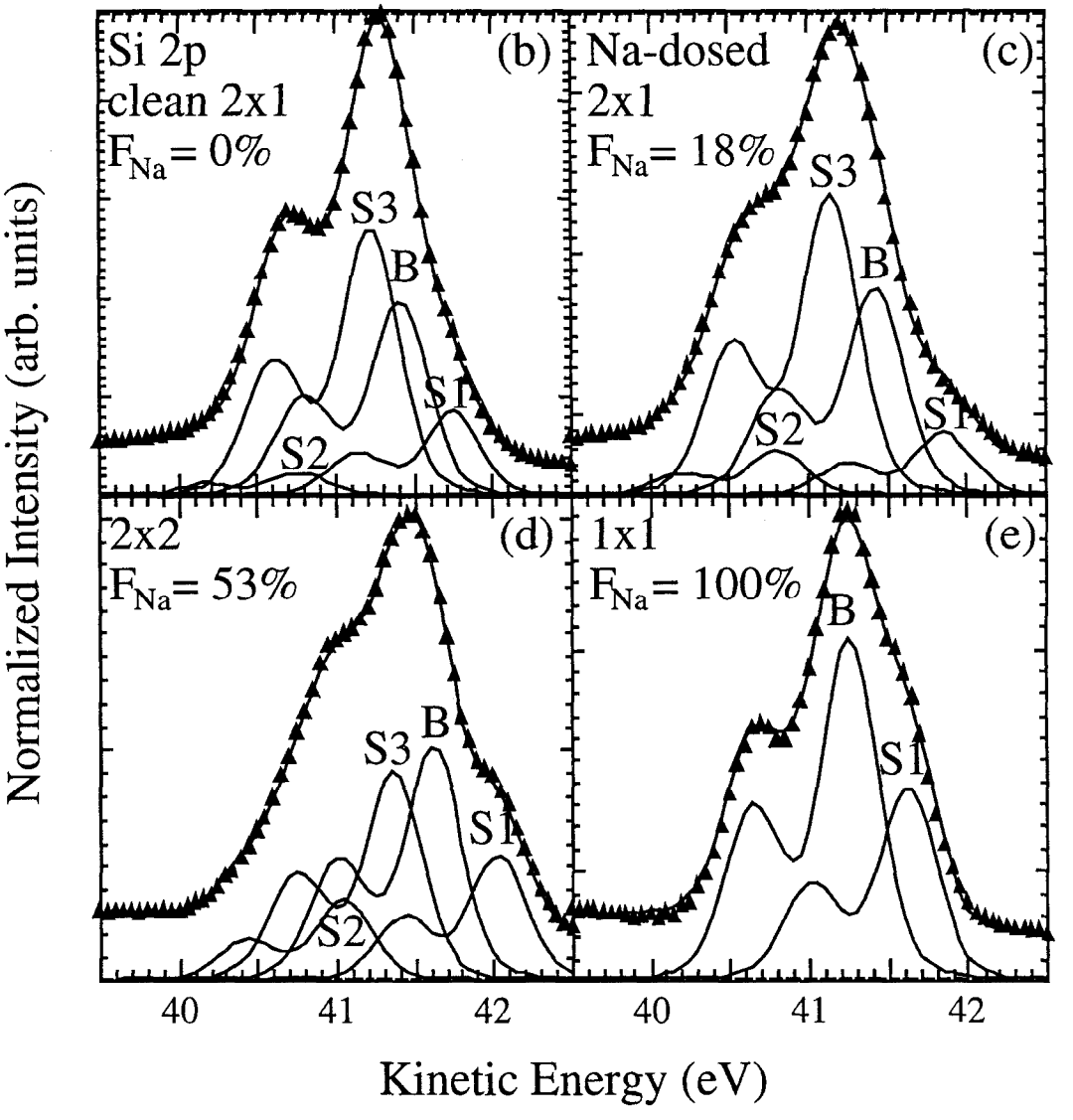

Figure 4.26. Valence band region photoemission spectra, Na/Si(111) room-temperature dosing progression. Note the growth of a large Na-Si bonding peak near the top of the valence band. Photon energy 65 eV.

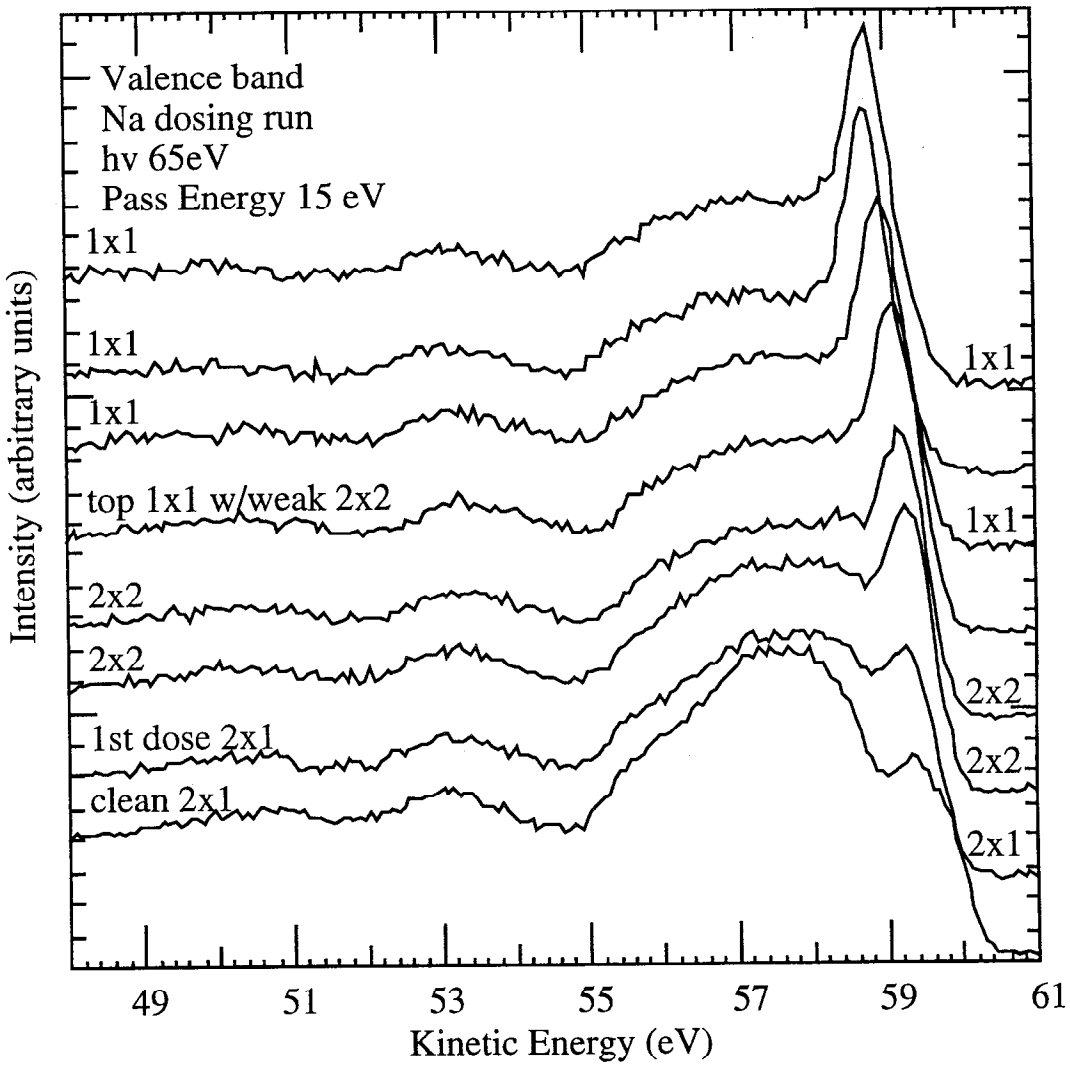

Figure 4.27. Valence band region photoemission spectra, Na/Si(111) room-temperature dosing progression. Note the growth of a large Na-Si bonding peak near the top of the valence band. Photon energy 20.8 eV.

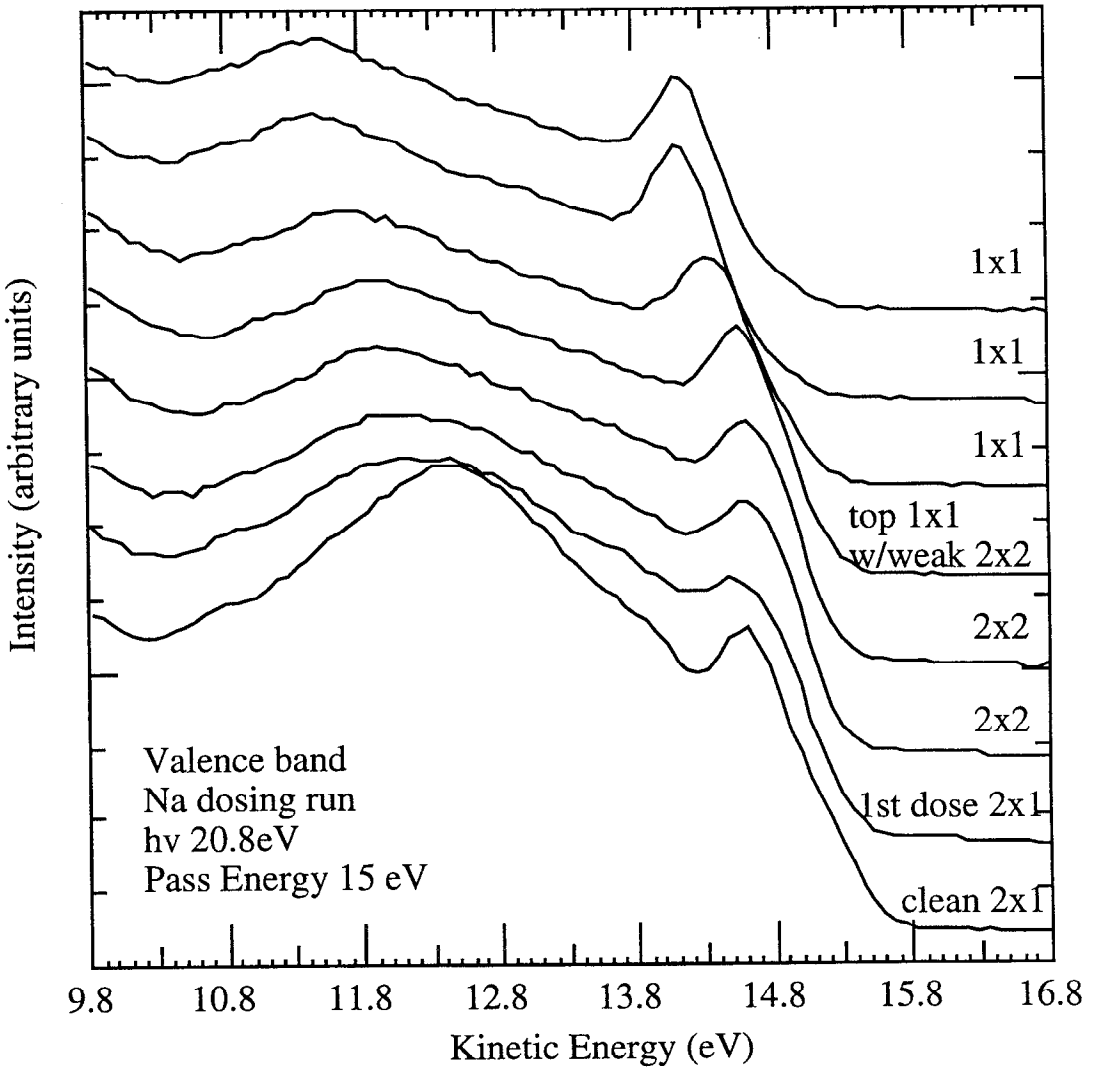

Figure 4.28. Na 2p photoemission spectra, annealed Na/Si(111)3x1 vs. low coverage room-temperature dosed samples. Photon energy 77 eV.

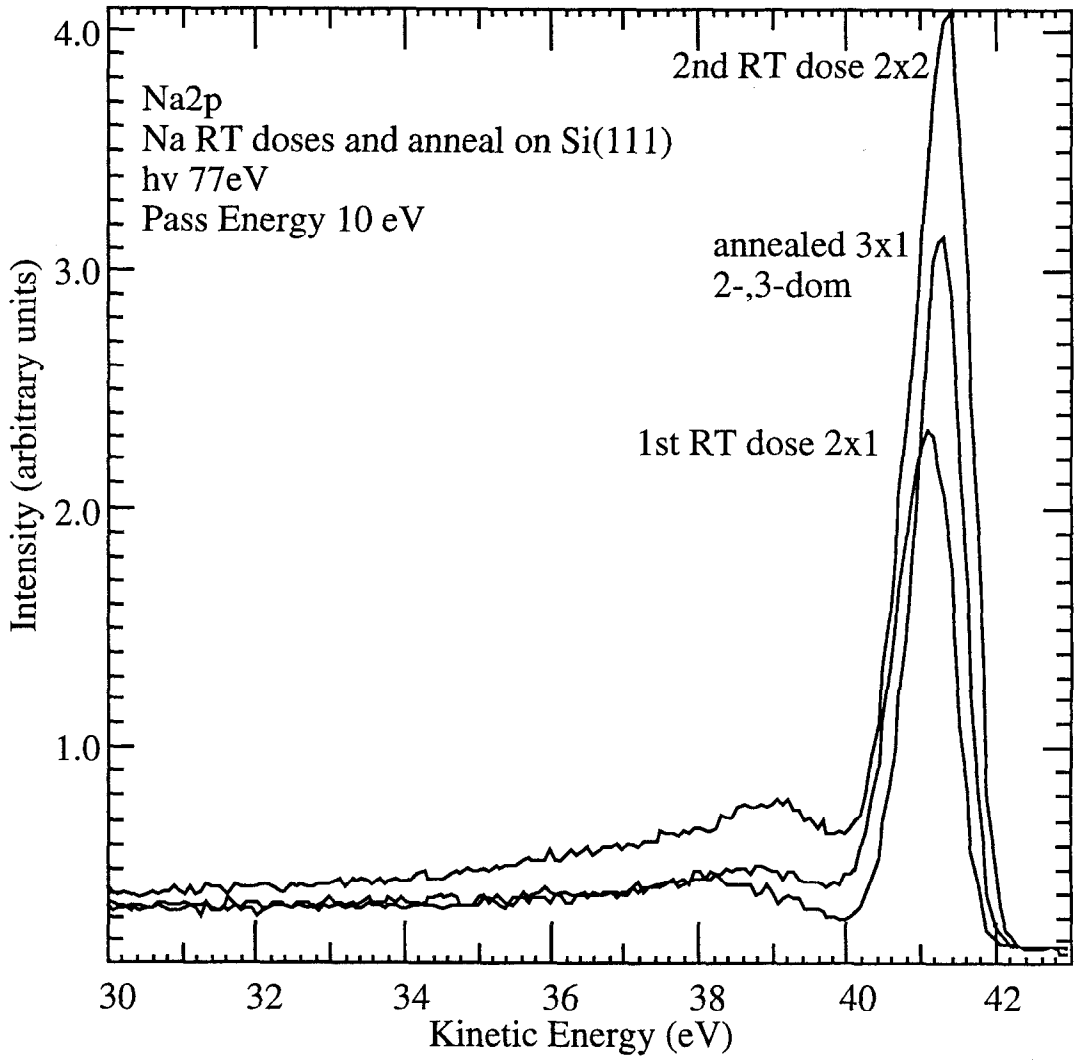

Figure 4.29. Surface-sensitive Si 2p photoemission spectra, annealed Na/Si(111)3x1 vs. low coverage room-temperature dosed samples. Photon energy 145 eV.

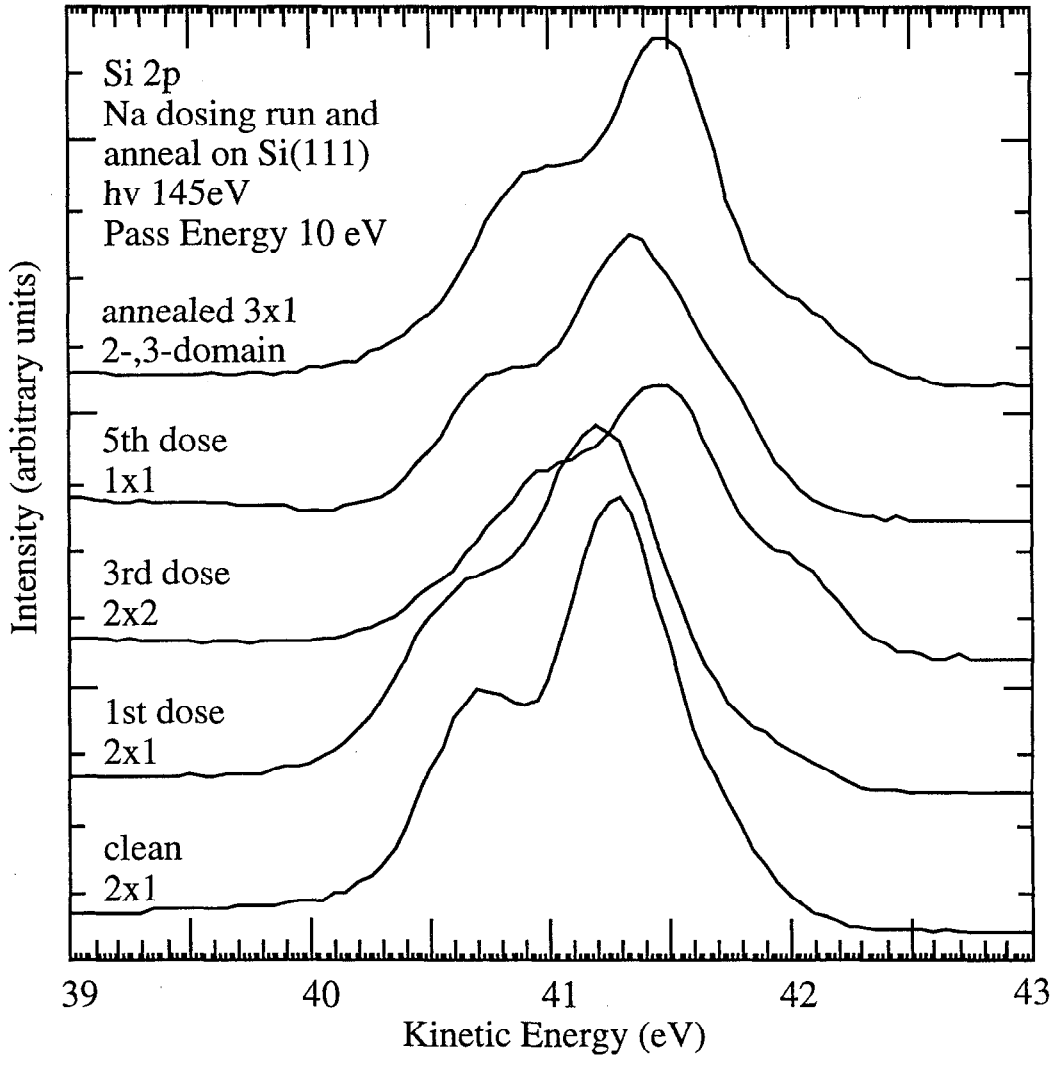

Figure 4.30(a). Valence band region photoemission spectra, annealed Na/Si(111)3x1 vs. low coverage room-temperature dosed samples. Photon energy (a) 65 eV

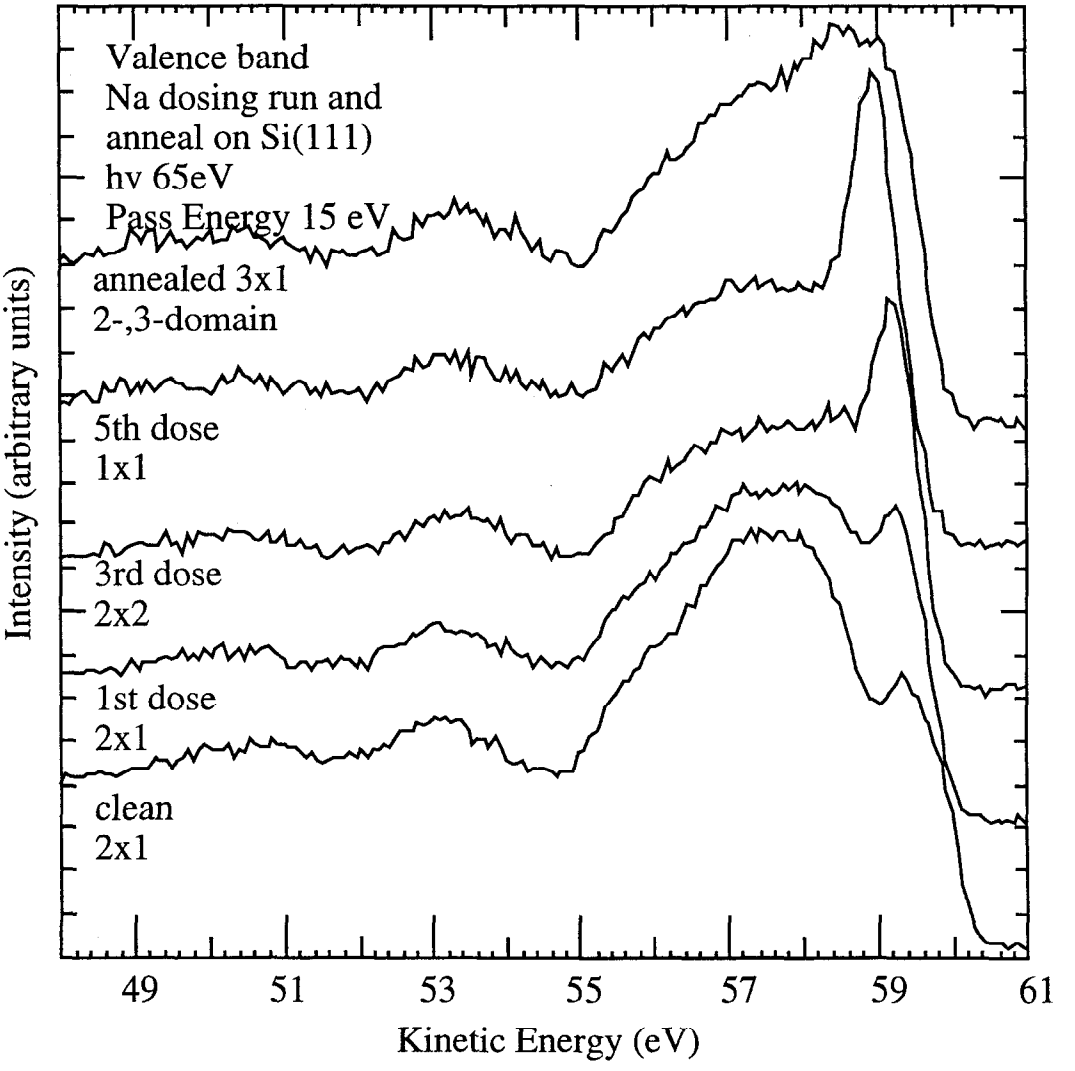

Figure 4.30(b). Valence band region photoemission spectra, annealed Na/Si(111)3x1 vs. low coverage samples. Photon energy (b) 20.8 eV